EFFECTS OF COUPLING AND HETEROGENEITY IN THE PRE-BÖTZINGER COMPLEX CELLS USING FIRST RETURN MAPS

by

Evandro Manica

Master in Applied Mathematics, Federal University of Rio Grande do Sul, 2000

Submitted to the Graduate Faculty of
the Faculty of Arts and Sciences in partial fulfillment
of the requirements for the degree of

Doctor of Philosophy

University of Pittsburgh

2008

UNIVERSITY OF PITTSBURGH

MATHEMATICS DEPARTMENT

This dissertation was presented

by

Evandro Manica

It was defended on

December 2nd 2008

and approved by

Jonathan Rubin, Professor, University of Pittsburgh

Bard Ermentrout, Professor, University of Pittsburgh

William Troy, Professor, University of Pittsburgh

Georgi Medvedev, Associate Professor, Drexel University

Dissertation Director: Jonathan Rubin, Professor, University of Pittsburgh

EFFECTS OF COUPLING AND HETEROGENEITY IN THE PRE-BÖTZINGER COMPLEX CELLS USING FIRST RETURN MAPS

Evandro Manica, PhD

University of Pittsburgh, 2008

The preBötzinger complex located at the ventrolateral medulla in the brainstem is believed to have an important role in generating the respiratory rhythm in mammals, specially the inspiratory process [56]. Keeping this in mind, we will study a small network of such cells by means of a minimal model suggested and experimentally tested by Butera *et al* [6, 7]. A thorough analysis of the Butera model was done for two very small networks of pre-Bötzinger cells: a self coupled single cell and a network of two coupled cells [5]. In order to understand the role of coupling and heterogeneity in these two particular networks we reduce the self coupled single cell network to a one dimensional map using a similar approach as in [37]. Using this one dimensional map, some analytical conditions for switching from one regime to another are determined and numerical results are shown. Using the same idea as for the self coupled single cell case, two identical coupled cells are reduced to a two dimensional iterated map which is a composition of many one dimensional maps. Using the form of these maps, mechanisms for the transition between previously observed regimes [5] are determined and linear analysis is performed for a particular set of parameters.

Introducing heterogeneity on the network of two coupled identical cells, for a fixed level of synaptic input, shows that depending on the level of the synaptic input some different behaviors arise which were not previously observed in a network of homogenous cells [5]. These results suggest that introducing heterogeneity can increase the range in the parameter space for which cells are bursting. This is desirable, since from experiments it is observed that bursting is associated with the inspiratory rhythm of respiration.

TABLE OF CONTENTS

LIST OF TABLES

LIST OF FIGURES

PREFACE

After more than 6 years as a graduate student at the Mathematics Department at the University of Pittsburgh, I made a lot of friends among graduate students, professors and staff.

First of all, I would like to thank my advisor, Professor Jonathan Rubin, for all his patience and and time spent in long discussions on the subject of the thesis.

Thanks to my committee members, Professors Bard Ermentrout, William Troy and Georgi Medvedev for their useful remarks on the thesis.

Special thanks to Professor William Layton whose conversations and positive attitude throughout my years of graduate school help me to keep on track for graduation.

Thanks to my fellow graduate students at the Mathematics Department for the fun time I had here. Thanks to all my friends who I will not name not to be unfair with any of them. Thanks for my soccer partners for the fun and relaxing time outside the Math Department. For all the faculty to whom I had contact with and who provided me with the best of their knowledge.

To all staff who provided a nice environment to study and helped me into various instances of my staying in Pittsburgh.

Last, but certainly not least, to my wife Carolina and to my daughter Sofia whose love was essential to keep me on track all these years in order to obtain my degree even when, at times, we had to be apart. I dedicate this work to you.

1.0 INTRODUCTION

Breathing is a deceptively simple yet remarkable behavior in vertebrates [17]. It is one of the most vital processes of our bodies, occurring continuously and automatically from the time we are born until the day we die. Any disruption in our breathing process can cause irreversible damage to our brain and put our life at risk [58].

Motivated by earlier evidence suggesting that, somewhere in the brainstem, there was a site responsible for generating the rhythm of our breathing process [16], Smith *et al* [56], performed a series of *in vitro* experiments in slices of the brainstem of rats and found a site in the ventrolateral medulla which is believed to play an important role for controlling the respiratory rhythm in mammals, especially the inspiration process. This site was named the *pre-Bötzinger complex* (preBötC)[56].

Later, experiments *in vivo*, found that another structure, also located in the brainstem, the *parafacial respiratory group/retrotrapezoid nucleus* (pFRG/RTN)[24, 26], could be another site for rhythmogenesis. There is not yet enough evidence to characterize the pFRG/RTN as one single structure or 2 distinct structures and so far, the pFRG/RTN has not been captured in *in vitro* experiments [17, 24].

Studies suggest that the preBötC and the pFRG/RTN work as coupled oscillators to regulate the respiratory process [40, 24, 25], providing our body with the ability to change breathing frequency after a given stimulus while maintaining the robust rhythmicity of the network. However, the preBötC seems to take control of the rhythmicity of our breathing system over the pFRG/RTN group, although some recent evidence suggests that, at birth [24], the absence of the pFRG/RTN causes apnoea (in rats) and does not activate the preBötC causing death [17]. Although the pFRG/RTN may have an important role in the respiration process, from now on our attention will be focused on the preBötC.

The importance of the preBötC is supported by experiments *in vivo* and *in vitro*, in rats, showing that any damage to the preBötC causes disturbances in the inspiratory phase of breathing. Among other things, damages to the preBötC can cause breathing disorders during sleep which can evolve to troubled breathing when awake [36]. Similar disturbances are observed when pharmacologically killing preBötC cells [19, 36]. Although, experiments in rats show such problems, in normal, healthy humans, breathing problems during wakefulness are rare, meaning that in our life span not enough preBötC cells will die in order to cause such a problem [17]. Diseases which attack the neurosystem responsible for breathing, in humans, include: Parkinson's disease, multiple syndrome atrophy and amyotrophic lateral sclerosis. The first two occur due to depletion of the ventromedullary NK1 receptor-immunoreactive neurons [4]. The latter occurs due to loss of calcium-binding proteins and, in later stages of the disease, can kill during sleep [1].

The preBötC participates in dictating the rhythm of our breathing process and it is an example of so called *pacemaker systems*. It has been shown that single neurons may not necessarily have pacemaker-like properties. However, intrinsic properties of each neuron together with coupling give the whole system a group pacemaker-like property [11, 45]. In both cases, bursting pacemaker-like properties of the preBötC complex depending on I_{NaP} (persistent sodium current) have an important role in rhythm generation [56, 29]. There is also some evidence showing that Ca^{+2}-activated inward cationic current I_{CAN} influences pacemaker activity[11]. Other examples of pacemaker systems include hormonal secretion and digestion [20].

Experiments at the network level show that cells within the preBötC may not all be active or silent at the same time. That is, while a group of cells are active another group of cells may not present any activity at all. Within the active state, different groups of cells exhibit different behaviors [6, 7]. Cells engaged in the same pattern of activity are said to be synchronized. Experiments also suggest that the strength of connections between cells (coupling) and intrinsic properties of the cells such as concentration of calcium, sodium or potassium channels present in each cell (heterogeneity) play a role in determining in which state a given cell will be [6, 44, 28, 10, 31]. Given that *breathing* has to be adaptable over changes in the environment and physiological state, it is reasonable to believe that coupling

and heterogeneity are some of the mechanisms responsible for such adaptability. Most of these predictions were confirmed when a slice of brainstem of a neonatal rat was prepared *in vitro* with the preBötC and the inspiratory-related motor activity intact [12].

Understanding mechanisms that underlie inspiratory rhythm generation in the slice will serve as a foundation for unraveling the mechanisms in more intact preparations, including en bloc and in vivo [17].

In recent years, more and more attention has been given to the study of *neural networks*, such as the preBötC, using mathematical models. A common framework in which these neural networks are modeled uses the *Hodgkin-Huxley equations* [22]. These equations model the dynamics of the membrane potential of the cell, together with the inflow and outflow of several substances such as calcium, potassium and sodium that contribute to this potential. Many neural functions, and diseases that disrupt these functions, cannot yet be completely understood either because experimenting is too expensive or because experimental techniques are still too limited. Developing good mathematical models allows us to clearly distinguish the roles of the network components, to efficiently generate predictions to guide subsequent experimental studies, and to understand general mechanisms of neural network dynamics. Experiments *in vivo* have been done in connection with mathematical models suggesting that, considering the right models, we can accurately imitate and generate relevant predictions about what happens in these neural networks [23].

As observed in experiments *in vitro*, during inhalation, cells in the preBötC are in their *active phase* and during exhalation, cells go *silent*. These alternating phases of activity and silence form a rhythm called *bursting*. During each active phase, cells experience two or more abrupt changes in the membrane potential (that is, the difference in charge across a cell's membrane) followed by a period of recovery (where we do not see any activity) . Each of these abrupt changes is called a *spike*.

Applying the Hodgkin-Huxley formalism, Rybak *et al* [52] model respiratory neurons in the brainstem looking for mechanisms to explain oscillations and firing patterns. Based on data from *in vivo* experiments, they develop two models for single neurons. Model 1 shows an adapting firing pattern in response to synaptic excitation. Model 2 shows a ramp firing due to depolarization after a period of synaptic inhibition. The differences between the two

models arise due to the different types of calcium channels that each one has. In a second paper, Rybak *et al* [53] develop two- and three-phase models of the central respiratory pattern generator (CRPG) using experimental data. The former models the inspiratory phase of respiration and its termination mechanism is via late-I neurons; the latter models the expiratory phase which has a different mechanism for termination.

The inspiration process is connected to synchronized oscillatory bursting behavior of the preBötC cells. Butera *et al* [6, 7] develop a nonlinear differential equation model network of cells exhibiting synchronized bursting activity consistent with that observed experimentally in respiration. For a model network composed of identical cells, they [6, 7] systematically changed some relevant parameters of the model and found that changing these parameters could give rise to a variety of behaviors which include bursting, spiking and quiescence. These different regimes were found for a significantly large range on the parameter space, implying that the system is robust.

They also found that bursting becomes even more robust in simulations of a network of nonidentical (heterogeneous) coupled cells relative to that seen in a single cell. In the model, mechanisms responsible for the adaptability of the respiratory patterns have to preserve these patterns over a broad range of parameters and frequencies, that is, over a large dynamic range. Simulations show that some of the mechanisms that confer such adaptability are *coupling* and *heterogeneity*, complying with experiments *in vitro*. In their model of bursting neurons with excitatory coupling, bursting occurs via fast activation and slow inactivation of the persistent sodium I_{NaP}. In a later work by Rubin and Terman [49], a small preBötC network of heterogeneous cells was analyzed. In this context, conditions for synchrony and break down of synchrony of the network were found.

Using Butera's model as a baseline, Rybak *et al* [54] determined that transitions between different regimes may occur through changes in extracellular concentration potassium or an elevation of the conductance of the persistent sodium current and discussed the role of these currents in triggering or abolishing bursting activity in the preBötC in a model and by means of experiments *in vivo* [55].

Best *et al* [5] explores a network of a single self-coupled cell and a model network with two coupled identical cells from the preBötC, based on the Butera model. In their work,

they found regions for some key parameters, namely g_{syn} and g_{ton}, where the cells are either silent, bursting or continuously spiking (tonically active). These two parameters represent, respectively, the maximal strength of excitatory synaptic connections from one neuron to the other and the conductance of external excitatory synaptic current into the network from elsewhere in the brainstem. In an experiment, these quantities can be changed and can affect the dynamic behavior of the network. The methods used in [5] include *fast/slow decomposition* and *bifurcation* analysis. *Fast/slow decomposition* analysis takes into account the disparate time scales of the network, treating the slowest variable as a constant and studying the dynamics of the fast subsystem as a function of the parameters. After the analysis is complete, the slow and fast subsystems are recombined to obtain the full dynamics of the network. *Bifurcation* analysis is performed by finding values of a key parameter at which the fast subsystem has an abrupt change in behavior. Each value of the parameter in which the system has these abrupt changes is called bifurcation point. At the bifurcation point possible changes in the dynamics of the system include: from stable fixed point to periodic solutions; from no fixed point to two fixed points (one stable and another unstable) and so on [43].

In order to model preBötC cells, a set of nonlinear differential equations was used. Analysis of such systems of equations is often complicated and relies on sophisticated tools [43]. In order to simplify such analysis some methods were developed to reduce the number of equations to be solved, yet maintaining important characteristics of the whole system. One such method relies on maps. Roughly speaking, maps are obtained by fixing a local transverse section to a continuous oscillatory system, letting the system evolve in time and recording each passage through the local section. These points form a map which can be related to the dynamics of the full system and help to describe important characteristics of the full system [27, 59]. This idea of reduction of systems differential equations to maps has been applied to models in neuroscience [15, 37, 8, 50, 51] as well as in many other areas [18, 2, 13, 41, 48].

In many models used in neuroscience and other areas as well, high dimensional systems of differential equations are often reduced to the study of one dimensional maps. In this context, we can cite the reduction of a three-dimensional model for the Belousov-Zhabotinskii reaction in a continuous flow stirred tank reactor (CSTR) [47] to a piecewise linear, discontinuous one

dimensional map. Analysis of the map shows that the full (excitable) system, as observed before [47], can present a variety of behaviors such as stable fixed point, bistable bursting solutions and irregular behaviors [48].

Other examples include, a pharmacologically isolated leech oscillatory heart interneuron which was reduced to a map and then, temporal characteristics of spiking and bursting patterns as well as transitions between them were studied [8]. In a network of two neurons coupled by inhibition [33], a five dimensional system of voltage-gated equations is reduced to a one-dimensional map through slow/fast decomposition analysis and slow manifold information.

In all of these models, the reduction to a one dimensional map helped to unravel some characteristics of the full model which would be otherwise harder to explain or find. Sometimes the dynamics of the full system cannot be fully understood through a one dimensional map setting yet it may not be possible to reduce the system of equations to a higher dimensional map. Higher dimensional maps have been constructed phenomenologically to reproduce some novel characteristics of a given problem [57]. Once the parameters of the system are calibrated, the study of this higher dimensional map is often more easy than the study of the full network. In particular we can cite a two dimensional map with one slow and one fast variable which reproduces different regimes of a single uncoupled neuron including bursting, spiking and synchronized states [50]. A variation of the model in [50] tries to replicate the behavior a complex neurobiological system for which a Hodgkin and Huxley formalism has been used to represent the full dynamics of the system. So far, to the best of our knowledge, there has been no reduction of a network of coupled preBötC neurons to a two or higher dimensional map.

Certain details about transitions between activity patterns are not analytically tractable in a network setting. As a first step to better understanding the role of heterogeneity in expanding the dynamic range of inspiration we will use a reduction based on maps. Medvedev [37] used fast/slow decomposition and bifurcation analysis to develop a one dimensional map expressed in terms of the slow dynamics and averaging over the fast subsystem to study the dynamics of a physiological model of a pancreatic β-cell [9]. Using the method defined in [37], which was developed for a class of models which includes all square wave models (e.g.

[38, 39]), we obtained a one dimensional map for a single preBötC cell with self-coupling. Considering the structure of our map some information about the transitions between different states was extracted. Our main result determines some analytical conditions for the transition between spiking and bursting when for small values of the parameter g_{syn} the cell is spiking. Numerical results corroborate our findings.

In chapter 4, a two dimensional map for the 2-cell network with identical cells was obtained. The two dimensional map resembles the one dimensional map in its derivation but, in terms of the analysis, it is more complicated due to the fact that 2 slow variables are used in the derivation of the map and these variables are coupled together. Thus, the dynamics of one affects the other in every point in the range of definition of the maps.

Another difference between the two dimensional map and the one dimensional map is the presence of branch points in the two dimensional case. Branch points refer points from which multiple branches of the map converge. A branch point is not a fixed point of the two dimensional map but rather represents a change in the direction of flow for one of the cells. Due to the presence of branch points an analysis of the conditions for the transition to another branch were also discussed. Taking one value on parameter space (g_{syn}, g_{ton}) for each of the four regions found in [5], several predictions about the structure of the map were made and some numerical results were obtained. In order to determine the stability of the fixed points of the map, a linear analysis of the map was attempted in which the eigenvalues were computed numerically for the case when the cell presents synchronous behavior. Numerical difficulties arose in obtaining the eigenvalues of the system due to the instability of the synchronous solution and due to the fact that the synchronous and asynchronous are really close to each other, meaning that a very small perturbation to synchronous state takes us to the asynchronous state. Discussion about these numerical difficulties is also included.

In Chapter 5, the role of heterogeneity and coupling in the *pre-BötC*, is studied by means of simulations of a minimal two cell network to isolate key mechanisms of the full system. Although, numerically we can see how heterogeneity and coupling change the behavior of the network, the specific mechanisms through which these effects occur remain to be understood. Using fast/slow decomposition and bifurcation analysis, numerical analysis was performed by perturbing slightly the degree of heterogeneity of the sodium current, namely δ, across

the two cells and analyzing the behavior of the network. We determined the behavior of the network for fixed values of g_{syn} and δ, under systematic changes in g_{ton} and gained, besides the improvement in the dynamic range of bursting for increasing δ, an understanding of the effect of δ into the network. In this heterogeneous context, each of the cells may be engaged in a different activity pattern. To the best of our knowledge, this type of behavior has not previously been analyzed in the study of small neural networks in the brainstem.

Lastly, in chapter 6, we summarize all the work done and suggest possible extensions and future directions this work can take.

2.0 MODEL EQUATIONS AND REVIEW OF SOME RESULTS ON SMALL NETWORK OF PREBÖTC

In this chapter, Butera's minimal model [6, 7] of a network of preBötC cells modeling the inspiratory phase of respiration and a review of some of the relevant results previously obtained are presented. Butera's model followed the usual Hodgkin-Huxley formalism using voltage-gated variables to account for the different behaviors experimentally seen. Butera's numerical results are consistent with what has been seen in experiments *in vitro* [6, 7]. It is also noticed in [6] that preBötC cells are purely excitatory, that is, inhibition does not play an important role in the process of inspiration for experiments in reduced preparations [24]. Using Butera's model, Best *et al* [5] analyzed the smallest possible networks of preBötC cells: a single self coupled cell and two identical synaptically coupled cells, which are reviewed here. At last, a slight modification of Butera's model is suggested which is going to be used for the rest of this thesis.

2.1 MODEL EQUATIONS

The set of equations describing the dynamics of a small network of preBötC cells using voltage-gated variables is given by [5, 6, 7]

$$v_i' = \frac{-I_{NaP}(v_i) - I_{Na}(v_i, n_i) - I_K(v_i, n_i) - I_L(v_i) - I_{ton}(v_i) - I_{syn}(v_i)}{C} \quad (2.1.1)$$

$$h_i' = \epsilon \frac{h_\infty(v_i) - h_i}{\tau_h(v_i)} \quad (2.1.2)$$

$$n_i' = \frac{n_\infty(v_i) - n}{\tau_n(v_i)} \quad (2.1.3)$$

$$s_i' = \alpha_s(1 - s_i)s_\infty(v_j) - \frac{s_i}{\tau_s}, \quad (2.1.4)$$

where C is the capacitance of the cell ; v_i represents the membrane potential of the cell; h_i and n_i are inactivation and activation variables, respectively; s_i is the synaptic coupling; τ_s is a positive time constant and ϵ is a small and positive constant. The right-hand side of (2.1.1) is the sum of all inward and outward currents and their expressions are given below:

$$\begin{aligned} I_{NaP}(v_i) &= \bar{g}_{NaP} m_{P,\infty}(v_i) h(v_i - E_{Na}), \quad I_{Na}(v_i) = \bar{g}_{Na} m_\infty(v_i)^3 (1 - n_i)(v_i - E_{Na}), \\ I_K(v_i) &= \bar{g}_K n_i^4 (v_i - E_K); \quad I_L(v_i) = \bar{g}_L(v_i - E_L), \\ I_{ton}(v_i) &= \bar{g}_{ton}(v_i - E_{syn}), \quad I_{syn}(v_i) = \bar{g}_{syn} s_i (v_i - E_{syn}). \end{aligned}$$

Above, E_{Na}, E_K, E_L and E_{syn} are resting potentials for the sodium, potassium, leakage and synaptic currents, respectively; $\bar{g}_{NaP}$, $\bar{g}_{Na}$, $\bar{g}_K$, $\bar{g}_L$, $\bar{g}_{ton}$ and $\bar{g}_{syn}$ are the maximal conductances for the persistent sodium, sodium, potassium, leakage, tonic and synaptic currents, respectively. Their values with respective units are given in table 1. Finally,

$$\begin{aligned} m_{P,\infty}(v_i) &= \frac{1}{1 + e^{\frac{v_i + 40}{-6}}}, \; n_\infty(v_i) = \frac{1}{1 + e^{\frac{v_i + 29}{-4}}}, \quad m_\infty(v_i) = \frac{1}{1 + e^{\frac{v_i + 34}{-5}}}, \quad h_\infty(v_i) = \frac{1}{1 + e^{\frac{v_i + 48}{6}}}, \\ s_\infty(v_i) &= \frac{1}{1 + e^{\frac{v_i + 10}{-5}}}, \quad \tau_h(v_i) = \frac{\bar{\tau}_h}{cosh\left(\frac{v_i + 48}{12}\right)}, \; \tau_n(v_i) = \frac{10}{cosh\left(\frac{v_i + 29}{-8}\right)}, \end{aligned}$$

for $i = 1, 2$, where $y_\infty(v_i)$ with $y \in \{m, n, h, s\}$ are steady-state voltage-dependent functions and $\tau_h(v_i)$ and $\tau_h(v_i)$ are voltage-dependent time constants. Also $\frac{\bar{\tau}_h}{\epsilon} = 10000 msec$. For more details about the connection with biological experiments, see for example [6].

In the single cell case, $i = j = 1$ and, for simplicity, the subscripts and bars in the above equations will be omitted. For the 2-cell coupled case, $i = 1, 2$ and $j = 3 - i$. The model described by the set of ordinary differential equations (2.1.1)-(2.1.4) was proposed by [6] as

$\bar{g}_{NaP}$	$\bar{g}_{Na}$	E_{Na}	$\bar{g}_K$	E_K	$\bar{g}_L$	E_L	$\bar{g}_{ton}$	E_{syn}	$\bar{g}_{syn}$
2.8 nS	28 nS	50 mV	11.2 nS	-85 mV	2.8 nS	-65 mV	[0;1] nS	0 mV	[0;15] nS

Table 1: Values of some parameters as given in [5] with respective units

the minimal model, built out of existing currents, that reproduces a variety of experimental results. For a given set of the parameters, this model gives silence, bursting and spiking as $\bar{g}_{ton}$ is varied. In this model, bursting can be started and terminated through fast activation and slow inactivation of the I_{NaP} current. Another way to initiate and terminate bursting is through fast activation of the I_{NaP} current and slow activation of the potassium current, I_K [5, 6].

2.2 SOME PREVIOUS RESULTS ON SMALL NETWORKS OF PREBÖTC CELLS

Looking into equations (2.1.1)-(2.1.4), for the single self coupled case, as a system of ordinary differential equations evolving with time, one can decompose the system based on its different time scales. This idea of breaking down in different time scales is also called the fast/slow decomposition analysis [27, 5]. In this set of equations, note that the coefficient of (2.1.2), $\frac{\epsilon}{\tau_h}$, for ϵ sufficiently small is much smaller that $\frac{1}{C}$ and $\frac{1}{\tau_n}$. Thus, the dynamics of equation (2.1.2) will be much slower than the dynamics of the remaining equations. Therefore, we shall refer to equation (2.1.2) as the slow subsystem and refer to equations (2.1.1), (2.1.3) and (2.1.4) as the fast subsystem.

Using the fact that h moves much slower than any other variables, h can be used as a control parameter and a bifurcation analysis [32, 59] on the fast subsystem can be performed in order to infer some properties of the full system [46].

In figure 1, the bifurcation diagram and the h-nullcline ($\dot{h} = 0$) are shown for some fixed parameters of the fast subsystem for the single self coupled case. The intersection of the

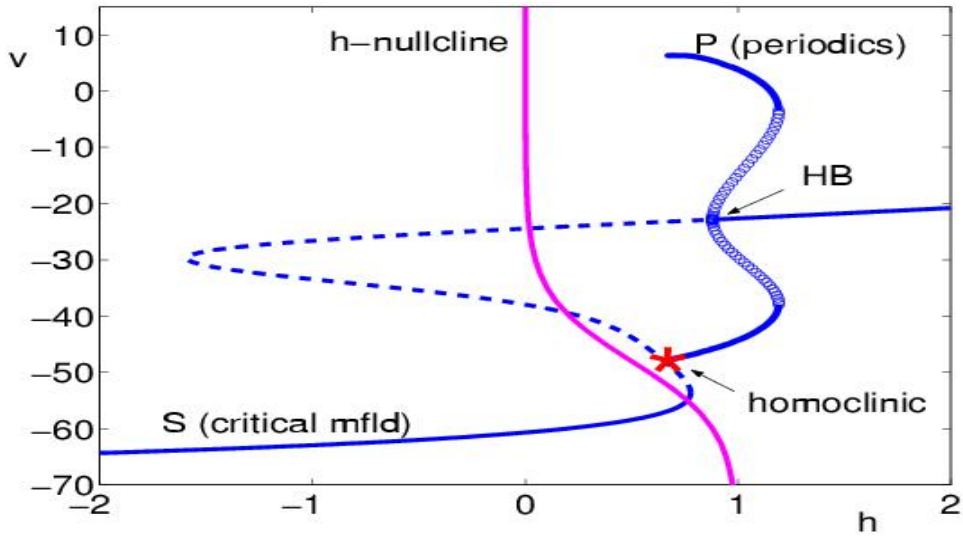

Figure 1: Bifurcation diagram for $g_{syn} = 0$ and $g_{ton} = 0.2$ [5]*(Copyright (c)2005 Society for Industrial and Applied Mathematics. Reprinted with permission. All rights reserved)*

.

h-nullcline with the critical manifold S is a fixed point of the whole system. A *homoclinic point* (*HP*), indicated as *homoclinic* in the figure, is the point where the curve of periodic orbits P ends. At this point, the period of the periodic orbits tends to infinity. If the curve of periodics P loses stability before the period goes to infinity then the intersection of the stable branch of P with its unstable branch is a saddle point for P, denoted by SN^p. Another way of seeing how dramatic changes in period are near HP is shown in figure 2. In this figure, one can see that far enough from HP the period of P does not change much, but closer to the homoclinic it grows relatively fast with small changes of the control parameter h. The curve S, in figure 1, represents the curve of fixed points for the fast subsystem. For fixed values of h, the fast subsystem may have up to 3 fixed points which can be stable or unstable. In order to determine stability of a fixed point, fix $h = h^*$ and draw a vertical line passing through it. Any intersection of $h = h^*$ with S occuring on the dashed part of S, represents an unstable fixed point. Similarly, an intersection of $h = h^*$ with S on the solid part of S represents a stable fixed point. Moreover, the point where the stable and unstable branches

of S meet is called a saddle node point (SN). Finally, there is a (subcritical or supercritical) Hopf bifurcation (HB) which gives rise to P [32]. The curve S divides the curve P in two branches. The top and bottom branches represent, respectively, the maximum and minimum voltages of a given periodic orbit for a particular value of h. Note that, as h decreases the amplitudes of the periodic orbits increase along with the periods of the oscillations.

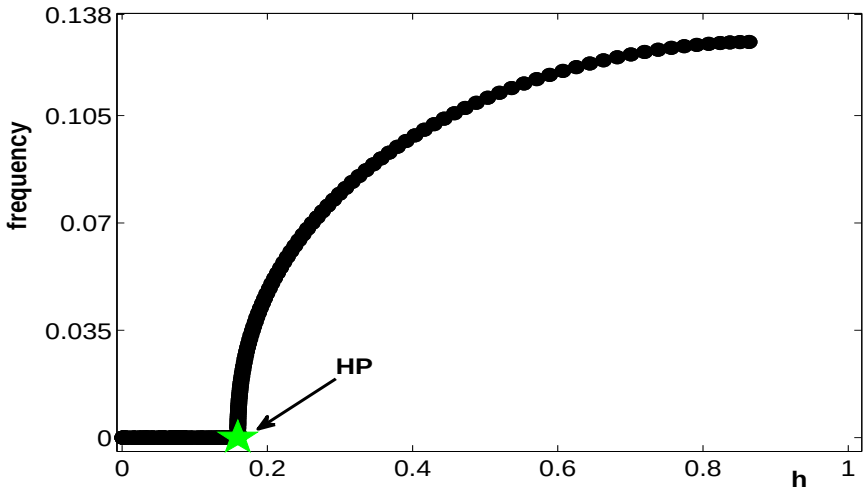

Figure 2: Example of how fast frequency grows near the homoclinic point HP, for $g_{syn} = 3$ and $g_{ton} = 0.91$ and all other parameters fixed as in table 1.

From the full set of parameters involved in this system of differential equations, it has been determined numerically that the parameters g_{syn}, g_{ton}, g_{NaP} play an important role in the dynamics of the whole system for the preBötC [6]. Figure 3 illustrates, in a bifurcation diagram, how changes in g_{NaP} affect the dynamics of the cell when all other parameters are fixed. It is clear from this picture that, as g_{NaP} is increased, the curve of periodic orbits moves to the left. Analogously, when g_{syn} or g_{ton} are varied with all other parameters fixed, the curve of periodics P moves to the left [5]. As for the curve S, it moves leftward when g_{NaP} and g_{ton} increase whereas it remains practically constant when g_{syn} is varied [5]. This means that, the range of values for which a cell is active will strongly depend on changes in the parameter set.

In figure 4, an experiment *in vitro* with slice preparations of a rat's brainstem shows

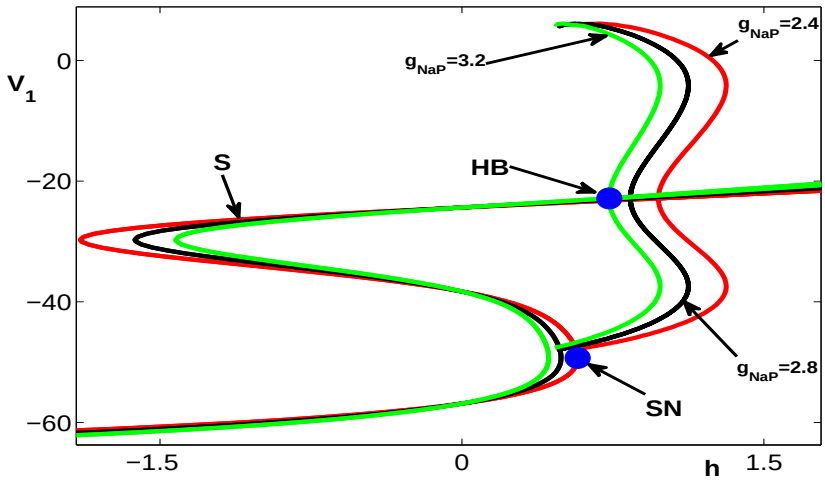

Figure 3: Bifurcation diagram corresponding to all parameter values fixed except g_{NaP}. The reference values for this plot were taken from [6]. Here $g_{syn} = 4$ and $g_{ton} = 0.4$.

that some bursting activity in the preBötC, without any stimulus, can be observed [12]. In this experiment, macropatch electrodes were applied to the pre-BötC and $XIIn$ regions and readings of consecutive inspiratory bursts were obtained. These readings are shown directly as they were obtained in the experiment as well as after some filtering of these data.

As mentioned before, Butera's minimal model [6] can reproduce experimental results when two parameters, g_{syn} and g_{ton}, are varied, giving rise to a variety of behaviors: *quiescence* - cell shows no sign of activity, i.e., the system goes to a stable solution without action potentials; *bursting* - cell has action potentials, followed by a period of recovery without spikes; and *spiking*, where the cell is firing constantly. In the bursting regime, if for a certain parameter value h the cell is firing, then h decreases, until it reaches a minimum value for which the cell falls to the lower branch of the curve S. Then, the parameter h starts increasing until it reaches the SN point and it jumps back to the active phase, continuing this cycle over and over again. The frequency of such action potentials can last from a few miliseconds to up to hundreds of miliseconds depending on the parameter set. In all simulations, g_{syn} and g_{ton} are varied but are the same for the two homogeneous cells, and can be equal or

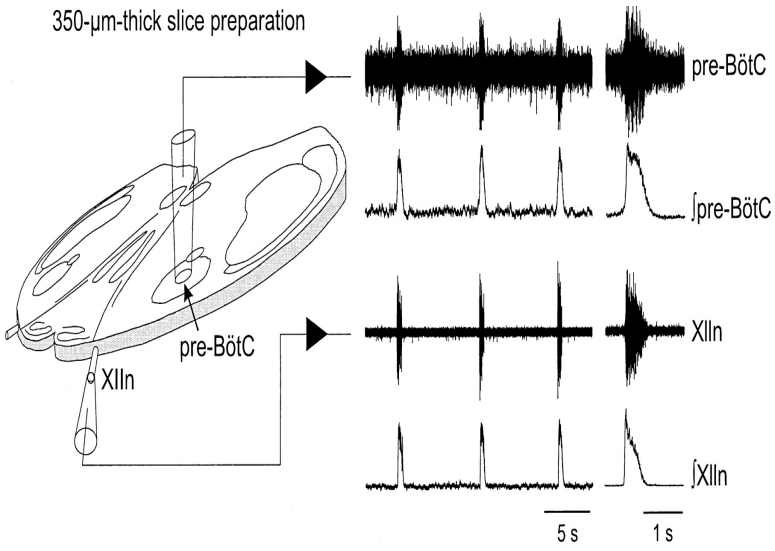

Figure 4: Figure 1 from [12] showing a slice preparation of a rat's brain *in vitro* . In this picture is also shown the hypoglossal nerve $XIIn$ from where inspiratory motor discharges has been recorded(*used with permission from Journal of Neurophysiology*).

different for two heterogeneous cells. How changes in the synaptic and tonic input promote different types of dynamics in a network of two coupled cells is depicted in figure 5.

In figure 5(A)-(C), $g_{ton} = 0.77$, and $g_{syn} = 0.28, 3, 8.4$, respectively. In these plots, notice that for a low value of g_{syn}, the network is spiking. With increasing g_{syn}, the network presents bursting solutions and for a big enough synaptic input the network goes back to spiking again. In figure 5(C)-(E), fixing $g_{syn} = 8.4$ and decreasing g_{ton}, the network goes from spiking to bursting and then to silence. This picture shows the important role of g_{syn} and g_{ton} on determining the different regimes a small network of cells may be engaged. In the figure 5 (F), a cartoon shows how g_{syn} and g_{ton} can influence the dynamics of the two cells.

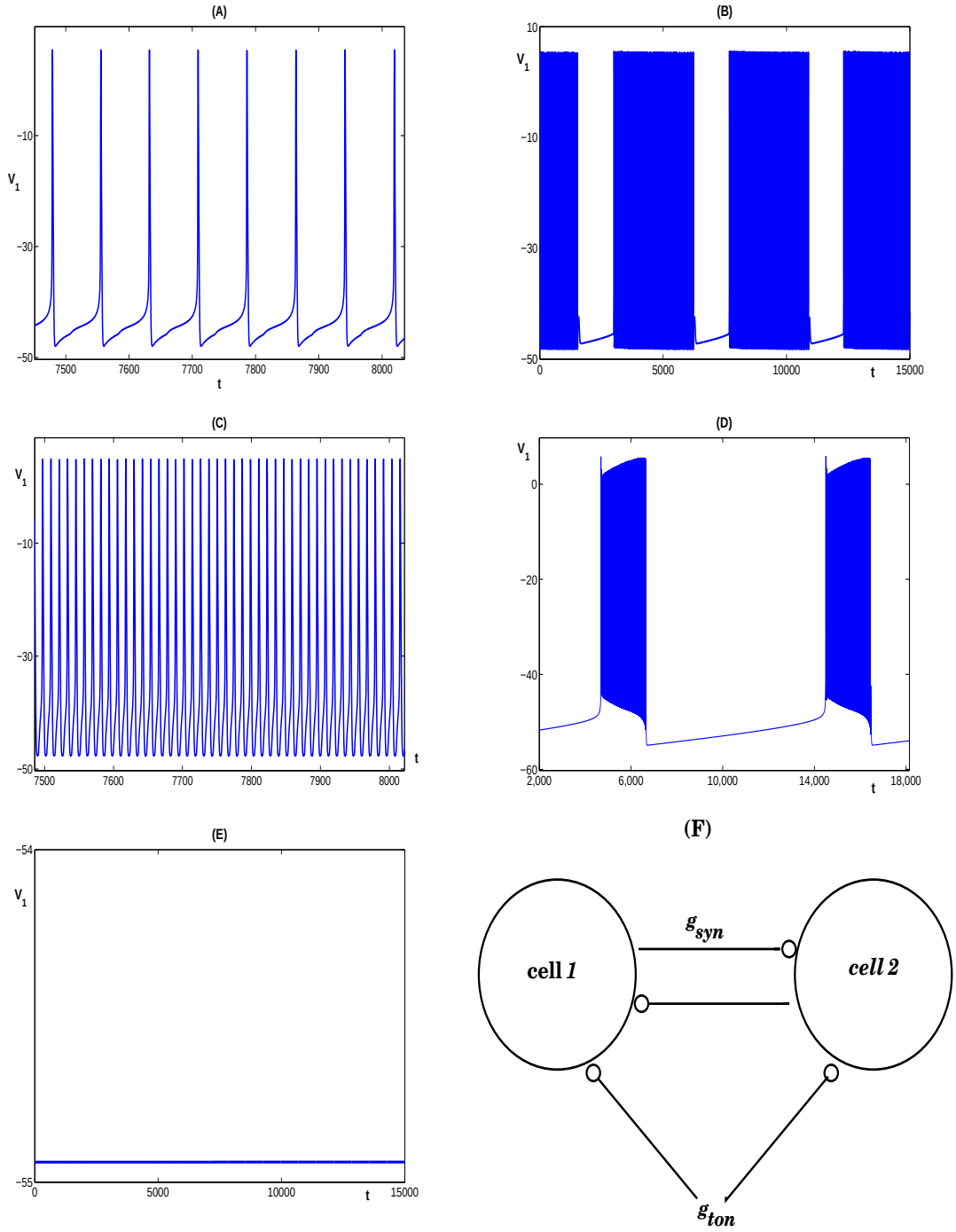

Figure 5: Pictures showing how varying g_{syn} and g_{ton} with all other parameters fixed can give rise to *quiescence*, *bursting* and *spiking* for a network of two cells. $(A) - (C)$ Fixing $g_{ton} = 0.77$ and varying g_{syn} from 0.28 to 3 and then to 8.4, the system goes from spiking to bursting and back to spiking. (C)-(E) Fixing $g_{syn} = 8.4$ and decreasing the value of g_{ton} from 0.77 to 0.42 and then to 0.20, the system goes from spiking to bursting and then, for low enough g_{ton} the cells are silent. (F) A cartoon show how g_{syn} and g_{ton} contribute to the dynamics of the two cells

.

In order to fully understand the role of these two parameters in a small network of preBötC cells, Best *et al* [5] made a thorough analysis in the self coupled single cell case and two-cell case. For the self coupled single cell case, the region in the parameter space (g_{ton}, g_{syn}) where the cell could be silent, burst or spike was determined. In the analysis, [5] used the slow variable h and took the limit of the parameter ϵ tending to zero.

This singular perturbation analysis [30, 42], for the self coupled single cell case significantly underestimated the region of bursting for the case of two coupled cells.

Consider now the two-cell case. In order to determine a curve in the parameter space (g_{ton}, g_{syn}) separating regions where the two cells could be bursting, spiking or silent, Best *et al* [5] used the averaged slow variables

$$\dot{h}_i = \frac{1}{T_s(h_1,h_2)} \int_0^{T_s(h_1,h_2)} g_i(v_i) d\xi \qquad i = 1,2, \tag{2.2.1}$$

where $g_i(v_i) \equiv \epsilon \frac{(h_\infty(v_i)-h_i)}{\tau_h(v_i)}$ and $T_s(h_1,h_2)$ is the period of the periodic orbit being averaged. The averaged nullclines can be computed numerically as in [5], using the following procedure.

First, regarding h_1 and h_2 as parameters, compute, on the $(h_1,h_2)-$plane, O and Ω defined as the oscillatory region and the boundary of the oscillatory region, respectively, as follows. Without loss of generality, suppose that for a fixed pair (h_1^*, h_2^*) the fast subsystem is active. Keep h_1^* fixed and vary systematically h_2 from h_2^* to lower values, in small steps, until the fast subsystem falls into quiescence. Record the pair (h_1^{1u}, h_2^{1u}) for which this transition happened ($h_1^{1u} = h_1^*$). Fix another pair (h_1, h_2) for which the fast subsystem is active with $h_1 = h_1^{1u} - \Delta$, $0 < \Delta \ll 1$. Vary h_2 until the fast subsystem falls into quiescence and again record this new pair (h_1^{2u}, h_2^{2u}) with $h_1^{2u} = h_1^{1u} - \Delta$. Perform this procedure until for a given initial pair (h_1, h_2) the system gives you quiescence for all h_2 and a fixed h_1. At this stage, you have a sequence of points $(h_1^{1u}, h_2^{1u}), (h_1^{2u}, h_2^{2u}), \ldots$, forming a curve separating the active and silent regions. Start again this whole process, at say (h_1^*, h_2^*) again but this time fix h_2^* and systematically vary h_1 in order to find another sequence of points $(h_1^{1f}, h_2^{1f}), (h_1^{2f}, h_2^{2f}), \ldots$, forming another curve separating the active and silent regions. All these computed pairs form what [5] called the boundary of the oscillatory region and which we denoted by Ω. The region to the right of Ω is the oscillatory region O and on the left there is the silent region, denoted here by $\mathbf{Q_f}$. A cartoon depicting these regions is shown in figure 6.

Now, let's describe how to get the h_1 and h_2 averaged nullclines. Fix a pair (h_1, h_2) in O. Compute the period of the corresponding periodic orbit $T_s(h_1, h_2)$. Integrate the fast subsystem together with equations (2.2.1). Vary systematically one of the parameters while keeping the other fixed, to find pairs (h_1, h_2) within O such that either $\dot{h}_1 = 0$ or $\dot{h}_2 = 0$ or both.

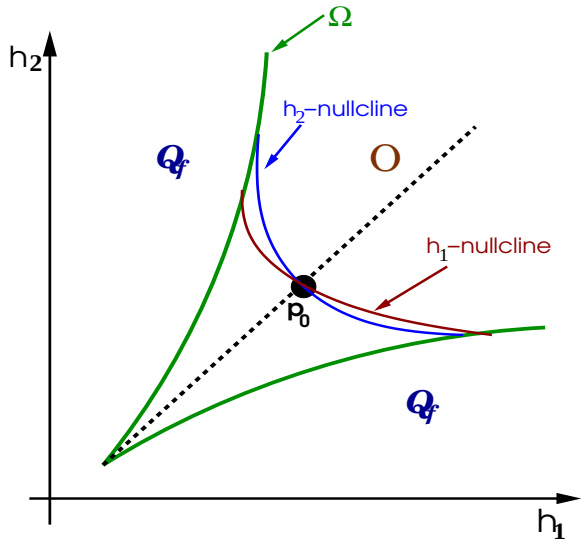

Figure 6: Cartoon of a typical region on the (h_1, h_2) for fixed values of the parameters. In blue and red are the averaged h_1 and h_2 nullclines intersecting at a point p_0, which, if it exists, can be either stable or unstable. The regions denote by $\mathbf{Q_f}$ are regions where the cell is silent. The region containing the nullclines and inside the green region Ω, the boundary of oscillatory region, is a region where both cells are active and it will be denoted by O.

The set of pairs (h_1, h_2) for which $\dot{h}_1 = 0$ forms the h_1 averaged nullcline and the pairs (h_1, h_2) such that $\dot{h}_2 = 0$ forms the h_2 averaged nullcline. If for no pairs (h_1, h_2) $\dot{h}_i = 0$ $i = 1, 2$, then the averaged nullclines are outside O.

The numerical computation of the averaged nullclines helped [5] in distinguishing between the different regimes. These different regimes were defined based on whether the averaged nullclines were inside or outside O; on the number of intersections of these averaged nullclines within the active region along with their stability; whether trajectories in O leave or not O as well as whether trajectories were oscillating around the identity line.

Varying systematically $g_{syn}(g_{ton})$ for fixed $g_{ton}(g_{syn})$, Best *et al* [5] determined curves in the parameter space (g_{ton}, g_{syn}) for which two identical coupled cells were either silent, bursting or spiking, with all other parameters fixed. The 4 different regions found are shown in figure 7 and are described below. One representative of each region in figure 7 is shown in figure 8. For all examples in figure 8, $g_{syn} = 3$.

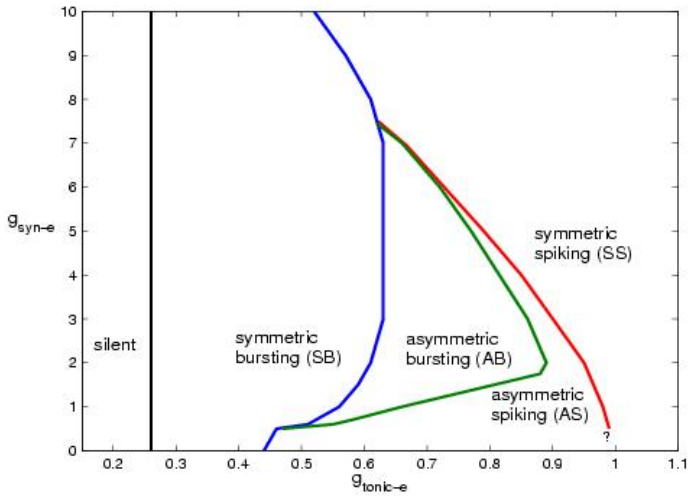

Figure 7: Boundaries for different regimes of activity on the parameter space (g_{ton}, g_{syn})[5] *(Copyright (c)2005 Society for Industrial and Applied Mathematics. Reprinted with permission. All rights reserved)*

.

1. *Symmetric Bursting* (**SB**)(figure 8(A)): In this region, $\dot{h}_1 < 0$ and $\dot{h}_2 < 0$ for all pairs $(h_1, h_2) \in O$. After a transient, trajectories of the full system (2.3.1)- (2.3.4) in O oscillate symmetrically around the identity line leaving O through Ω. At this time, the cell falls to the lower branch of S and h starts increasing again until SN is reached and then the cells enter the active phase again;
2. *Asymmetric Bursting* (**AB**)(figure 8(B)): Averaged nullclines come inside O and intersect at a point p_0 on the $h_1 = h_2$ line and p_0 is unstable, due to the configuration of the nullclines. Starting with initial conditions such that $h_2 > h_1$ ($h_2 < h_1$), trajectories of the full system in O will remain above (below) the identity line and cross either $\dot{h}_1 = 0$

or $\dot{h}_2 = 0$ or perhaps both, leaving O through Ω;

3. *Asymmetric Spiking* (**AS**)(figure 8(C)): Averaged nullclines are still inside O, but this time they intersect at 3 distinct points, p_0 (unstable) and q_A and q_B (stable). Trajectories of the full system starting in O with initial conditions such that $h_2 > h_1$ stay above the identity line and go to q_A, never leaving O whereas if initial conditions are such that $h_2 < h_1$ then trajectories of the full system go to q_B;
4. *Symmetric Spiking* (**SS**)(figure 8(D)): Only a fixed point p_0 exists with $h_1 = h_2$. Trajectories of the full system in O oscillate symmetrically around the identity line and get trapped in the stable fixed point p_0, never leaving O.

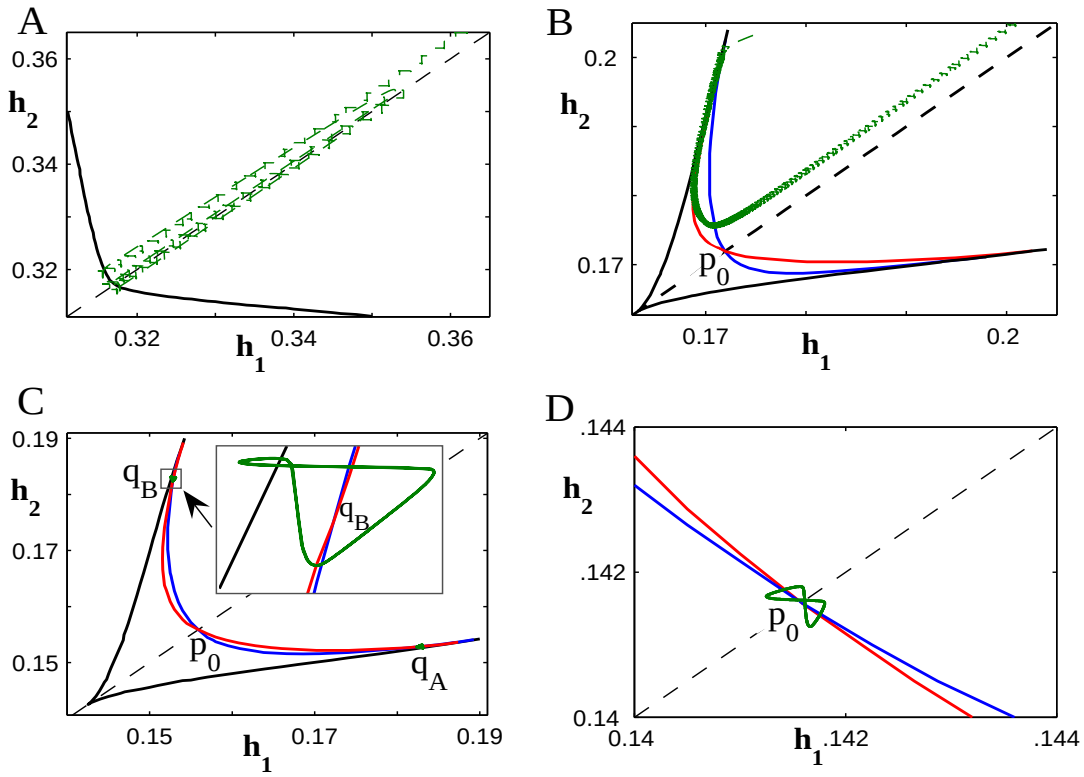

Figure 8: Plot of the 4 cases mentioned above for $g_{syn} = 3$ and $g_{ton} = 0.56$, $g_{ton} = 0.83$, $g_{ton} = 0.87$ and $g_{ton} = 0.91$, respectively. Figure reproduced from [5]*(Copyright (c)2005 Society for Industrial and Applied Mathematics. Reprinted with permission. All rights reserved)*

.

The fact that there are 3 fixed points in O in the **AS** region dropping down to a single fixed point in **SS** when g_{ton} is increased suggests the presence of a pitchfork bifurcation of periodics.

As a final remark, in all simulations of the full system (2.1.1)-(2.1.4), the action potentials for each cell could theoretically occur exactly at the same time for the duration of the simulation, in which case, we say that the cells are in synchrony or in-phase (IP); or the action potentials for one cell could occur exactly when the other cell is at its minimum voltage in which case we say that the cells are not in synchrony or anti-phase AP. As noted in [5], for mostly every initial condition cells are AP. The only case when an IP solution exists is when starting with initial conditions such that $v_1 = v_2$, $n_1 = n_2$, $s_1 = s_2$ and $h_1 = h_2$, in regions **AB**, **AS** and **SS**. That is, for all $t > 0$, $v_1(t) = v_2(t)$, $n_1(t) = n_2(t)$, $s_1(t) = s_2(t)$ and $h_1(t) = h_2(t)$, is required to achieve IP behavior. Any slight perturbation on the initial conditions brings the IP to the AP solution. In figure 9, a bifurcation diagram for $g_{syn} = 3$ and $g_{ton} = 0.91$ shows on a v_1^{max} versus h plot, how close the IP and AP solutions are.

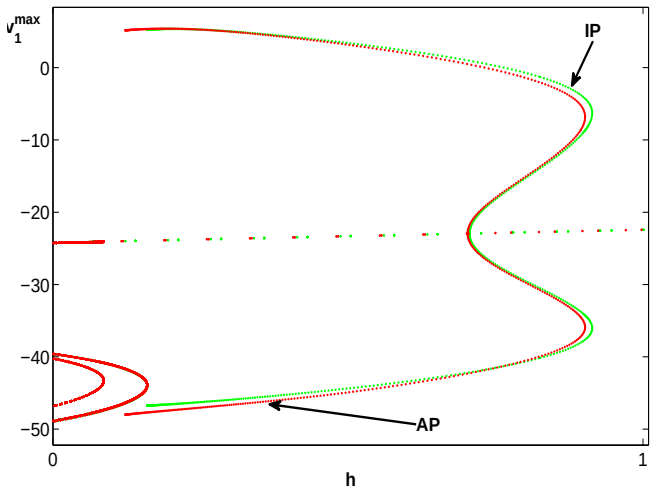

Figure 9: Bifurcation diagram for the full system (2.1.1)-(2.1.4) with $h_1 = h_2 = h$ for $g_{syn} = 3$ and $g_{ton} = 0.91$ showing the IP and AP solutions, for $h = h_1 = h_2$. Notice how close to each other these solutions really are.

.

2.3 MODIFICATIONS OF THE ORIGINAL SYSTEM

In this section, the change of variables $t = 10T$, $v = 100V$, and $\bar{g^*}_i = \frac{\bar{g}_i}{\bar{g}_{Na}}$ (maximal conductances) is applied to the original set of equations (2.1.1)-(2.1.4). There is no particular justification for this change of variables except that it keeps voltages on the interval (-1,1). Equations (2.1.1)-(2.1.4) become:

$$\frac{dV_i}{dT} = \frac{-I_{NaP}(V_i) - I_{Na}(V_i) - I_K(V_i) - I_L(V_i) - I_{ton}(V_i) - I_{syn}(V_i)}{\rho} \tag{2.3.1}$$

$$\frac{dh_i}{dT} = \epsilon^* \tau_h(V_i)(h_\infty(V_i) - h_i) \tag{2.3.2}$$

$$\frac{dn_i}{dT} = \frac{n_\infty(V_i) - n_i}{\tau_n(V_i)} \tag{2.3.3}$$

$$\frac{ds_i}{dT} = \alpha_s(1 - s_i)s_\infty(V_j) - \frac{s}{\tau_s} \tag{2.3.4}$$

for $i, j = 1, 2$ and $j = 3 - i$ where

$$\rho = \frac{C}{10\bar{g}_{Na}} = 7.5 \times 10^{-2}; \quad \epsilon^* = 10^{-3}; \quad \alpha_s = 2; \quad \tau_s = \frac{\bar{\tau}_s}{10} = 0.5$$

All other equations are as before, replacing v by $100V$ and the E_i's with $i \in \{Na, L, K, syn\}$, as defined in table 1, were all divided by 100. In equation (2.3.2), notice that $\tau_h(V_i)$ is now multiplying instead of dividing $(h_\infty(V_i) - h_i)$ as it occurred in equation (2.1.2). So, $\tau_h(V_i)$ has been written as

$$\tau_h(V_i(t)) = cosh\left(\frac{V_i(t) + 0.48}{0.12}\right) \tag{2.3.5}$$

Some parameter values of the nondimensional system shown above are summarized in table 2.

$\bar{g}^*_{NaP}$	$\bar{g}^*_{Na}$	E^*_{Na}	$\bar{g}^*_K$	E^*_K	$\bar{g}^*_L$	E^*_L	$\bar{g}^*_{ton}$	E^*_{syn}	$\bar{g}^*_{syn}$
0.1	1	0.5	0.4	-0.85	0.1	-0.65	[0;0.0357]	0	[0;0.5357]

Table 2: Nondimensional form of parameters in table 1. Here, $\bar{g}^*_i = \frac{\bar{g}_i}{28}$ and $E^*_i = \frac{E_i}{100}$

.

Henceforth, we will be using and referring to the set of equations (2.3.1)-(2.3.4) for our analysis and map reductions, unless otherwise noted.

3.0 THE ONE DIMENSIONAL MAP

In the last chapter a brief review was made on numerical results on a minimal model for preBötC cells relating some important parameters of the system with what is experimentally being seen. Also a review was given of the results of a thorough analysis in parameter space by [5] that determined regions associated with different regimes. In this chapter, a background on the relation between maps with the dynamics of systems of ordinary differential equations modeling neuronal activity in the brainstem is shown. A mathematical reduction of the 4 dimensional system of ordinary differential equations (2.3.1)-(2.3.4) with $i = j = 1$ to a one dimensional map is derived. After the map is obtained an analysis follows explaining some properties of the map. Some analytical results are shown along with numerical corroboration.

3.1 BACKGROUND

In figure 10, let $\Phi(t)$ be a time-dependent oscillatory solution of a system of differential equations $\dot{\mathbf{y}}(t) = f(\mathbf{y})$ where $f(\mathbf{y})$ is a function modeling, for instance, a particular neural network and $\mathbf{y} \in \Re^n$. Suppose that at time $t = 0$, $\Phi(0)$ is at the cross-section Σ. Let $\Phi(t)$ evolve in time. Then, after a time $t = t_1$ is elapsed, $\Phi(t)$ crosses Σ for the first time. Suppose that each subsequent oscillation takes a time t_i for $i = 2, 3, \ldots$ to return to the cross section Σ. Then, for each return to Σ a new point is drawn. The resulting set of points forms, on Σ, what is called a first return map, or simply a map. Mathematically, this map can be described as

$$\mathbf{x}_{n+1} = P(\mathbf{x}_n) \tag{3.1.1}$$

where $P(\mathbf{x}_n)$ is a linear or nonlinear continuous function which takes $\mathbf{x}_n$ into $\mathbf{x}_{n+1}$, $\mathbf{x} \in \Re^{n-1}$ with $n \in \aleph$. Here we are assuming that $f(\mathbf{y})$ is a continuous function with a continuous dependence on its parameters. As we will see later, the n^{th} dimensional flow could have been projected to a lower dimension map than $n-1$, for $n \geq 3$. This map allows one to extract information from the flow $\Phi(t)$ by studying the dynamics of the map P. Depending on the system it is not always possible to determine a closed form for the map P.

Suppose that, for the sake of the argument, one knows a closed form for the map $P(x_n)$. Then use the formula for $P(x_n)$, starting with x_0 and compute $x_1 = P(x_0)$ and the next iterates $x_2, x_3, x_4, \ldots$ of the map using $x_1, x_2, \ldots$, respectively. If, for a given $n \in \aleph$, one finds that $P(x_n) = x_n$, then x_n is called a fixed point of the map P. In terms of $\Phi(t)$, this implies that the return to the cross section takes place every $t = T$ units of time. In other words, $\Phi(t)$ is periodic with period T. Denote the fixed point of P by x^*. Then, the stability of x^*, on Σ, determines whether the oscillatory solution is stable or not. Furthermore, the advantage of using the map is that the analysis of P is in general easier than the study of the full dynamical system, due to the lower dimension of P.

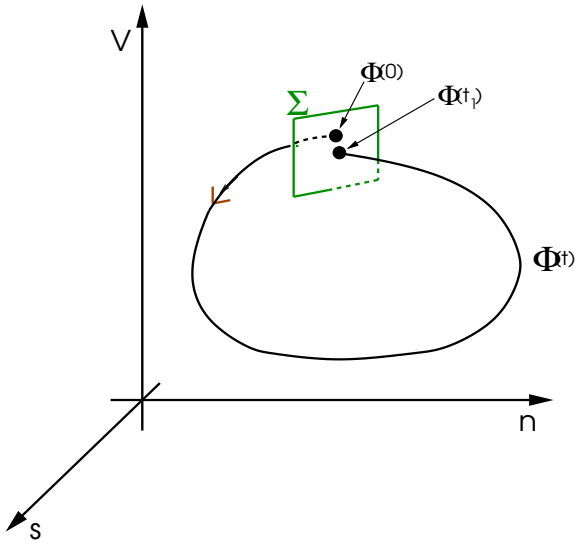

Figure 10: Sample of a time-dependent oscillatory solution $\Phi(t)$ on the (V,n)-plane for a fixed value of h. Starting with a initial condition $\Phi(0)$ on a cross-section Σ, a second point $\Phi(t_1)$ is recorded on Σ signaling a return to the section after a time $t = t_1$ has elapsed.

Among many studies studies of continuous systems of equations through maps, we can cite a one dimensional discontinuous map obtained from a three dimensional system describing the Belousov-Zhabotinskii reaction [47]. The study of this map yielded analytical explainations for some features of the three dimensional model as well as predictions of some bursting behavior [48]. In [37], a one dimensional map is obtained for a model of the pancreatic β-cells using fast/slow decomposition and bifurcation analysis in terms of the slow variable and averaging over the fast subsystem. In the next section, using a similar methodology as in [37], an analytical expression for a one dimensional map is derived by separating the full system of equations (2.3.1)-(2.3.4) into its slow (h) and fast (V, n and s) components [27].

3.2 OBTAINING THE MAP

Consider the slow subsystem (2.3.2) for a fixed g_{syn}. Define $t(T)$ such that $\frac{d}{dt} = \frac{1}{\tau_h(V)}\frac{d}{dT}$. Then, $t(T) = \int_0^T \tau_h(V(\xi))d\xi$ and equation (2.3.2) simplifies to,

$$\frac{dh}{dt} = \epsilon(h_\infty(V) - h) \tag{3.2.1}$$

In the (V, n, s)-space, let Σ be a local transversal section to the fast dynamics on this space and $\Phi(t) = (V(t), n(t), s(t))$, be the solution of the fast subsystem $\dot{\Phi}(t) = (\dot{V}(t), \dot{n}(t), \dot{s}(t))$. Suppose that on Σ, $\dot{V} = 0$ and without loss of generality, assume that V is at its minimum. We also need, at this point that, $\dot{n}(t) \neq 0$ or otherwise we will never cross transversely through Σ on the (V, n)-plane.

Proposition 3.2.1. *Suppose that at some time $t = t_0$, $\dot{V} = 0$. Without loss of generality, suppose that V is at its minimum at t_0, that is, $V = V_{min}$. Then, $\dot{n} \neq 0$ at $t = t_0$.*

Proof. By contradiction, assume that $\dot{V} = 0$ and $\dot{n} = 0$ at $t = t_0$. Without loss of generality assume that both are at their minimum values. Then, differentiating equation (2.3.3) with

respect to t gives

$$\frac{d}{dt}\left(\frac{dn}{dt}\right) = \frac{\frac{d}{dt}\left(n_\infty(V)-n\right)\tau_n(V)-\left(n_\infty(V)-n\right)\frac{d\tau_n(V)}{dt}}{\tau_n(V)^2} \tag{3.2.2}$$

$$= \frac{\left(\frac{dn_\infty(V)}{dV}\frac{dV}{dt}-\frac{dn}{dt}\right)\tau_n(V)-\left(n_\infty(V)-n\right)\frac{d\tau_n(V)}{dV}\frac{dV}{dt}}{\tau_n(V)^2}. \tag{3.2.3}$$

Now, evaluating this last expression at $t = t_0$ gives us that

$$\frac{d^2n}{dt^2} = 0. \tag{3.2.4}$$

Contradiction, since in a sufficiently small neighborhood of $t = t_0$, $n(t)$ is concave up and, therefore, the second derivative of n with respect to t should be always positive there. □

Numerical evidence also show that $\dot{V} = 0$ implies $\dot{n} \neq 0$. Suppose that at $t = 0$, $\Phi(0) = (V(0), n(0), s(0))$ is on Σ. Let t_s be the time that it takes for $\Phi(t)$ to reach Σ again. Define the first return map by

$$P(\eta) = h(t_s(\eta)) \tag{3.2.5}$$

where $\eta = h(0)$ and $t_s(\eta)$ is defined as

$$t_s(\eta) = min\{t > 0 \mid (V(t), n(t), s(t)) \in \Sigma \quad and \quad \dot{n} < 0\}.$$

Adding ϵh on both sides of equation (3.2.1) and multiplying it by its integrating factor $e^{\epsilon t}$ we get

$$\frac{d}{dt}(e^{\epsilon t}h) = e^{\epsilon t}\epsilon h_\infty(V) \tag{3.2.6}$$

Integrating the last equation from 0 to $t_s(\eta)$,

$$e^{\epsilon t_s(\eta)}h(t_s(\eta)) - h(0) = \epsilon\int_0^{t_s(\eta)} h_\infty(V)e^{\epsilon t}dt$$

But, according to our previous definition, $h(t_s(\eta)) = P(\eta)$ and $h(0) = \eta$. Thus, we obtain the equation for the first return map for the self coupled case

$$P(\eta) = e^{-\epsilon t_s(\eta)}\eta + \epsilon\int_0^{t_s(\eta)} h_\infty(V)e^{\epsilon(t-t_s(\eta))}dt. \tag{3.2.7}$$

Define a function [37],

$$F(\eta) = \frac{\int_0^{t_s(\eta)} h_\infty(V) e^{\epsilon(t-t_s(\eta))} dt}{\int_0^{t_s(\eta)} e^{\epsilon(t-t_s(\eta))} dt}. \tag{3.2.8}$$

Some algebraic manipulations allow us to write equation (3.2.7) as

$$P(\eta) \;\; = \;\; e^{-\epsilon t_s(\eta)}(\eta - F(\eta)) + F(\eta) \tag{3.2.9}$$

If $\eta \neq F(\eta)$, that is, if $\eta - F(\eta) = \Delta \neq 0$, then the right hand side of (3.2.9) becomes

$$e^{-\epsilon t_s(\eta)}(\eta - F(\eta)) + F(\eta) = e^{-\epsilon t_s(\eta)}\Delta - \Delta + \eta = \eta + \Delta(e^{-\epsilon t_s(\eta)} - 1) \neq \eta. \tag{3.2.10}$$

It is clear from equation (3.2.9) that the behavior of $P(\eta)$, depends on $F(\eta)$. Therefore, it becomes helpful to look at $F(\eta)$ and check its properties first, before drawing conclusions about $P(\eta)$.

3.2.1 Some properties of $F(\eta)$

First, assume that the curve of periodic orbits ends in a HP (homoclinic point). Denote the value of η at HP by η_{HC}. Assume also that g_{syn} is fixed. In chapter 2, figure 2, it is shown that far enough from the HP, the period of the periodic does not vary much with changes in h. As a consequence, the time that the periodic orbit takes to return to Σ will be approximately the same as η varies, that is, $t_s(\eta) \approx t_s^0 = constant$. Then, we can write the numerator of equation (3.2.8) as

$$\int_0^{t_s(\eta)} h_\infty(V) e^{\epsilon(t-t_s(\eta))} dt = \int_0^{t_s^0} h_\infty(V) e^{\epsilon(t-t_s(\eta))} dt + \int_{t_s^0}^{t_s(\eta)} h_\infty(V) e^{\epsilon(t-t_s(\eta))} dt \tag{3.2.11}$$

These 2 terms on the right hand side (RHS) correspond, respectively, to the dynamics far away and close to HP. If we are far enough from the homoclinic then the second term on the RHS of equation (3.2.11) is small, since the period of the periodic orbits is approximately t_s^0. Near the homoclinic, the first integral on the RHS of (3.2.11), can be written as

$$\int_0^{t_s^0} h_\infty(V) e^{\epsilon(t-t_s(\eta))} dt = e^{\epsilon(t_s^0 - t_s(\eta))} \int_0^{t_s^0} h_\infty(V) e^{\epsilon(t-t_s^0)} dt \tag{3.2.12}$$

The second integral on the RHS, since we are close to the homoclinic and the V values do not change very much, we will assume, without loss of generality, that $h_\infty(V) \simeq h_\infty(V_{HC})$, where $V = V_{HC}$ is the value of V at HP. Then, equation (3.2.11) becomes

$$\int_0^{t_s(\eta)} h_\infty(V) e^{\epsilon(t-t_s(\eta))} dt \approx e^{\epsilon(t_s^0 - t_s(\eta))} \int_0^{t_s^0} h_\infty(V) e^{\epsilon(t-t_s^0(\eta))} dt + h_\infty(V_{HC}) \int_{t_s^0}^{t_s(\eta)} e^{\epsilon(t-t_s(\eta))} dt$$

Some more algebra, simplifies the equation for $F(\eta)$ to

$$F(\eta) = \frac{e^{-\epsilon(t_s(\eta)-t_s^0)} A(\eta) + h_\infty(V_{HC})}{(1 - e^{-\epsilon t_s(\eta)})} \tag{3.2.13}$$

where $A(\eta) = \epsilon t_s^0 F_0(\eta) - h_\infty(V_{HC})$ and the equation for $F_0(\eta)$ is given by.

$$F_0(\eta) = \frac{\int_0^{t_s^0} h_\infty(V) e^{\epsilon(t-t_s^0)} dt}{(1 - e^{-\epsilon t_s^0})}.$$

Differentiating (3.2.13) with respect to η yields

$$\frac{dF}{d\eta} = \epsilon \frac{e^{-\epsilon(t_s(\eta)-t_s^0)} \left[t_s^0 \frac{dF_0}{d\eta} \left(1 - e^{\epsilon t_s(\eta)}\right) - \frac{dt_s(\eta)}{d\eta} \left(A(\eta) + h_\infty(V_{HC}) e^{-\epsilon t_s^0} \right) \right]}{(1 - e^{-\epsilon t_s(\eta)})^2} \tag{3.2.14}$$

In (3.2.13), $t_s(\eta) - t_s^0$ can be written as

$$t_s(\eta) - t_s^0 = \int_0^{T_s(\eta)} \tau_h(V) d\xi - \int_0^{T_s^0} \tau_h(V) d\xi = \int_{T_s^0}^{T_s(\eta)} \tau_h(V) d\xi. \tag{3.2.15}$$

where $T_s(\eta)$ and T_s^0 are defined similar to $t_s(\eta)$ and t_s^0, respectively. Near HP, $\tau_h(V) \approx \tau_h(V_{HC})$ where $V_{HC} = V(t)\,|_{\eta=\eta_{HC}}$, since $V(t)$ does not change much with t. Then,

$$t_s(\eta) - t_s^0 \;\approx\; \tau_h(V_{HC})(T_s(\eta) - T_s^0) = -(log(d(\eta - \eta_{HC})))^{\mu\tau_h(V_{HC})} + h.o.t. \tag{3.2.16}$$

where μ^{-1} is the positive eigenvalue of the matrix of linearization of the fast subsystem near HP [37]; $d = |f'(\eta_{HC})| \neq 0$, where $f(\eta)$ is the split function which measures the distance between the branches of the stable and unstable manifolds corresponding to the fast subsystem near HP [37, 32].

Let $\sigma = \epsilon\mu\tau_h(V_{HC})$.Then,

$$e^{-\epsilon(t_s(\eta)-t_s^0)} \;\approx\; (d(\eta - \eta_{HC}))^\sigma. \tag{3.2.17}$$

Note that when $\epsilon \to 0$, $(d(\eta - \eta_{HC}))^\sigma \to 1$. Near the homoclinic we also have,

$$\epsilon \int_{t_s^0}^{t_s(\eta)} h_\infty(V) e^{\epsilon(t - t_s(\eta))} dt \quad \approx \quad h_\infty(V_{HC})(1 - (d(\eta - \eta_{HC}))^\sigma). \tag{3.2.18}$$

Thus, we can write (3.2.14) as

$$\frac{dF}{d\eta} \quad = \quad \frac{\epsilon[d(\eta - \eta_{HC})]^\sigma \left[t_s^0 \frac{dF_0}{d\eta} (1 - e^{-\epsilon t_s}) - \frac{dt_s}{d\eta} \left(\epsilon t_s^0 F_0 + h_\infty(V_{HC})(e^{-\epsilon t_s^0} - 1) \right) \right]}{(1 - e^{-\epsilon t_s(\eta)})^2} \tag{3.2.19}$$

Let's take a close look into equation (3.2.19). According to previous analysis, $d^\sigma(\eta - \eta_{HC})^\sigma > 0$ (see equation (3.2.17)). Clearly, $t_s^0 > 0$ and $1 - e^{-\epsilon t_s(\eta)} > 0$. It can be easily shown using equation (3.2.8) that, $0 < F(\eta) < 1$ and $F(\eta)$ is a continuous and smooth function of η on some bounded interval $[\eta_0, \eta_1]$, and $\eta_{HC} < \eta_0$.

At last, differentiating $t_s(\eta)$ with respect to η, up to first order terms, yields

$$\frac{dt_s}{d\eta} = -\frac{\mu \tau_h(V_{HC})}{\eta - \eta_{HC}} = -\frac{\sigma}{\epsilon(\eta - \eta_{HC})} < 0 \tag{3.2.20}$$

where $\eta_{HC} < \eta$ for all $\eta \in [\eta_0, \eta_1]$.

Proposition 3.2.2. *If, for η sufficiently close to η_{HC}, $V(t) > V_{HC} \quad \forall \quad t$ then $\frac{dF}{d\eta} < 0$ in (3.2.19), for ϵ sufficiently small. Moreover, as $\eta \to \eta_{HC}^+$, $\frac{dF}{d\eta} \to -\infty$.*

Proof. What remains to be shown is that under the assumptions of Proposition 3.2.2 the term multiplying $\frac{dt_s(\eta)}{d\eta}$ is negative. Moreover, this term takes over the other the first term since both t_s^0 and $\frac{dF_0}{d\eta}$ are finite and $\frac{dt_s}{d\eta} \to -\infty$ as $\eta \to \eta_{HC}^+$. Recall that,

$$F_0(\eta) = \frac{\epsilon \int_0^{t_s^0} h_\infty(V) e^{-\epsilon(t - t_s^0)} dt}{1 - e^{-\epsilon t_s^0}} < h_\infty(V_{HC}) \frac{\epsilon \int_0^{t_s^0} e^{-\epsilon(t - t_s^0)} dt}{1 - e^{-\epsilon t_s^0}} = h_\infty(V_{HC}) \qquad \text{if } V(t) > V_{HC},$$

since $h_\infty(V)$ is a non-increasing function of V. Thus,

$$\begin{aligned} \epsilon t_s^0 F_0(\eta) + h_\infty(V_{HC})(e^{-\epsilon t_s^0} - 1) &= \epsilon t_s^0 F_0(\eta) + h_\infty(V_{HC})(1 - \epsilon t_s^0 - 1) + O(\epsilon^2) \\ &= \epsilon t_s^0 F_0(\eta) - \epsilon t_s^0 h_\infty(V_{HC}) + O(\epsilon^2) \\ &< \epsilon t_s^0 h_\infty(V_{HC}) - \epsilon t_s^0 h_\infty(V_{HC}) = 0, \end{aligned} \tag{3.2.21}$$

for ϵ sufficiently small. Since $\frac{dt_s(\eta)}{d\eta} < 0$ then the second term on the RHS of (3.2.19) is negative and it takes over the first term because

$$(\eta - \eta_{HC})^{\sigma} \frac{dt_s(\eta)}{d\eta} = \epsilon(\eta - \eta_{HC})^{\sigma} - \frac{\sigma}{\epsilon(\eta - \eta_{HC})} = -\frac{\sigma(\eta - \eta_{HC})^{\sigma-1}}{\epsilon} \to -\infty \qquad (3.2.22)$$

as $\eta \to \eta_{HC}^{+}$.

□

Moreover, when $\eta \to \eta_{HC}^{+}$, $t_s(\eta) \to \infty$ and equation (3.2.13) gives us that

$$F(\eta) \to h_{\infty}(V_{HC}) < 1 \qquad (3.2.23)$$

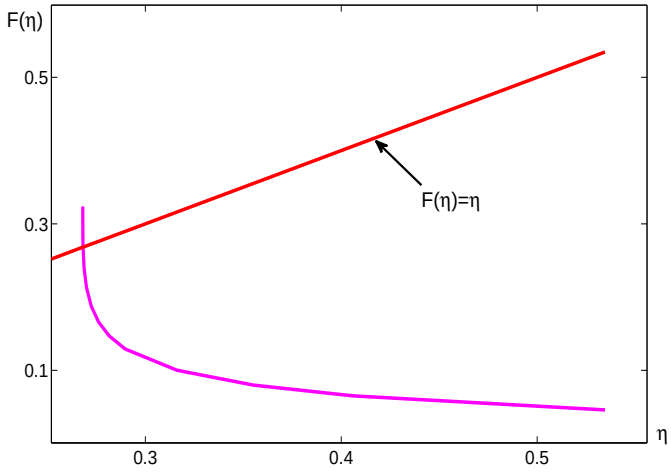

Figure 11: $F(\eta)$ for $g_{ton} = 0.025$ and $g_{syn} = 0.1$ (equivalent to $g_{ton} = 0.70$ and $g_{syn} = 2.8$, on the original system).

In summary $F(\eta)$ has the following properties, which were obtained either analytically (An) or numerically (Nu):

1. $0 < F(\eta) < 1$ for all η (An);
2. $F(\eta)$ is a monotone decreasing function of η for all $\eta < \eta_{HC}$ (Nu); (see figure 11)
3. $F(\eta) \to h_{\infty}(V_{HC})$ as $\eta \to \eta_{HC}^{+}$ (An);
4. For ϵ sufficiently small, $\frac{dF}{d\eta} \to -\infty$ as $\eta \to \eta_{HC}^{+}$ (An).

If our assumption about the existence of HP is false, then our curves of periodics can be observed numerically to end in a saddle node of periodics SN^p. At SN^p, the period of any stable oscillation achieves its maximum value and it does not go to infinity. Of the properties of $F(\eta)$ mentioned above, only the first two still hold true. The last two properties do not necessarily hold.

3.3 ANALYSIS OF THE MAP

According to the previous section, the analysis of the map has to take into account whether there exists a homoclinic point or not. This analysis will parallel what was previously done in [37].

Suppose there is a HP. Let η_{HC} be the value of η at the HP and η_L and η_R be the minimum and maximum values of η in the active phase. Suppose that the fast subsystem on the interval $(\eta_L, \eta_R]$ with $\eta_R \geq \eta_{HC}$ and $\eta_R > \eta_L$ is on the active phase. In the case HP exists, 3 distinct regions of the map are found and which will be discussed below.

3.3.1 Linear region $I_{linear} = [\eta_0, \eta_R]$ with $\eta_0 > \eta_L$

Recall figure 2. Assume that within I_{linear}, for all values of η, the period of the periodic orbits does not change much with η. So, by continuous dependence of solutions of equations (2.3.1)-(2.3.4) on ϵ, $t_s(\eta)$ can be approximated by

$$t_s(\eta) = t_s^0 + O(\epsilon) \tag{3.3.1}$$

where t_s^0 is constant throughout the interval. As a consequence of equation (3.3.1), the corresponding periodic orbit can be written as

$$(V(t), n(t), s(t)) = (V_0(t), n_0(t), s_0(t)) + O(\epsilon) \qquad 0 \leq t \leq t_s(\eta) \tag{3.3.2}$$

where $(V_0(t), n_0(t), s_0(t))$ with $t > 0$ is a periodic solution of the fast subsystem (2.3.1), (2.3.3) and (2.3.4) with initial conditions $\Phi(0)$.

Equations (3.3.1) and (3.3.2) allow for a linear analysis of the map $P(\eta)$. So, plugging in (3.3.1) and (3.3.2) into (3.2.9) and Taylor expanding the exponential function about t_s^0 yields

$$P(\eta) = (1 - \epsilon t_s^0)\eta + \epsilon t_s^0 F_0(\eta) + h.o.t.$$

where $F_0(\eta)$ is defined as before. According to the definition of $F_0(\eta)$, $\epsilon F_0(\eta)$ is a $O(\epsilon^2)$ term, which can be eliminated from linear analysis. Therefore,

$$P(\eta) = (1 - \epsilon t_s^0)\eta + O(\epsilon^2) \tag{3.3.3}$$

Differentiating (3.3.3) with respect to η yields:

$$\frac{dP}{d\eta} \approx 1 - \epsilon t_s^0 < 1 \tag{3.3.4}$$

From this linear analysis of $P(\eta)$, it can be concluded that, there exists η_0 far enough from HP such that $\dfrac{dP}{d\eta} < 1$ and $P(\eta_0) < \eta_0$.

3.3.2 Nonlinear region $I_{nonlinear} = (\eta_{HC}, \eta_0]$ with $\eta_{HC} \geq \eta_L$

In this region, it is assumed that small changes in η may imply a significant change in the period of the oscillations of the fast subsystem (2.3.1),(2.3.3) and (2.3.4) due to the closeness to HP, that is, $t_s(\eta)$ grows without bound, since $T_s(\eta)$ grows without bound. Let Σ_1 and Σ_2 be two two-dimensional cross sections dividing the periodic orbits of the fast subsystem near the homoclinic bifurcation, in the (V, n, s)-space, into two parts:

1. Starting at Σ_1 and going towards Σ_2 (away from HP), the time of flight is approximately t_s^0;
2. between Σ_2 and Σ_1 (near the homoclinic), we need to come up a way of determining a map connected to the map in the first part.

That is, starting at $\Phi(0)$ on Σ_1, integrate the fast subsystem until we hit Σ_2 at approximately time t_s^0, since we are far away from the homoclinic point . Define this map as P^u, as in equation (3.3.3). Let $P^u = \eta_1$. Starting with this initial condition on Σ_2 at time t_s^0 integrate the fast subsystem until you reach Σ_1 again. In order to set the map for this second flight rewrite equation (3.2.15),

$$t_s(\eta_1) - t_s^0 = -\mu log(d(\eta_1 - \eta_{HC})) + h.o.t. \tag{3.3.5}$$

where μ, d are defined as in equation (3.2.16).

Using equation (3.2.16), the map P in equation (3.2.7) can be written as

$$P^l(\eta_1) \quad = \quad e^{-\epsilon(t_s(\eta_1)-t_s^0)}\eta_1 + \epsilon \int_{t_s^0}^{t_s(\eta_1)} h_\infty(V) e^{\epsilon(t-t_s(\eta_1))} dt \tag{3.3.6}$$

This equation can be further simplified if expressions (3.2.17) and (3.2.18) are used,

$$P^l(\eta_1) \approx (d(\eta_1 - \eta_{HC}))^\sigma (\eta_1 - h_\infty(V_{HC})) + h_\infty(V_{HC}) \tag{3.3.7}$$

From (3.3.7), when $\eta_1 \to \eta_{HC}^+$

$$P^l(\eta_1) \to h_\infty(V_{HC}) \tag{3.3.8}$$

And, from (3.3.6), when η_1 moves towards Σ_1, $t_s(\eta_1) \to t_s^0$ and

$$P^l(\eta_1) \to \eta_0. \tag{3.3.9}$$

Therefore, it can be concluded that the map can be extended continuously from I_{linear} to $I_{nonlinear}$ for all $\eta \in (\eta_{HC}, \eta_R)$.

3.3.3 Constant region I_{const} for $\eta < \eta_{HC}$

In this case, all trajectories of the fast subsystem (except the unstable fixed points) converge to a unique attracting equilibrium $(V^*(h), n^*(h), s^*(h))$ for some h. The following equations to obtain $n^*(h)$, $s^*(h)$ and $V^*(h)$ have to be satisfied simultaneously

$$\begin{cases} n^* = n_\infty(V*) \\ s^* = \frac{s_\infty(V^*)}{1-s_\infty(V^*)} \\ 0 = I_{NaP}(V^*) + I_{Na}(V^*) + I_K(V^*) + I_L(V^*) + I_{g_{ton}}(V^*) + I_{g_{syn}}(V^*). \end{cases}$$

The above combined with (2.3.2) gives us

$$\frac{dh}{dt} = \epsilon(h_\infty(V^*) - h) \tag{3.3.10}$$

One can show that $\Phi^*(h) = (V^*(h), n^*(h), s^*(h))$ evolves near the stable branch of the fixed points parameterized by h, as h slowly increases according to (3.3.10) until it reaches $h = h_{SN}$. Therefore, for $h = \eta$ define $P(\eta)$ for $\eta < \eta_{HC}$ by

$$P(\eta) = \eta_{SN} \tag{3.3.11}$$

As an important remark, notice that if the curve of periodic orbits does not end in a homoclinic point, that is, it ends in a saddle node of periodics SN^p, then some of the analysis carried out for the map on this section will not be valid. This is true, since at SN^p, before the periodic orbits go unstable, the period of these orbits is finite, i.e., $\exists\ M \in \Re$ such that $t_s(\eta^*) < M$ for all η^*. Therefore, the period of the oscillations varies relatively little with small changes in η. Note also that this transition between HP to SN^p is a continuous process, that is, with increasing g_{syn}, the periodic orbits with high period gradually become unstable with increasing g_{syn}. Therefore, for some values of g_{syn} we have a SN^p but the period is still large but finite. Therefore, there exists the $I_{nonlinear}$ but the rate of change of F with η does not go to infinity. So for some values of g_{syn} the curve of periodics end in a SN^p and the period is small then, our 3 regions above reduce to only 2: I_{linear} and I_{const}. In the I_{linear}, replace η_0 by η_{SN^p} and the rest of the analysis carries over. In I_{const}, replace η_{HC} by η_{SN^p}, so that, you get again $P(\eta) = \eta_{SN}$.

3.3.4 Properties of $P(\eta)$

After the above analysis one can summarize some of the properties of our map. For a fixed g_{syn}, if there exists an η_* such that

$$F(\eta_*) \geq \eta_* \tag{3.3.12}$$

then there exists a fixed point, $\bar{\eta}(g_{syn})$, of the map $P(\eta)$. If $\bar{\eta}(g_{syn})$ exists, then it must satisfy the following relation:

$$P(\bar{\eta}(g_{syn})) = \bar{\eta}(g_{syn}) \quad \Leftrightarrow \quad F(\bar{\eta}(g_{syn})) = \bar{\eta}(g_{syn}). \tag{3.3.13}$$

Once existence is established, uniqueness of $\bar{\eta}(g_{syn})$ comes as a consequence of the properties of $F(\eta)$ discussed above, where it is observed numerically that $F(\eta)$ is a monotone decreasing function of η, for all $\eta < \eta_{HC}$ or $\eta < \eta_{SN^p}$, as appropriate.

Stability of the fixed point is obtained by computing the derivative of P with respect to η at the fixed point and checking whether this derivate is smaller than 1, in absolute value. In other words, it is required for stability that $\left|\frac{d\bar{P}}{d\eta}\right| < 1$ where the bar on top of P represents its evaluation at the fixed point [27].

Suppose we are in the regime where HP exists. Differentiating equation (3.2.9) with respect to η gives

$$\frac{dP}{d\eta} = e^{-\epsilon t_s(\eta)} + \frac{dF}{d\eta}\left(1 - e^{-\epsilon t_s(\eta)}\right) + e^{-\epsilon t_s(\eta)}\epsilon\frac{dt_s(\eta)}{d\eta}(F(\eta) - \eta). \tag{3.3.14}$$

At $\bar{\eta}$, the last term in (3.3.14) vanishes and then,

$$\frac{d\bar{P}}{d\eta} = e^{-\epsilon \bar{t}_s} + \frac{d\bar{F}}{d\eta}\left(1 - e^{-\epsilon \bar{t}_s}\right). \tag{3.3.15}$$

At $\eta \to \eta_{HC}^+$, all of the following take place:

1. $t_s(\eta) \to \infty$;
2. $\frac{dF}{d\eta} \to -\infty$;
3. $e^{-\epsilon t_s(\eta)}\frac{dt_s(\eta)}{d\eta} = -e^{-\epsilon t_s(\eta)}\left(\frac{\sigma}{\eta - \eta_{HC}}\right) \to 0$.

The last property is true, since the exponential function goes much faster to zero than the rational function goes to infinity. Therefore, $\frac{dP}{d\eta} \to -\infty$ as $\eta \to \eta_{HC}^{+}$.

Some additional properties of $P(\eta)$ are summarized below, which hold when HP is present:

1. $P(\eta) \to h_{\infty}(V_{HC})$ as $\eta \to \eta_{HC}^{+}$, since, in equation (3.2.9), $e^{-\epsilon t_s(\eta)} \to 0$ and $F(\eta) \to h_{\infty}(V_{HC})$ as $\eta \to \eta_{HC}^{+}$;
2. $0 < \dfrac{dP}{d\eta} < 1$ and $P(\eta) < \eta$ both hold, sufficiently far from η_{HC} (see equation (3.3.4));
3. $\dfrac{dP}{d\eta} < 0$ near $\eta = \eta_{HC}$;

Property 3 holds true assuming that inequality (3.3.12) is satisfied and using proposition 3.2.2 and the fact that $\frac{dt_s}{d\eta} < 0$ near HP. If the branch of periodic orbits doesn't end in a homoclinic, the condition that $\dfrac{dP}{d\eta} < 0$ may not hold and this derivative may not change signs at all. In figure 12, an example is shown for which a curve of periodics does not end on a HP. At the SN^{p}, for this example, the period of the stable periodic orbits vary from approximately from 0.70 to 1.816. In the right panel, the top part of the figure represents the stable branch of the curve of periodics whereas the bottom branch represents the unstable branch. The fact that the period does not change much on the stable branch could also be seen in a frequency versus h plot (figure not shown).

According to our analysis, the loss of stability of $\bar{\eta}(g_{syn})$ takes place only through,

$$\frac{d\bar{P}}{d\eta} = -1 \Leftrightarrow \frac{d\bar{F}}{d\eta} = \frac{-1 - e^{-\epsilon \bar{t}_s}}{(1 - e^{-\epsilon \bar{t}_s})} \tag{3.3.16}$$

where the value of the derivative of F with respect to η is negative for any value of $\bar{\eta}$.

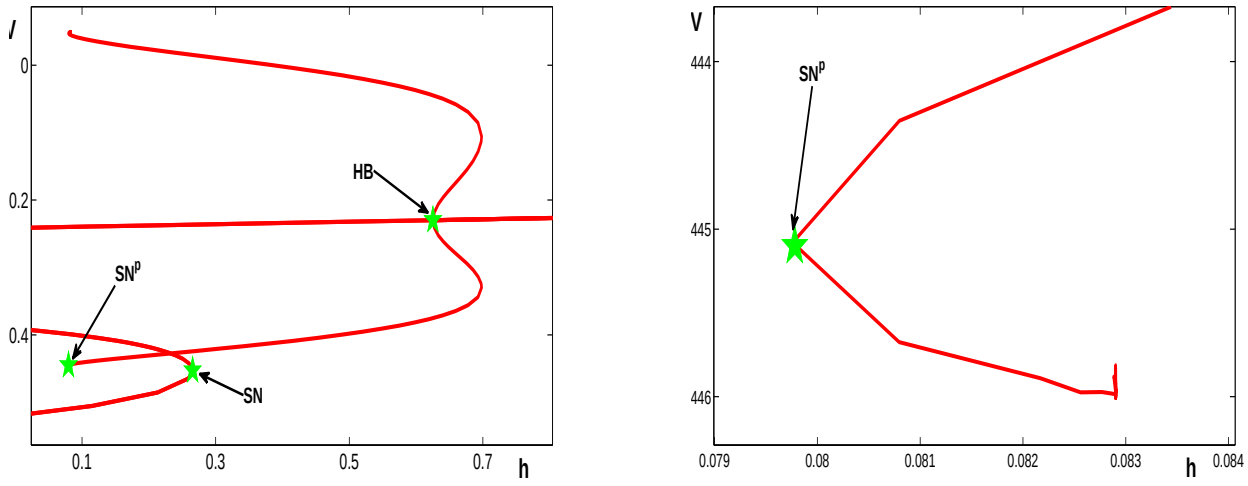

Figure 12: Bifurcation diagram for $g_{syn} = 0.47$ and $g_{ton} = 0.025$ showing that for these parameter value we do not end in a homoclinic point as it can be clearly seen in the zoomed plot on the right panel. In the right panel, the top branch is stable and the bottom branch is unstable. The period at SN^p is approximately 1.816.

3.4 SPIKING VS BURSTING

In this section, conditions for the transition between bursting and spiking will be stated and some numerical results will show the accuracy of such conditions. The conditions derived here will hold true for small values of g_{syn}, since we observe numerically that for sufficiently large g_{syn}, the curve of periodics does not necessarily end in a homoclinic point (see figure 12).

Recall that a unique fixed point exists provided that

$$F(\eta_*) \geq \eta_* \qquad \text{for some} \quad \eta_* \in (\eta_{HC}, \eta_R) \tag{3.4.1}$$

Suppose that for some given (small) value of g_{syn}, the cell exhibits tonic spiking. Recall that, as shown earlier, the derivative of $P(\eta, g_{syn})$ with respect to η goes from positive to

negative if η is decreased toward η_{HC}. Then, by the Intermediate Value Theorem [34], there exists $\eta = \eta^*(g_{syn}) \in (\eta_{HC}, \eta_R)$ such that

$$\frac{dP}{d\eta}(\eta^*(g_{syn}), g_{syn}) = 0 \tag{3.4.2}$$

The transition to bursting will occur if there exists a g^*_{syn} such that the map $P(\eta, g_{syn})$ falls below η_{HC}, that is,

$$P(\eta^*(g^*_{syn})) < \eta_{HC} \tag{3.4.3}$$

for some $\eta^* \in (\eta_{HC}, \eta_R)$.

Finally, we are guaranteed to cross the line given by (3.4.3) if

$$\frac{dP}{dg_{syn}}(\eta^*(g^*_{syn}), g^*_{syn}) \neq 0 \tag{3.4.4}$$

We can summarize all this in the following result:

Proposition 3.4.1. *Suppose that for some small $g_{syn} \geq 0$ the cell is spiking. Then, the onset of bursting occurs, as g_{syn} increases through g^*_{syn}, if the following conditions hold. For each $g_{syn} \in (g^*_{syn} - \xi, g^*_{syn} + \xi)$ and $0 < \xi \ll 1$, there exists $\eta^(g_{syn}) \in (\eta_{HC}, \eta_R)$ such that*

1. $\frac{dP}{d\eta}(\eta^*(g_{syn}), g_{syn}) = 0$;
2. $P(\eta^*(g^*_{syn})) = \eta_{HC}$, ;
3. $\frac{dP}{dg_{syn}}(\eta^*(g^*_{syn}), g^*_{syn}) < 0$.

The conditions on proposition 3.4.1 are also sufficient for the onset of bursting because if the fixed point of the map is unstable, then bursting exists on some interval $[g^*_{syn}, g^*_{syn} + \Delta]$ for some $\Delta > 0$ and increasing g_{syn}. This makes sense due to continuity of the map with respect to the parameters.

Analysis and numerical results suggest that, for increasing g_{syn}, if the map has a fixed point before the transition from spiking to bursting occurs, then it will persist after the transition as long as the fixed point is not at $\eta^*(g^*_{syn})$. But, this cannot happen since $\eta^*(g^*_{syn}) > \eta_{HC}$ and $P(\eta^*(g^*_{syn})) = \eta_{HC}$ imply that $\eta^*(g^*_{syn}) > P(\eta^*(g^*_{syn}))$.

Considering all analysis above, $P(\eta)$ can be described by one of the 4 situations depicted in figure 13 when the cell is either bursting or spiking.

The top cartoons represent the case when the cell is either bursting or spiking and the curve of periodics ends in a homoclinic point. The cartoons at the bottom also represent bursting and spiking but, this time, when the curve of periodics ends in a saddle node of periodics, with some pretty small period that P remains monotone increasing. Let S_{HC}, B_{HC}, B_{SN^p} and S_{SN^p} denote, in figure 13, spiking with HP, bursting with HP, bursting with SN^p and spiking with SN^p, respectively. For a fixed g_{ton} and increasing g_{syn}, the transition from one of these regimes to another occurs :

$$S_{HC} \to B_{HC} \to B_{SN^p} \to S_{SN^p}$$

The transition S_{HC} to B_{HC} occurs because increasing g_{syn} moves the values for which our cells are active to lower values of η and this brings the map P below η_{HC}, that is $P(\eta^*, g^*_{syn}) < \eta_{HC}$. Continuing to increase g_{syn} makes the periodic orbits with higher periods unstable, that is, we lose HP and gain SN^p and, in this case, $\frac{dP}{d\eta}$ may not change signs at all. At this point we went from B_{HC} to B_{SN^p}, since the map P also goes below η_{SN^p} for some values of η. Finally, increasing g_{syn} even further the map P moves above the line $P = \eta_{SN^p}$ for all η and, at this point cells are spiking again. Transition directly from S_{HC} to S_{SN^p} is also possible since with increasing g_{syn} the map stays above the line $P = \eta_{SN^p}$ but loses HP. The transition between B_{HC} to B_{SN^p} is possible to since the map stays below the identity line and loses HP.

There are 2 transitions that cannot happen without the cell passing through some intermediate transition: $B_{HC} \to S_{SN^p}$ and $S_{HC} \to B_{SN^p}$. The transition $B_{HC} \to S_{SN^p}$ is not possible due to the fact that it would have to happen in a nongeneric point for which

$$\lim_{\eta \to \eta^+_{HC}} P(\eta) = \eta_{HC} \quad \text{and} \quad \frac{dP}{d\eta} > 0 \ \ \forall \eta > \eta_{HC}. \tag{3.4.5}$$

This is equivalent to lose HP and to move below the line $P = \eta_{HC}$ at the same time. Similar explanation holds true for why the transition from S_{HC} to B_{SN^p} cannot occur. The condition of existence of a HP and SN^p used here to help characterize the different regimes, was not used in [5] to distinguish between different regimes.

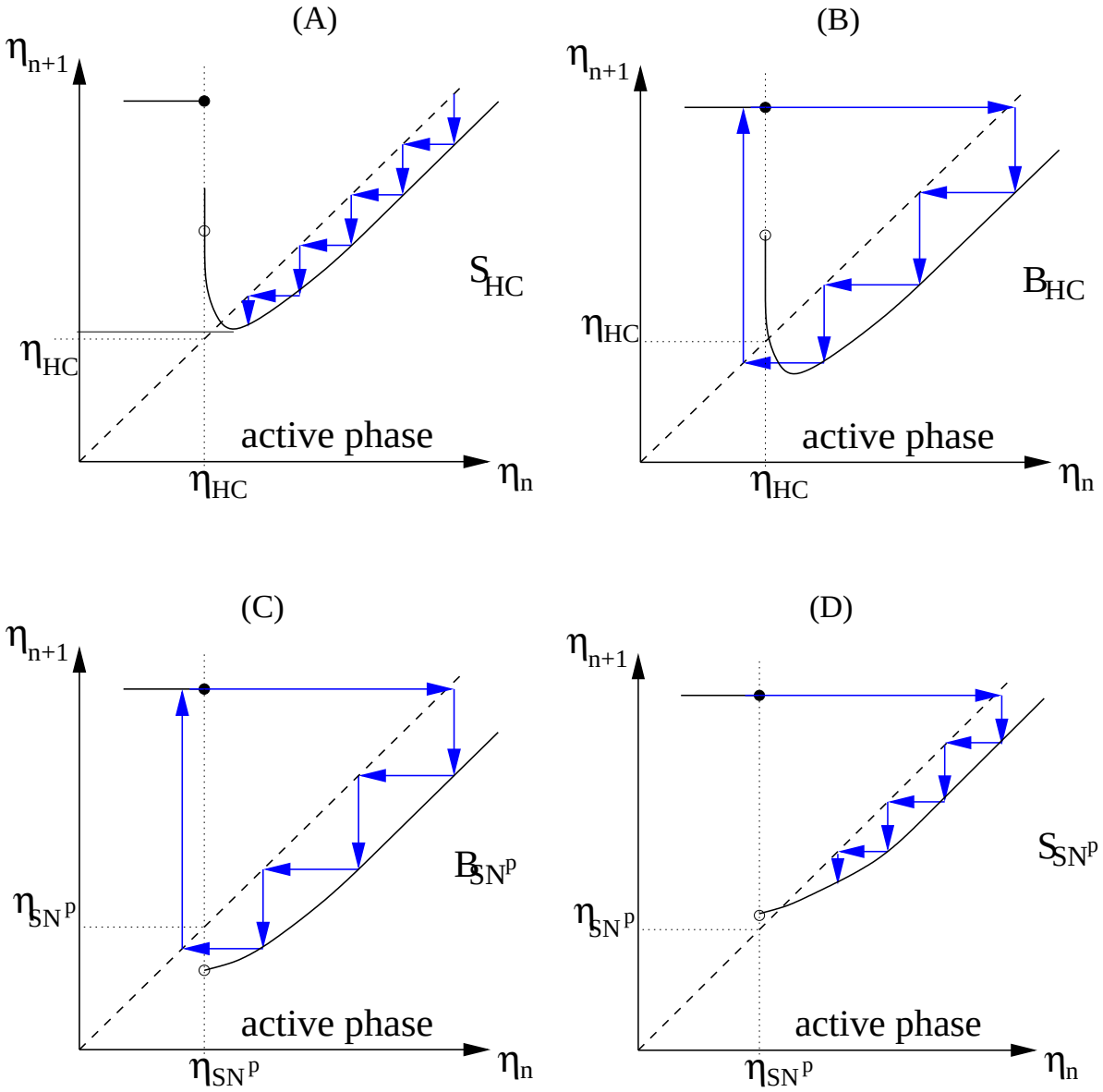

Figure 13: Cartoon showing the four possible forms of the map and related regimes by varying g_{syn} with a fixed g_{ton}. Here, S_{HC}, B_{HC}, S_{SN^p} and B_{SN^p} represent, respectively, spiking with HP, bursting with HP, spiking with SN^p and bursting with SN^p.

3.5 SOME NUMERICAL RESULTS

All numerical results shown in this section and throughout this thesis were obtained using a combination of the XPPAUT [14] and MATLAB [35].

In figure 14, some numerical results for $g_{ton} = 0.025$ and $g_{syn} = 0.10, 0.11, 0.47, 0.48$ determining with some accuracy the transition from spiking (S_{HC}) to bursting (B_{HC})(top) and the transition from bursting (B_{SN^P}) to spiking (S_{SN^P}) (bottom). Note that, the conditions for the onset of bursting for small g_{syn} are satisfied.

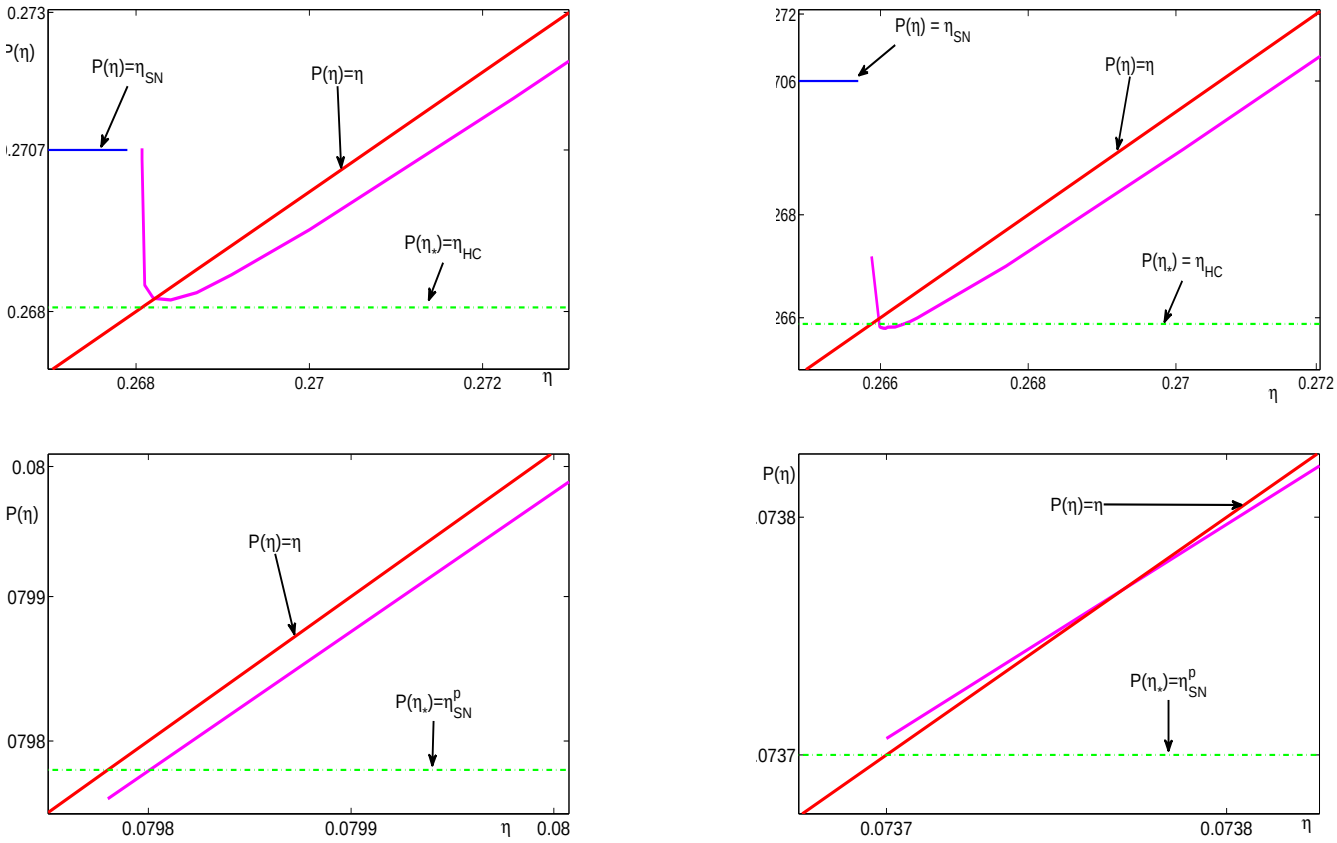

Figure 14: $P(\eta)$ for $g_{ton} = 0.025$ (equivalent to $g_{ton} = 0.70$ on the original system), for a single self-coupled cell. At the top, transition from S_{HC} ($g_{syn} = 0.10$) (left) to B_{HC} ($g_{syn} = 0.11$)(right). At the bottom, transition from B_{SN^P} ($g_{syn} = 0.47$) (left) to S_{SN^P} ($g_{syn} = 0.48$) (right). Note that our Proposition 3.2.2 only covers the transition at the top.

In figure 15, the dynamics of the full system (2.3.1)-(2.3.4)for each one of the cases in figure 14 is shown illustrating that for each of the values of g_{syn} the map predicts the behavior of the full system. Let's observe some differences between the different solutions obtained in figure 15. For the 2 bursting solutions (top right and bottom left), it can be seen that the duration of the burst and frequency are quite different. This is due to the fact that for $g_{syn} = 0.11$ (upper right) we have a fixed point close to the homoclinic and this implies that it is needed a long excursion to get back to the starting point given that the period is growing fast near the homoclinic. In the bottom left panel, there is not a fixed point and the curve of periodics end in SN^p. This means that it take less time to move around the orbit. Similar explanation can be given for the difference between figure on top left and bottom right. Finally, table 3 shows the values η_{HC} and the minimum value of the map for the cases in figure 14. As expected, these values are very close to each other, but they are consistent with the solutions for the full system.

In figure 16, cobwebbing the maps for $g_{syn} = 0.1$ and $g_{syn} = 0.11$ shows the dynamics of the spiking and bursting solutions, respectively, that they represent. For the tonic spiking solution, starting at η_0 one obtains the next point by reflecting the point to the identity line horizontally and to obtain the next point on the iteration just reflect it vertically until you intersect the graph of P. Doing this procedure over and over again gives you the iterated map and the dynamics of the solution over time.

g_{syn}	η_{HC}	$P(\eta_{min})$
0.10	0.2680692	0.26819
0.11	0.26588065	0.26579
0.47	0.07978	0.07976
0.48	0.07368	0.073686

Table 3: Values of η_{HC} computed with AUTO [14] and the lowest value of $P(\eta)$ indicating whether a transition to a different regime occurred.

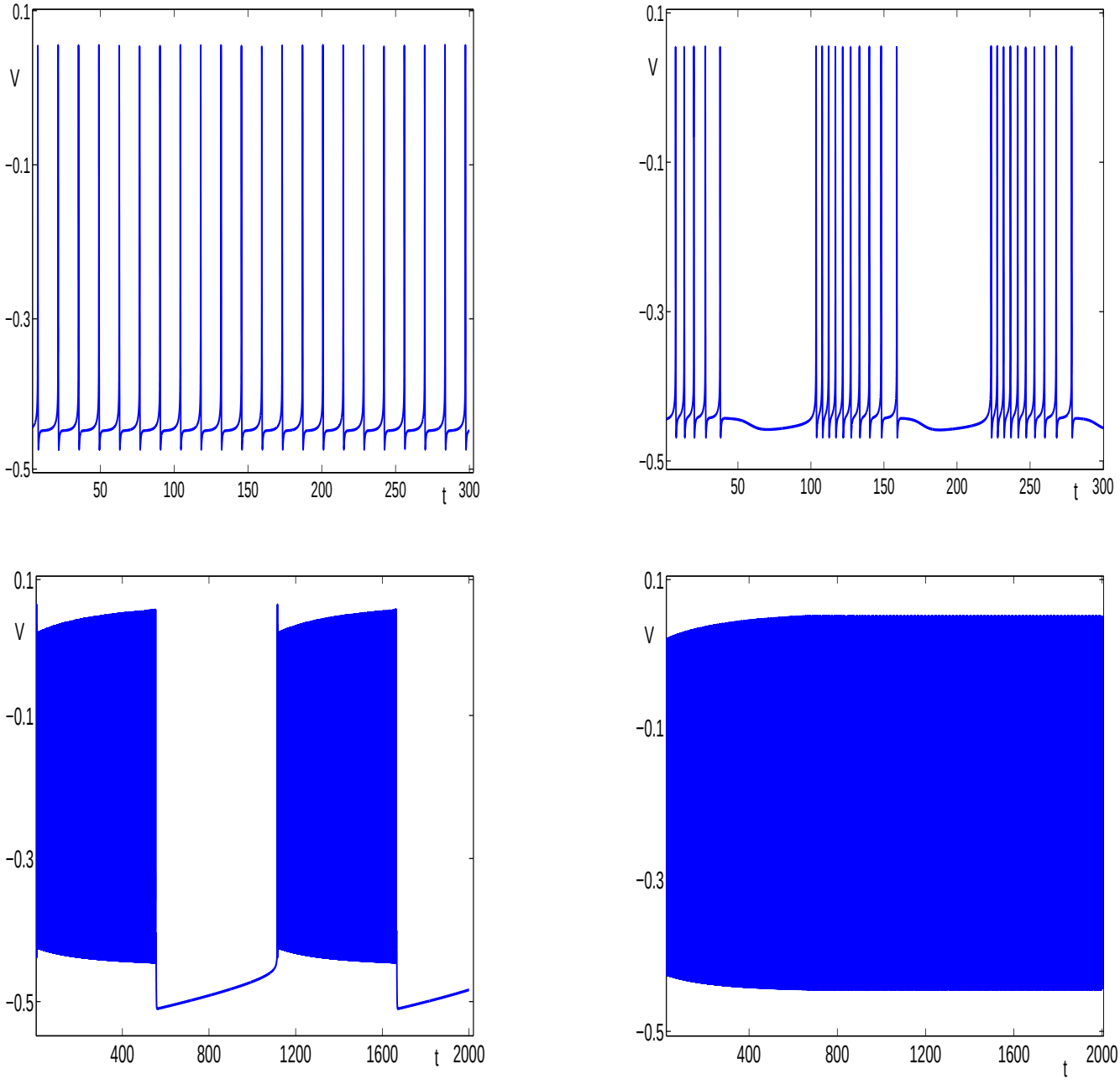

Figure 15: Full system for all 4 maps plotted in figure 14 showing that the transition from spiking to bursting and bursting to spiking occurred as the map predicted

.

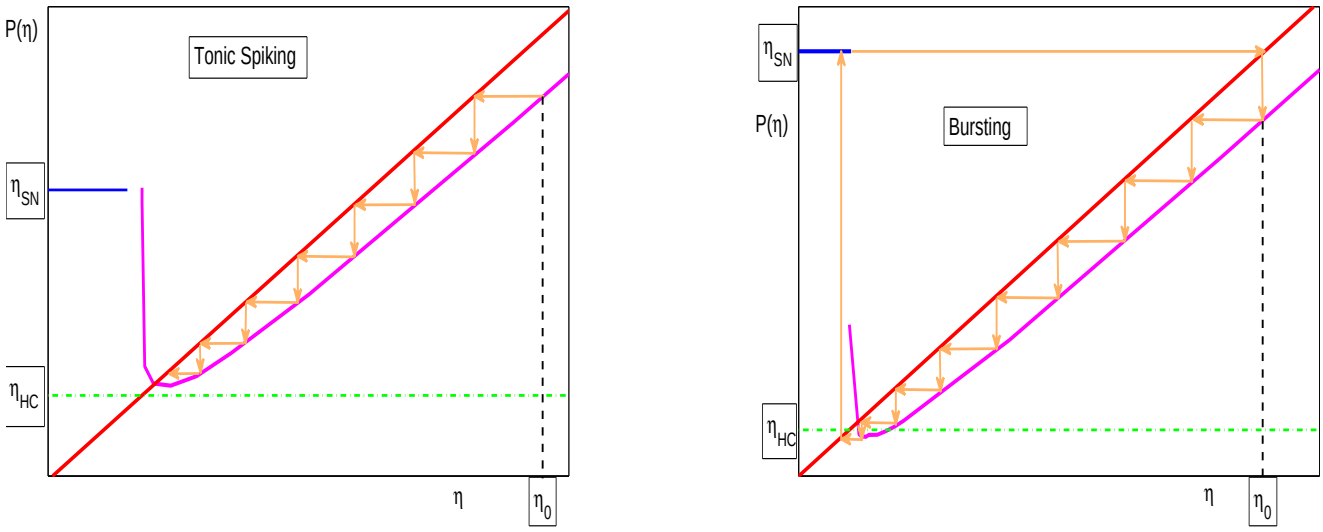

Figure 16: Cobwebing of the maps on figure 14 for $g_{ton} = 0.025$ (equivalent to $g_{ton} = 0.70$ on the original system), for a single self-coupled cell and $g_{syn} = 0.1$ and $g_{syn} = 0.11$. These results match with what is seen for the transition from spiking to bursting for the full system.

For tonic spiking, the cobwebbing gets trapped by the fixed point meaning that the solution will stay there forever, oscillating (due to fast subsystem). For bursting, once the cobwebbing iteration gets close to the minimum value of $P(\eta)$, it escapes from the curve of periodics and moves to the branch of stable fixed points and as soon as it gets to the saddle node point η_{SN}, the cell jumps to the active phase starting the whole process again. This cobwebbing solution was implemented in MATLAB [35].

In summary, we derived, in this chapter, a one dimensional map from a four dimensional system of ordinary differential equations. Using this map, we determined conditions for the transition from bursting to spiking with a continuous increase of g_{syn} and numerically corroborated our predictions. Moreover, we determined what possible forms transitions between bursting and spiking can take in general.

Using a similar approach, we derive, in the next chapter, a two dimensional map for a network of two coupled identical cells and determine conditions for the transition between different regimes, if possible.

4.0 TWO DIMENSIONAL MAP

Sometimes it is not possible to represent all important characteristics of a particular model described as a set of ordinary differential equations using a one dimensional map. Instead, two or higher dimensional maps are required to describe the behavior of the network. Some two dimensional maps are not derived directly from the system, these maps are rather built to fit in to a certain set up to describe novel characteristics of a particular system [50, 51].

In this chapter, system (2.3.1)-(2.3.4) with $i = j = 1, 2$ and $j = 3 - i$, defined in chapter 2 will be reduced to a two dimensional map, building on the same ideas and results from chapter 3. The analysis of the resulting map is expected to be more difficult than for the one dimensional map due to coupling and nonlinearities. Using this two dimensional map, we want to determine, in a compact form, what dynamical regimes are possible and how the transitions between the different regimes, including those found in [5], occur.

4.1 OBTAINING THE MAP

Let $\Phi(T) = (V_1(T), n_1(T), s_1(T), V_2(T), n_2(T), s_2(T))$ be the solution of fast subsystem $\dot{\Phi}(T) = f$ where f is the right hand side of equations (2.3.1), (2.3.3) and (2.3.4) with $i = 1, 2$. Let $\Sigma \subset \Re^6$ be a 5-dimensional cross section such that, the intersection of the V_1 nullsurface and the family of periodic orbits takes place at a point on each orbit where $\dot{V}_1 = 0$. Without loss of generality let's assume that we are at the minimum of V_1, that is, $V_1 = V_1^{min}$ on Σ. Integrate the system (2.3.1)-(2.3.4) starting at a point Φ^0 on Σ at $T = 0$. Define $c = sign(\dot{n}_2(0))$. It was shown in chapter 3 that $\dot{V}_1 = 0$ implies $\dot{n}_1 \neq 0$. Moreover, at

$V_1 = V_1^{min}$, $\dot{n}_1 < 0$. The first return map can be written as

$$\mathbf{P}(\eta_1, \eta_2) = \begin{bmatrix} P_1(\eta_1, \eta_2) \\ P_2(\eta_1, \eta_2) \end{bmatrix} = \begin{bmatrix} h_1(T_s(\eta_1, \eta_2)) \\ h_2(T_s(\eta_1, \eta_2)) \end{bmatrix} \tag{4.1.1}$$

where $T_s(\eta_1, \eta_2)$ is the time of first return to Σ. For simplicity, write $T_s = T_s(\eta_1, \eta_2)$, $P_1 = P_1(\eta_1, \eta_2)$ and $P_2 = P_2(\eta_1, \eta_2)$. The time of flight (return) can be defined as

$$T_s = min\{T > 0 \mid \Phi(T) \in \Sigma \quad and \quad \dot{n}_1 < 0 \quad and \quad sgn(\dot{n}_2(T)) = c\} \tag{4.1.2}$$

Recall that,

$$\begin{cases} \frac{dh_1}{dT} = \epsilon\tau_h(V_1)\left(h_\infty(V_1) - h_1\right) \\ \frac{dh_2}{dT} = \epsilon\tau_h(V_2)\left(h_\infty(V_2) - h_2\right) \end{cases} \tag{4.1.3}$$

Using the same strategy as in chapter 3, the two dimensional first return map can be written as

$$\mathbf{P}(\eta_1, \eta_2) = \begin{bmatrix} P_1 \\ P_2 \end{bmatrix} = \begin{bmatrix} e^{-\alpha_1(T_s)}(\eta_1 - F_1) + F_1 \\ e^{-\alpha_2(T_s)}(\eta_2 - F_2) + F_2 \end{bmatrix} \tag{4.1.4}$$

where $\eta_1 = h_1(0)$ and $\eta_2 = h_2(0)$ and

$$\bar{\tau}_h(V_i) = \frac{1}{T_s}\int_0^{T_s} \tau_h(V_i(\xi))d\xi, \quad \alpha_i(T_s) = \epsilon\bar{\tau}_h(V_i)T_s, \quad g_i(V_1, V_2) = \epsilon h_\infty(V_i)\tau_h(V_i) \tag{4.1.5}$$

$$F_i = F_i(\eta_1, \eta_2) = \frac{\int_0^{T_s} g_i(V_1, V_2)e^{\alpha_i(T)}dT}{e^{\alpha_i(T_s)} - 1} \tag{4.1.6}$$

for $i = 1, 2$. Each of the components $P_i(\eta_i, \eta_j)$ of the map $\mathbf{P} = \mathbf{P}(\eta_1, \eta_2)$ has a similar structure as the one dimensional map derived in chapter 3 if η_j is fixed, but due to coupling the analysis of the two dimensional map derived here is harder than for the one dimensional case. In terms of the dynamics, coupling between the 2 cells, although it is not explicit in the expressions, will affect the behavior of each component of the map. The functions $F_i = F_i(\eta_1, \eta_2)$ for $i = 1, 2$ can also be written in a somewhat simplified form, if we are in the neighbohood of a homoclinic point for the the 2-cell system, as

$$F_i \approx \frac{(F_i^0 - h_\infty(V_{HC}^i))(e^{\alpha_i(T_s^0)} - 1)}{e^{\alpha_i(T_s)} - 1} + h_\infty(V_{HC}^i)$$

where T_s^0 is the first return time to the section Σ, for some fixed η in a region where the rate of change of period of the oscillations with respect to η_1 and η_2 is approximately constant, V_{HC}^i is the value of V_1 and V_2 evaluated at the homoclinic point and $F_i^0 = F_i^0(\eta_1, \eta_2)$ is defined as

$$F_i^0 = \frac{\int_0^{T_s^0} g_i(V_1, V_2) e^{\alpha_i(T)} dT}{e^{\alpha_i(T_s^0)} - 1}. \tag{4.1.7}$$

If there is no homoclinic point for the system, then F_i, for $i = 1, 2$ will be used as in equation (4.1.6). In the formulas for P_1 and P_2, τ_h was averaged over one oscillation for each fixed pair (η_1, η_2), for convenience of notation and in order to simplify the analysis of the map.

Before we start the analysis of the map, let's take a look at a numerical example, using equation (4.1.4) for some fixed values of the parameters.

4.2 A NUMERICAL EXAMPLE

Let's use the formula obtained for the map $\mathbf{P}$ in equation (4.1.4) and numerically determine P_1 and P_2 for $g_{syn} = 0.107143$ and $g_{ton} = 0.0275$ with all other parameters fixed, as in table 2. For these values of the parameters the two cells are bursting. Figure 17 shows trajectories of the full system on the (h_1, h_2)-plane and how the slow variables (h_1, h_2) vary on each burst after a long enough transient has passed for a given set of initial conditions. Now, let $\eta_1 = h_1$ and $\eta_2 = h_2$. Then , according to figure 17, since the position of η_1 will strongly depend on the position of η_2 (and vice-versa), then we can imagine that the components P_1 and P_2 will also strongly depend on the position of both η_1 and η_2. In this case, both η_1 and η_2 are varying whereas on the one dimensional map P only one control parameter was varying.

In order to determine the form of P_1 and P_2, let's do the following. Pick a point (η_1, η_2) on the trajectory of the full system (2.3.1)-(2.3.4), say $(\eta_1^1, \eta_2^1) \simeq (0.2045, 0.2095)$ (see figure 18(A)). Compute $P_1(\eta_1^1, \eta_2^1)$ and $P_2(\eta_1^1, \eta_2^1)$ using (4.1.4). On the (η_1, P_1) and (η_2, P_2) planes plot the points $(\eta_1^1, P_1(\eta_1^1, \eta_2^1))$ and $(\eta_2^1, P_2(\eta_1^1, \eta_2^1))$, respectively.

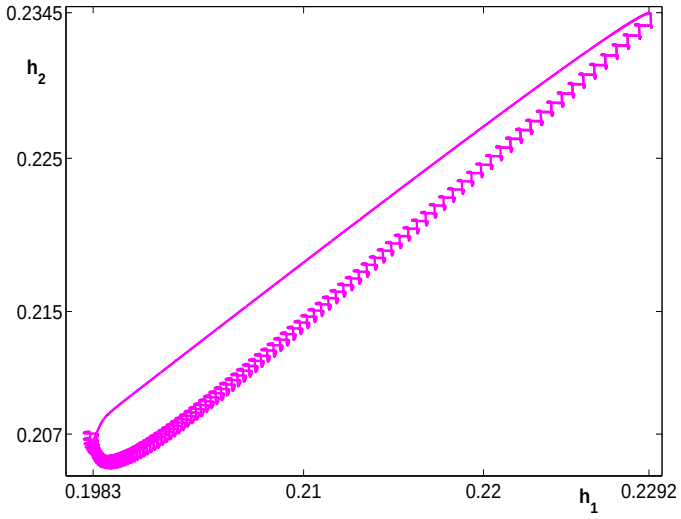

Figure 17: Trajectories of the full system (2.3.1)-(2.3.4) for a bursting solution for $g_{syn} = 0.107143$ and $g_{ton} = 0.0275$ on the (h_1, h_2)-plane. This trajectories were obtained after eliminating a transient of approximately 8s and the next $500ms$ of the simulation were plotted.

Cobweb P_1 and P_2 at the same time. That is, on the (η_1, P_1)-plane plot a horizontal line parallel to the η_1 axis from $(\eta_1^1, P_1(\eta_1^1, \eta_2^1))$ to $(P_1(\eta_1^1, \eta_2^1), P_1(\eta_1^1, \eta_2^1))$. Similarly, on the (η_2, P_2)-plane plot a horizontal line parallel to the η_2 axis from $(\eta_2^1, P_2(\eta_1^1, \eta_2^1))$ to $(P_2(\eta_1^1, \eta_2^1), P_2(\eta_1^1, \eta_2^1))$. At this time, we moved from point (η_1^1, η_2^1) to the point $(\eta_1^2, \eta_2^2) \simeq (0.2042, 0.2092)$. Repeat same procedure as for (η_1^1, η_2^1) to find $P_1(\eta_1^2, \eta_2^2)$ and $P_2(\eta_1^2, \eta_2^2)$. Note that the values of P_1 and P_2 on the second iterate depend on the values of P_1 and P_2 on the first iterate.

Repeating this procedure over and over again, we found numerically P_1 and P_2 for the pairs (η_1^3, η_2^3), (η_1^4, η_2^4), $\ldots$, $(\eta_1^{25}, \eta_2^{25})$, $(\eta_1^{26}, \eta_2^{26})$, $\ldots$, $(\eta_1^{34}, \eta_2^{34})$ using equation (4.1.4). At $(\eta_1^{34}, \eta_2^{34})$ the two cells fall to the curve of steady states S and η_1 and η_2 start increasing until they reach SN where they jump back to the active phase. From iteration 1 to 25, both, η_1 and η_2 are decreasing monotonically. But, at iteration 26, we have that $(\eta_2^{26}, P_2(\eta_1^{26}, \eta_2^{26}))$ is above the identity line as opposed to $(\eta_2^{25}, P_2(\eta_1^{25}, \eta_2^{25}))$(figure 19(C)).

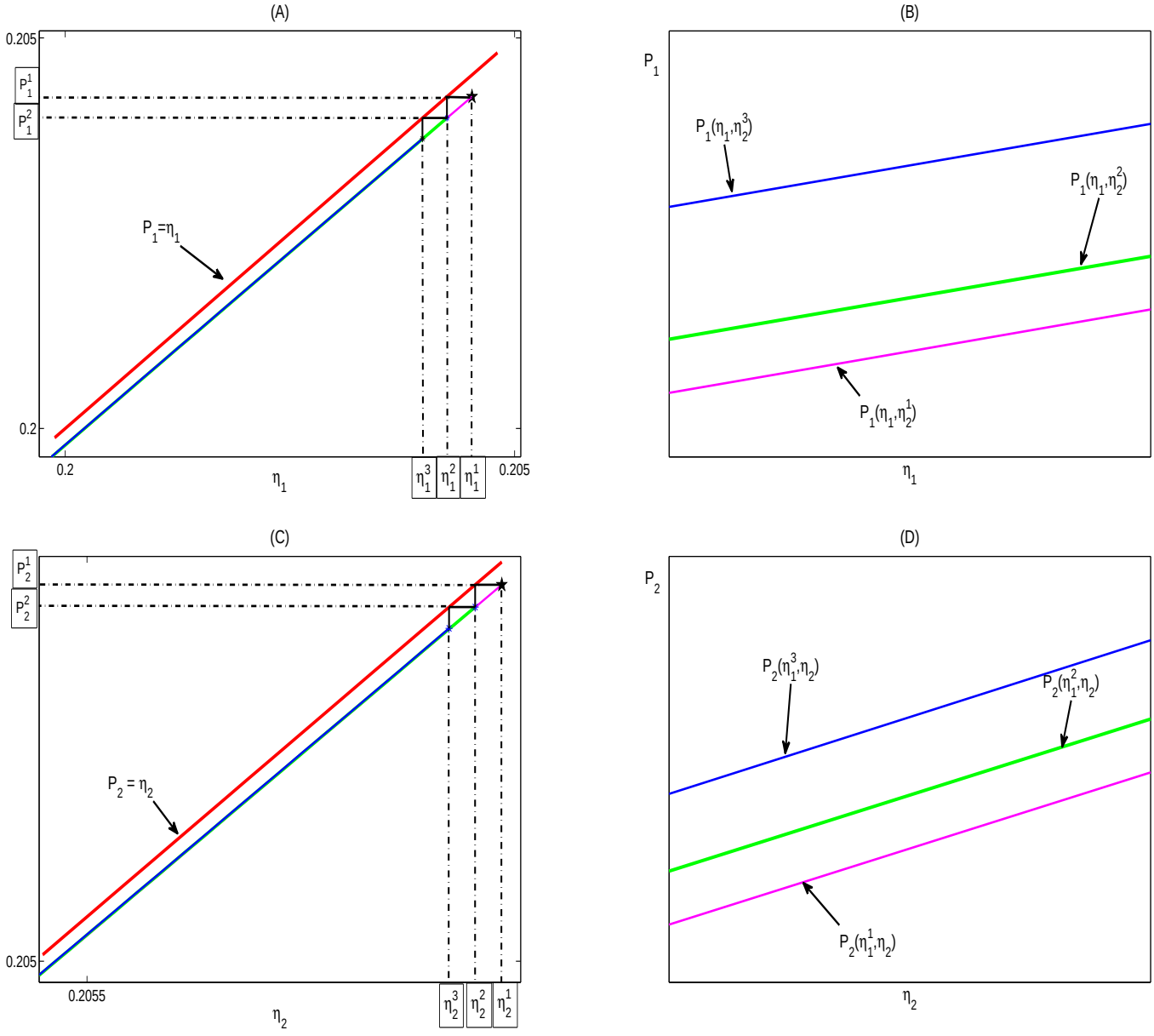

Figure 18: First two approximations of P_1 and P_2, computed using equations (4.1.4). Parts (B) and (D) show a zoom in a very small neighborhood near the computed maps from figures (A) and (C), respectively. These zooms show that decreasing either η_1 or η_2 the corresponding map moves upward.

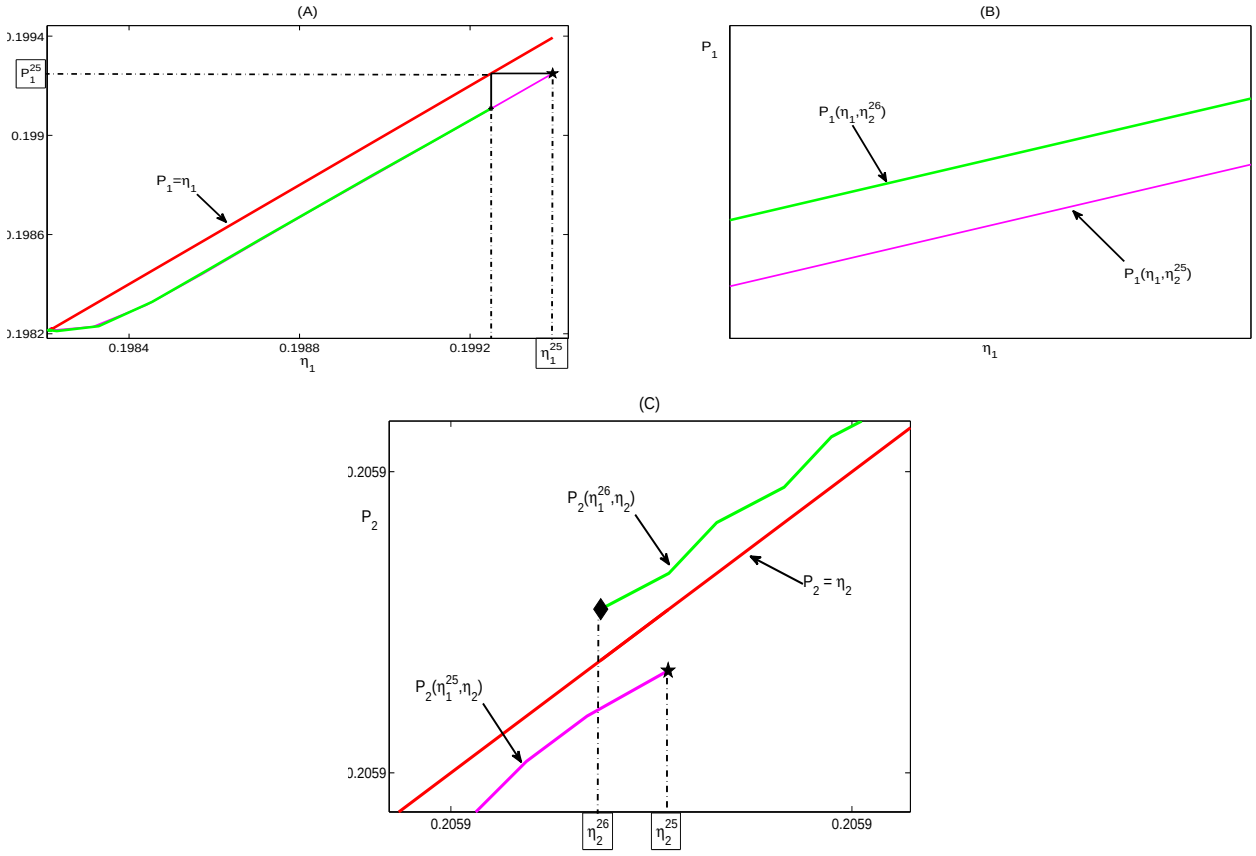

Figure 19: (A)-(B) Curves $P_1(\eta_1, \eta_2^{25})$ and $P_1(\eta_1, \eta_2^{26})$ are still below the identity line. (C) Curves $P_2(\eta_1^{25}, \eta_2)$ and $P_2(\eta_1^{26}, \eta_2)$ showing that $P_2(\eta_1^{26}, \eta_2)$ is now above the identity line and the next iteration of the map has to move to larger values of η_2.

This means that the following iterations of P_2 will have to be performed upward as opposed to what we were doing so far. As for P_1, it remains below the identity line for all iterates. (see figure 19(A)-(B)). Before we go any further let's note a few things.

If we fix $\eta_1 = \eta_1^1$ then $P_2(\eta_1^1, \eta_2)$ is a one dimensional map in η_2. By continuity of the parameters involved on the system of differential equations, the graph of $P_2(\eta_1^1, \eta_2)$ passes through $(\eta_2^1, P_2(\eta_1^1, \eta_2^1))$. Similarly, for fixed $\eta_2 = \eta_2^1$ plot $P_1(\eta_1, \eta_2^1)$ for variable η_1 passing through $(\eta_1^1, P_1(\eta_1^1, \eta_2^1))$. In general, for fixed $\eta_i = \eta_i^j$ for $i = 1, 2$, we plotted the curves (one dimensional maps) $P_1(\eta_1, \eta_2^j)$ and $P_2(\eta_1^j, \eta_2)$ for $j \in \{1, 2, \ldots, 34\}$.

In figure 18(D), note that $P_2(\eta_1^2, \eta_2)$ is slightly shifted upward with respect to $P_2(\eta_1^1, \eta_2)$.

Also, figure in 18(B) $P_1(\eta_1, \eta_2^2)$ is also slightly shifted upward with respect to $P_1(\eta_1, \eta_2^2)$. So, the first two iterates (points) of the maps P_1 and P_2 belong to two different curves. In this numerical example, for each $j \in \{1, 2, \ldots, 34\}$ the curve $P_1(\eta_1, \eta_2^{j+1})$ was shifted upward with respect to $P_1(\eta_1, \eta_2^j)$ for fixed η_2 for $j \leq 25$. For $j > 25$, the curve of P_1 moves downward due to the fact that at this point η_2 started increasing. The curve $P_2(\eta_1^{j+1}, \eta_2)$ was shifted upward with respect to $P_2(\eta_1^j, \eta_2)$ for fixed η_1 for all j.

Let's look at $P_2(\eta_1^1, \eta_2)$ and $P_2(\eta_1^2, \eta_2)$ on the (η_2, P_2) plane. Since $P_2(\eta_1^1, \eta_2) < P_2(\eta_1^2, \eta_2)$ for all η_2 and $\eta_1^1 > \eta_1^2$ then, for this particular example, $\frac{dP_2(\eta_1,\eta_2)}{d\eta_1} < 0$. Similarly, $\frac{dP_1(\eta_1,\eta_2)}{d\eta_2} < 0$. In fact, computations of the map show that, for this particular example, $\frac{dP_2(\eta_1,\eta_2)}{d\eta_1} < 0$ for every fixed η_2 and $\frac{dP_1(\eta_1,\eta_2)}{d\eta_2} < 0$ for every fixed η_1.

Back to the sequence of points we got before. Connecting, on the (η_1, P_1) and (η_2, P_2) planes, the values of the maps P_1 and P_2 at each (η_1^j, η_2^j), $j = 1, 2, \ldots, 34$, by using linear interpolation between each two consecutive points, we form two one dimensional maps. The curve obtained by linear interpolating $(\eta_1^i, P_1(\eta_1^i, \eta_2^i))$ and $(\eta_1^{i+1}, P_1(\eta_1^{i+1}, \eta_2^{i+1}))$, $i = 1, 2, \ldots, 33$ will be called the iterated map $\Gamma_1 = \Gamma_1(\eta_1)$. In an analogous way, we obtain the iterated map $\Gamma_2 = \Gamma_2(\eta_2)$. These two maps together form a two dimensional map which will be denoted by $\mathbf{\Gamma}$. We can also define $\Psi_1 = \Psi_1(\eta_1)$ and $\Psi_2 = \Psi_2(\eta_2)$ as the linear interpolation of the points $(\eta_1^i, F_1(\eta_1^i, \eta_2^i))$ with $(\eta_1^{i+1}, F_1(\eta_1^{i+1}, \eta_2^{i+1}))$ and $(\eta_1^i, F_2(\eta_1^i, \eta_2^i))$ with $(\eta_1^{i+1}, F_2(\eta_1^{i+1}, \eta_2^{i+1}))$, $i = 1, 2, \ldots, 34$.

Since in our numerical example it is hard to see the whole iterative procedure, we show in a cartoon figure (figure 20) how this iterated process work throughout the computation of the map and how at the end we obtain one of the components of the iterated map Γ. Note that, although in our numerical example the one dimensional curves computed for fixed values of η_j were linear, for some choices of η_i for some η_j fixed the one dimensional curves could be qualitatively similar, for example, to figure 16.

A plot of the iterated maps Γ_1 and Γ_2 for $g_{syn} = 0.107143$ and $g_{ton} = 0.0275$ generated numerically is shown in figure 21. These maps can vary slightly depending on the initial conditions. In this example, a sufficiently long transient passed before the components of the iterated maps were computed.

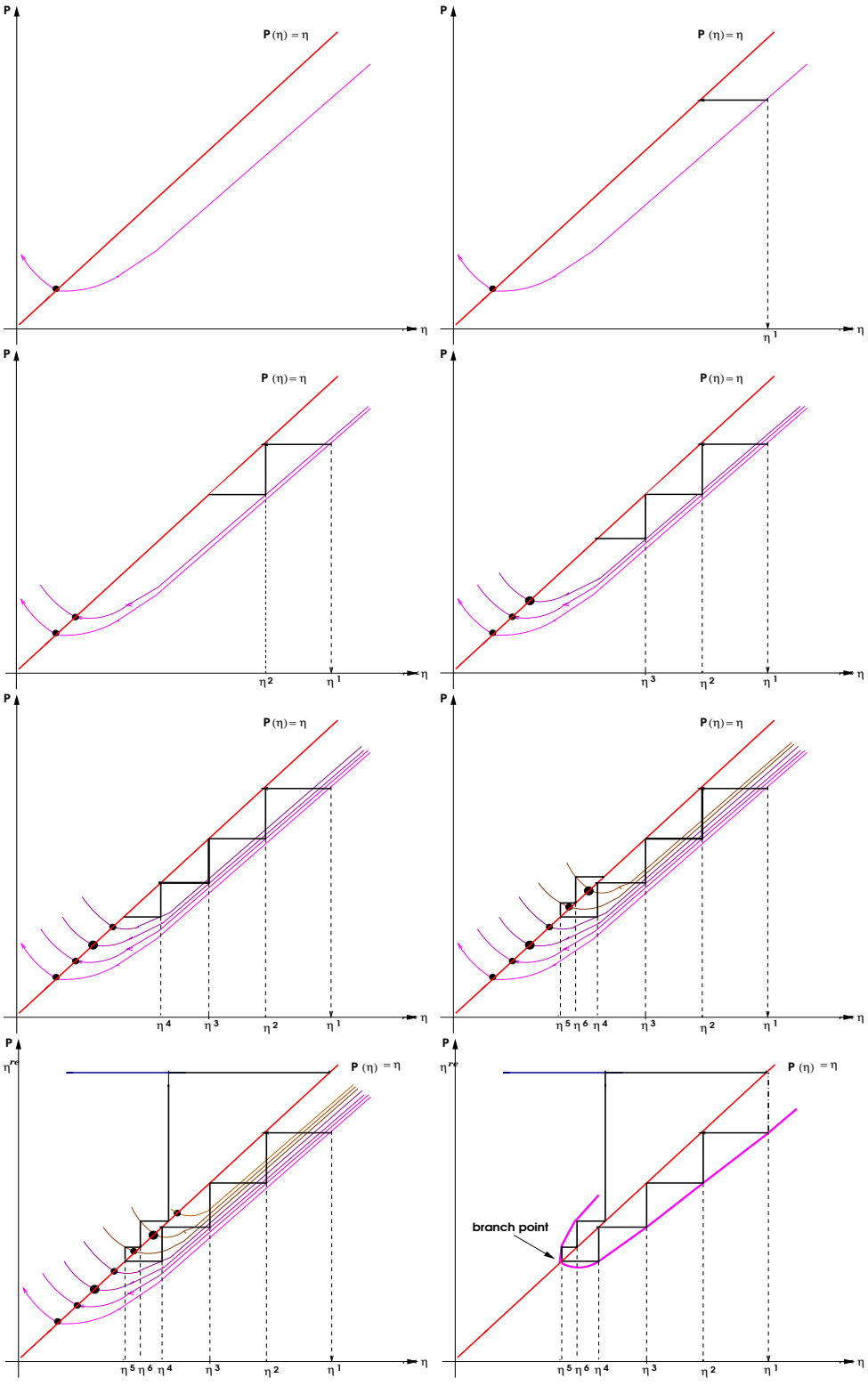

Figure 20: Dynamic cobwebbing to generate an iterated map

In light of these numerical results, let us define lower branch, upper branch, branch point and a true fixed point for the iterated maps Γ_1 and Γ_2.

Definition 4.2.1 (Lower branch, Upper branch)**.** *Suppose, without loss of generality that the iterated map Γ_1, on the (η_1, Γ_1) plane, has a portion of its graph below the identity line and a portion which is above the identity line. Then, we shall refer to the portion of the iterated map below the identity line as the* **lower branch** *of the iterated map and denote it by* **LB** *and, the portion of the map above the identity line as the* **upper branch** *and denote it by* **UB**. *Similar definition holds true for Γ_2.*

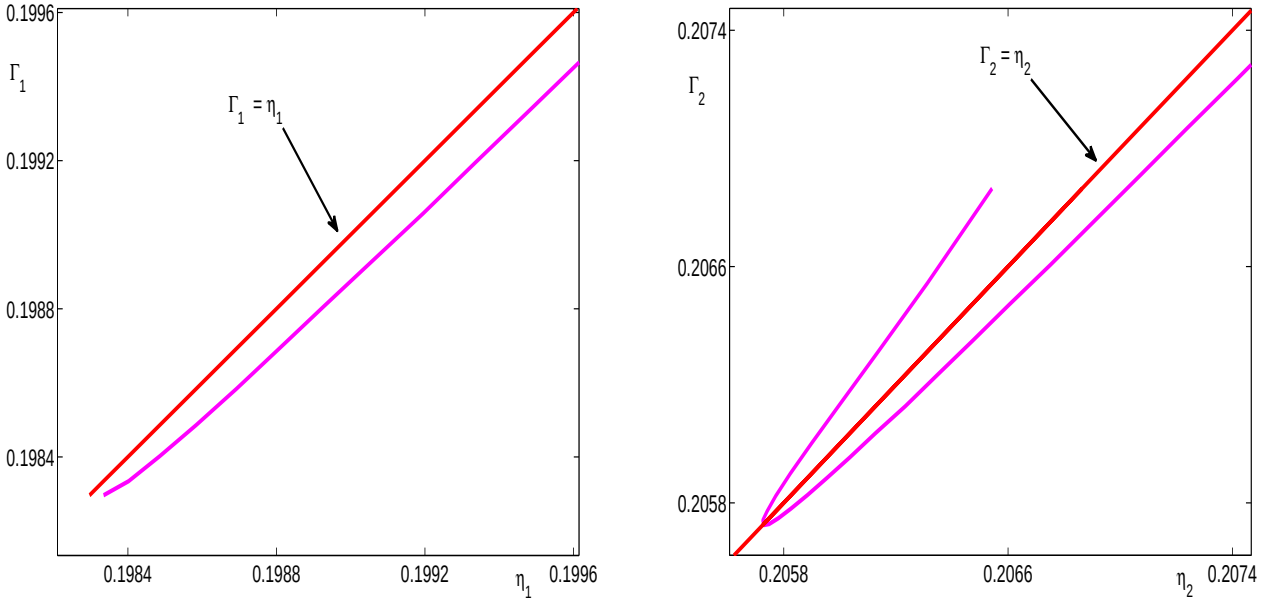

Figure 21: Numerical computation of the iterated maps Γ_1 and Γ_2, for $g_{syn} = 0.107143$ and $g_{ton} = 0.0275$

.

Definition 4.2.2 (branch point, fixed point)**.** *For a fixed set of parameters, a point (η_1^*, η_2^*) is a* **branch point** *of either Γ_1 or Γ_2 if at (η_1^*, η_2^*) either $\Gamma_1 = \eta_1^*$ or $\Gamma_2 = \eta_2^*$, but not both. If at (η_1^*, η_2^*) both $\Gamma_1 = \eta_1^*$ and $\Gamma_2 = \eta_2^*$ hold true, then (η_1^*, η_2^*) will be called a* **fixed point** *of the iterated map* $\mathbf{\Gamma}$.

If a branch point exists, it connects the lower and upper branches of the corresponding iterated map Γ_1 or Γ_2. A fixed point of the iterated map $\mathbf{\Gamma}$ corresponds to a fixed point of the full original system (2.3.1)-(2.3.4).

In figure 22, a cartoon gives a more complete description of other possible shapes that the iterated maps for Γ_1 and Γ_2 can have, besides the 2 depicted in the above numerical example. In this figure, only shown the final iterated maps without the intermediate steps are shown.

As mentioned before, the cobwebbing process is finished either when a stable fixed point is reached (in case the cells are spiking , figure 22(C)-(E)) or until it exits the oscillatory region (in case the cells are bursting, figure 22(A)-(B)).

In the cartoons corresponding to bursting solution there is a reinjection point η^{re} which can vary depending on η_1 and η_2. The reinjection point is obtained as follows. For the one dimensional map, we know that if the cell is in a bursting regime then at some finite number of iterations the cell will fall below the line $P(\eta) = \eta_{HC}$ or $P(\eta) = \eta_{SN^p}$, where HC and SN^p correspond to the homoclinic or the saddle node of periodics. SO, the cell jumps down to the lower branch of the curve S and it gets back to the active phase through the saddle node point η_{SN}.

In the two dimensional case, for each fixed η_j, there exists a η_i^*, which corresponds to a bifurcation on the fast subsystem, such that the graph $P_i(\eta_i, \eta_j)$ in the next iterate will fall into the silent phase. For each η_j, η_1^* maybe different, since η_1 and η_2 are moving at the same time. Suppose now that for a given η_j, the next value of $P_i(\eta_i, \eta_j)$ falls below η_i^*. Then, there are two possible situations to consider. One in which the two cells fall into the silent phase exactly at the same time. So, both cells will fall below the line $P_i = \eta_i^*$ and reinject, as in the one dimensional case, at $(\eta_1^{SN}, \eta_2^{SN})$, which maybe a curve, since this reinjection point depends on η_j. The second possibility refers to the case when only one cell falls down to the silent phase. The sudden fall of one of the cells to the silent phase may have two different effects on the other cell. Either, fast threshold modulation causes the cell to fall into the silent phase on the next iteration and reinject to the active phase again as in the previous case, or while one of the cells is in the silent phase the other cell hangs on the active phase for a while.

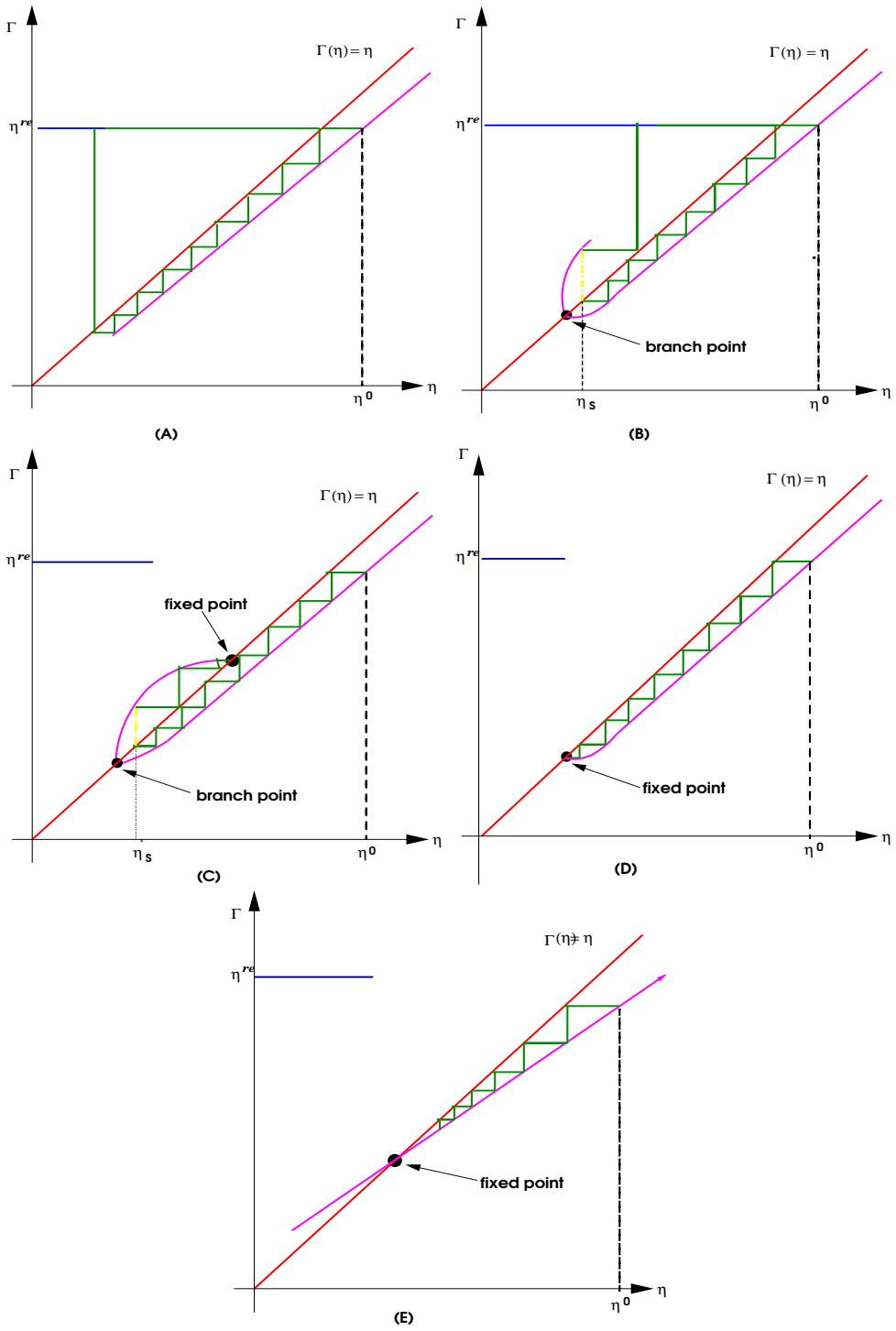

Figure 22: Five possible scenarios of cobwebbing for Γ_1 and Γ_2.

The latter case has a more complicated dynamics and it is not going to be dealt with in this work.

Finally, consider figure 8 and equations (4.1.4). In figure 8 for a pair (h_1, h_2) to the right of each of the averaged nullcline, numerical evidence shows that $\dot{h}_i < 0$ for $i = 1, 2$, to the left of both nullclines, $\dot{h}_i > 0$ for $i = 1, 2$ and for (h_1, h_2) in between the nullclines, the derivatives of the h_i with respect to time have opposite signs. This suggests, together with our numerical example, that $\frac{\partial P_i}{\partial \eta_j} < 0$ $i, j = 1, 2$ for all pairs (η_1, η_2) near entry into the active phase. From the equations (4.1.4) not much can be concluded given that we do not know exactly how each of the functions involved in the formulas are behaving.

In summary, for a pair (η_1, η_2) where both η_1 and η_2 decrease we have initially $\frac{\partial P_i}{\partial \eta_j} < 0$; if a branch point occurs, then for the corresponding map with branch point η_i increases and $\frac{\partial P_i}{\partial \eta_j}$ may or may not change signs.

Among some questions that remain to be answered is: What are conditions that allow a switch from iterating on the **LB** to iterating on **UB** for the iterated map? This question will be addressed next.

4.2.1 Condition(s) to switch from lower branch (LB) to the upper branch (UB) of either Γ_1 or Γ_2

Before addressing the condition for changing branches, let's define a few important things.

Definition 4.2.3 (Existence of nullclines)**.** *Let*

$$N_i(h_1, h_2) = \frac{1}{T(h_1, h_2)} \int_0^{T(h_1,h_2)} g(V_i(h_1, h_2, t), h_i)dt \quad i = 1, 2 \tag{4.2.1}$$

where $g(V_i(h_1, h_2, t), h_i) = \epsilon\tau_h(V_i(h_1, h_2, t))[h_\infty(V_i(h_1, h_2, t) - h_i)]$ *for* $i = 1, 2$ *is the right hand side of (3.2.1). Let* $H_1 = [h_1^{min}, h_1^{max}]$ *and* $H_2 = [h_2^{min}, h_2^{max}]$ *where* h_i^{min} h_i^{max} *are the minimum and maximum value of* h_i, i=1, 2 *on the active phase. Then, for* $i = 1$ *or* $i = 2$ *the* h_i *averaged nullclines exist if there exist* $\tilde{h}_1 \in H_1$ *and* $\tilde{h}_2 \in H_2$ *such that*

$$N_i(\tilde{h}_1, \tilde{h}_2) = 0. \tag{4.2.2}$$

Numerically we know that the h_1 and h_2 averaged nullclines exist in some parameter regimes (except in **SB**) [5]. Numerics also show that we cannot write the averaged nullclines as a function of either h_1 or h_2. Numerically, it seems that close to the identity line the nullclines could be written as functions. Thus assuming that trajectories of the full system (2.3.1)-(2.3.4) cross the nullclines close to the identity line we will assume that we can write the nullclines locally $h_2^n(h_1)$ and $h_1^n(h_2)$, there.

Let $h_2^t(h_1)$ denote the trajectory of the full system (2.3.1)-(2.3.4) near the nullcline. A condition for going from the lower branch to the upper branch is crossing the averaged nullcline, since at this point the h_2 or h_1 change directions. In terms of the map, with $\eta_1 = h_1$ and $\eta_2 = h_2$,

$$P_2^{i+1}(\eta_1^{i+1}, P_2^i(\eta_1^i, \eta_2^i)) > P_2^i(\eta_1^i, \eta_2^i) \quad \text{for some } i \in \aleph. \tag{4.2.3}$$

This means that for a give $i \in \aleph$ the next iteration of the map will be performed above the identity line (figure 23).

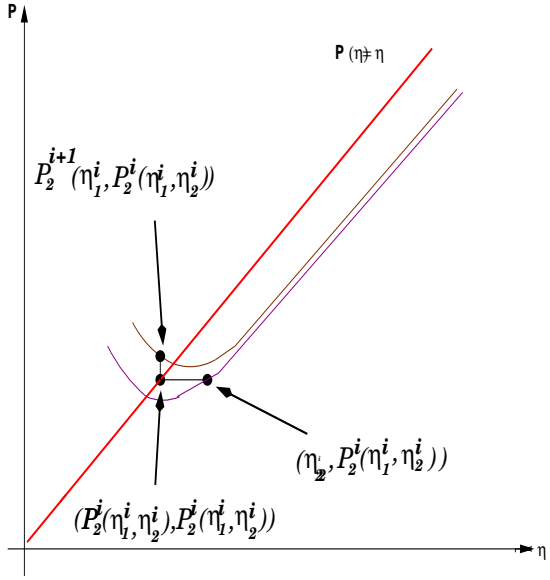

Figure 23: Cartoon showing the transition from the lower to the upper branch of the iterated map.

4.3 POSSIBLE OUTCOMES FOR THE ITERATED MAPS Γ_1 AND Γ_2 AND SOME NUMERICAL RESULTS

Suppose that the averaged nullclines exist. The numerical example together with the dynamics of the the system (2.3.1)-(2.3.4) depicted in the regions defined in the (g_{syn}, g_{ton}) parameter space by [5] suggest several possible outcomes for the shape that each of the iterated maps can take for a given set of parameters, if our network is either bursting or spiking.

The partition of the parameter space determined in [5] allows one to take a representative of each region and infer properties of the map in this region based upon the properties that the map will have for this particular value of (g_{syn}, g_{ton}). One also can use this map to determine conditions for the transition between two given regimes based upon the configuration of the iterated map. Finally, one can relate the corresponding iterated map to what is observed for the full system (2.3.1)-(2.3.4).

Assume that in the region of activity of the cells include values of $\eta_1 = h_1$ and $\eta_2 = h_2$ such that $\eta_1 \in [\eta_1^{min}, \eta_1^{max}]$ and $\eta_2 \in [\eta_2^{min}, \eta_2^{max}]$, where max and min indicate, respectively, the maximum and minimum values for each of the η_i on the active phase. As it is known from [5], the max and min for η_1 and η_2 are related and they will depend upon the level of tonic and synaptic inputs given to both cells. Except for the parameter values in region AB, all other choices of parameters were made based on figure 8 from Best *et al* [5]. These choices were made to compare our results to what was observed in their work. For all numerical simulations shown below, the network was initialized with non-identical initial conditions.

4.3.1 Possible mechanisms for the transition between regimes

In this section, we would like to give a description of possible forms the iterated map can take. Here we will assume an initial shape for the iterated map and using this initial state we will give (derive) possible forms that the iterated maps can take and conditions for the transition between different maps in a compact way. These conditions will be later related to the four regions described in [5].

For all the cases discussed below, we consider that when one cells jumps to the active phase or goes to the silent phase, the other cell also will do it right away.

Assume that for a given pair (g_{syn}, g_{ton}), close to the boundary with the quiescence region, the two iterated maps look like the iterated maps in figure 24. According to these pictures, the cells are bursting given that there is no fixed point of the iterated maps and, therefore, the two cells have to fall into the lower branch of the critical manifold and reinject back to the active phase to a larger value of η_j.

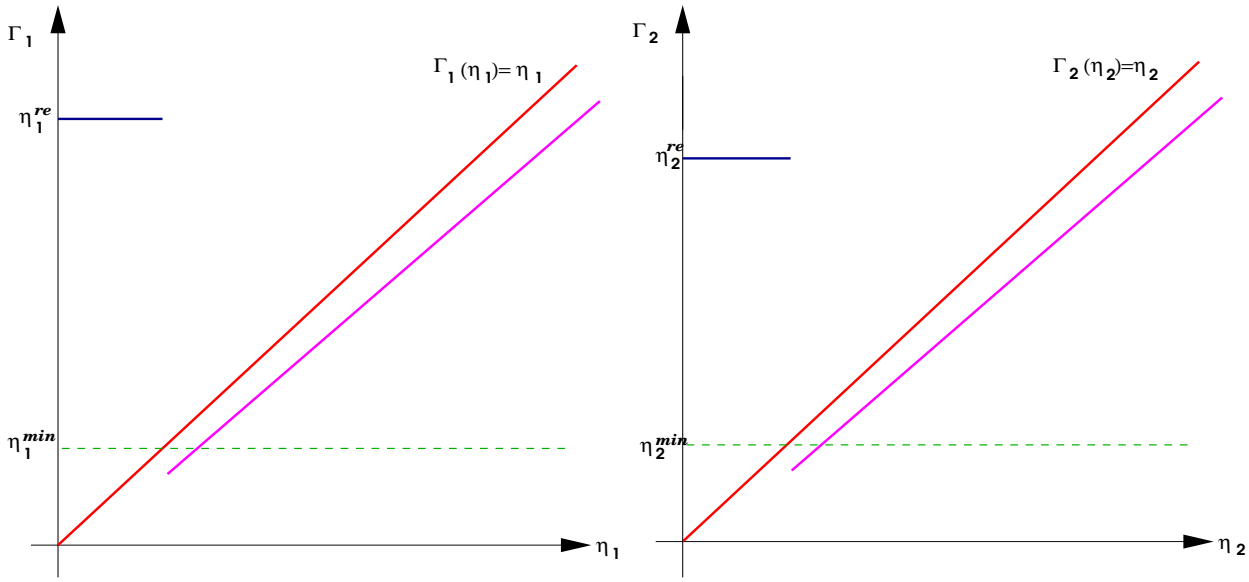

Figure 24: Cartoons describing possible representatives of a region where both iterated maps do not have true fixed points or branch points. Here $(\eta_1^{min}, \eta_2^{min})$ are the minimum values of η_1 and η_2, respectively, for which the two cells are still in the active phase. Also, $(\eta_1^{re}, \eta_2^{re})$ are the η_1 and η_2 values for which the two cells are reinjected back to the active phase after a period of recovery.

Proposition 4.3.1. *If there exists a pair* (η_1^*, η_2^*) *such that* $(P_1(\eta_1^*, \eta_2^*), P_2(\eta_1^*, \eta_2^*)) = (\eta_1^*, \eta_2^*)$ *and this fixed point is stable, then* $\Gamma_1(\eta_1^*) = \eta_1^*$ *and* $\Gamma_2(\eta_2^*) = \eta_2^*$.

Proposition 4.3.2. *If* (Γ_1, Γ_2) *is the iterated map generated by* $\mathbf{P} = (P_1(\eta_1, \eta_2), P_2(\eta_1, \eta_2))$ *with initial condition* (η_1^0, η_2^0) *and there exists* η_1^*, *not a branch point, such that* $\Gamma_1(\eta_1^*) = \eta_1^*$, *then there exists* η_2^* *such that* $\Gamma_2(\eta_2^*) = \eta_2^*$ *and such that* (η_1^*, η_2^*) *is a stable fixed point of* $\mathbf{P}$.

Making use of these propositions, let's determine possible forms that the iterated maps can take if we increase g_{ton}.

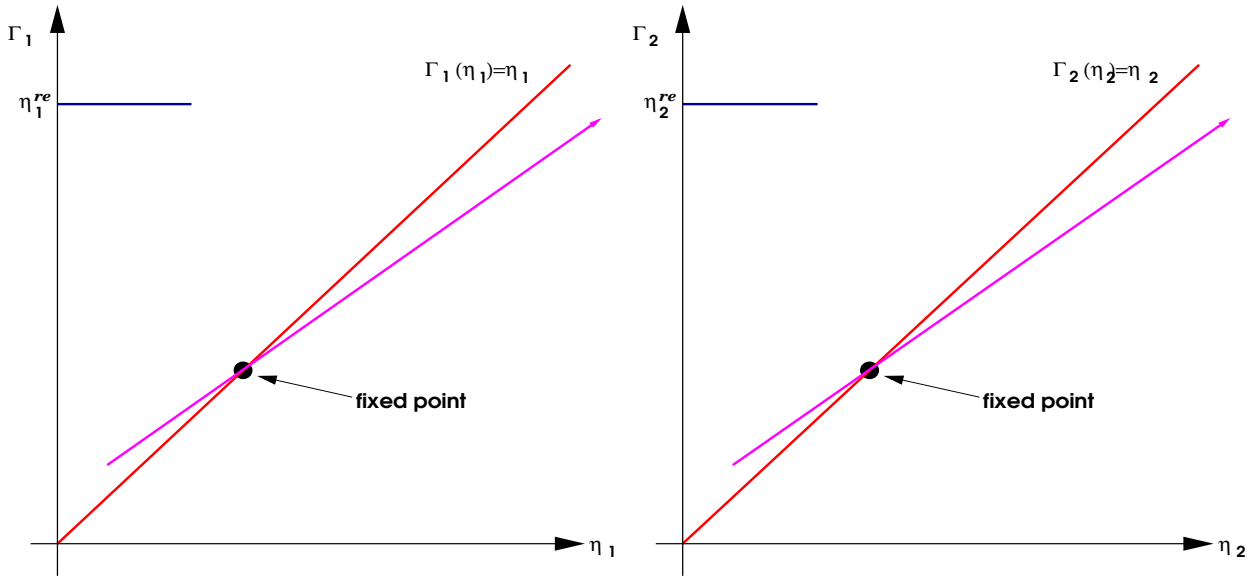

Figure 25: Possible outcome for iterated maps in figure 24, if the iterated maps remain linear for increasing g_{ton}.

Assuming that both iterated maps remain linear for all the time when inside the active region then, the only possible qualitative change of the map is the presence of a fixed point (figure 25). In this case, both iterated maps get trapped into a stable fixed point and stay there and the cells are spiking. This is similar to what is seen for region **SS** in [5].

Another possibility is to have one of the iterated maps, say Γ_2 in figure 24, to stay linear and below the identity line and the other map Γ_1 to cross the identity line in a nonlinear fashion. Then, before the map reaches the point where $\Gamma_1 = \eta_1$, the values of the iterated map are decreasing given that $\frac{\partial P_1}{\partial \eta_2} < 0$ for all η_2. As soon as we cross the identity line, we have the iterated map increasing with η_2 decreasing. In this case, the two dimensional iterated map still does not have a fixed point and the cells must leave the region of activity as before. The cells are still bursting but there is a qualitative change in the type of the bursting seen. This setup is similar to the description of region **AB** in [5] and it is shown in figure 26. Also, if the two iterated maps have the same form as Γ_1 in figure 26, then we are still in region **AB** (figure 27).

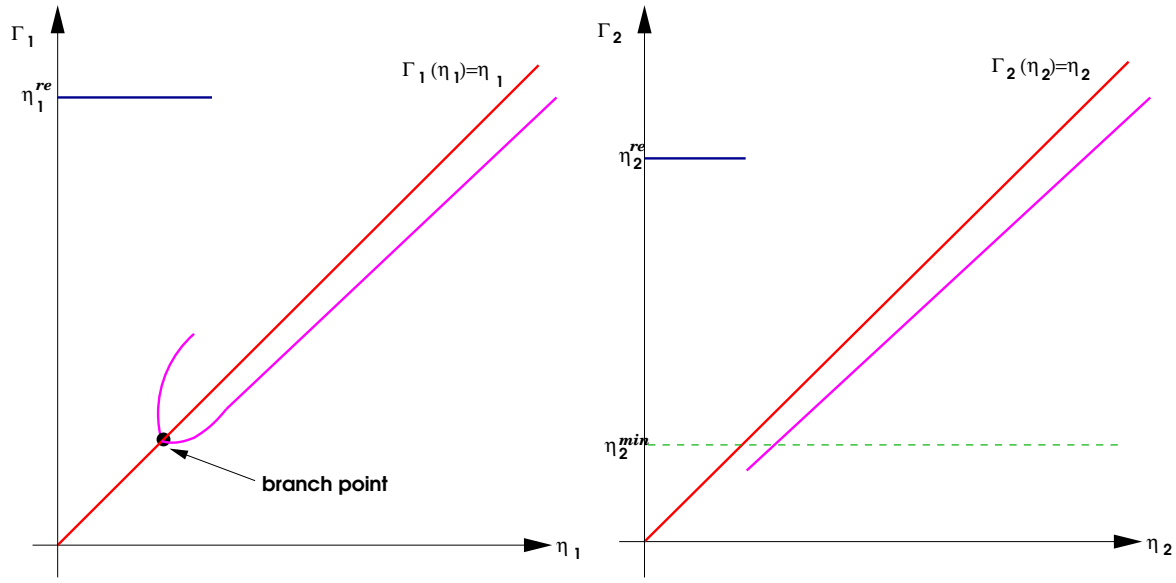

Figure 26: Possible outcome for Γ_1 and Γ_2 with the presence of at least one of the maps with a branch point.

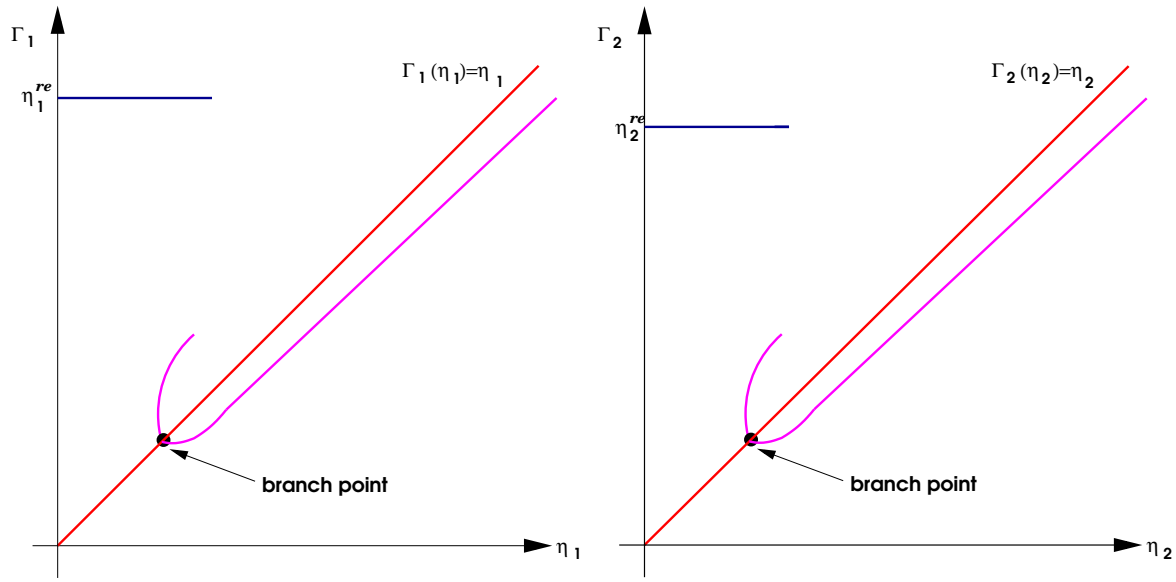

Figure 27: Possible outcome for Γ_1 and Γ_2 with the presence of at least one of the maps with a branch point.

With increasing g_{ton}, a qualitative change in the form of the iterated maps in figure 26 would be the presence of a fixed point(figure 28). In this setup the fixed point is stable and as soon as the iterates reach the fixed point they will stay trapped in there. This situation is equivalent to region **AS** described in [5]. Similar explanation holds true when determining a possible form for the iterated maps in figure 27. That is, the two iterated maps will have a branch point and a fixed point and the cells are also spiking.

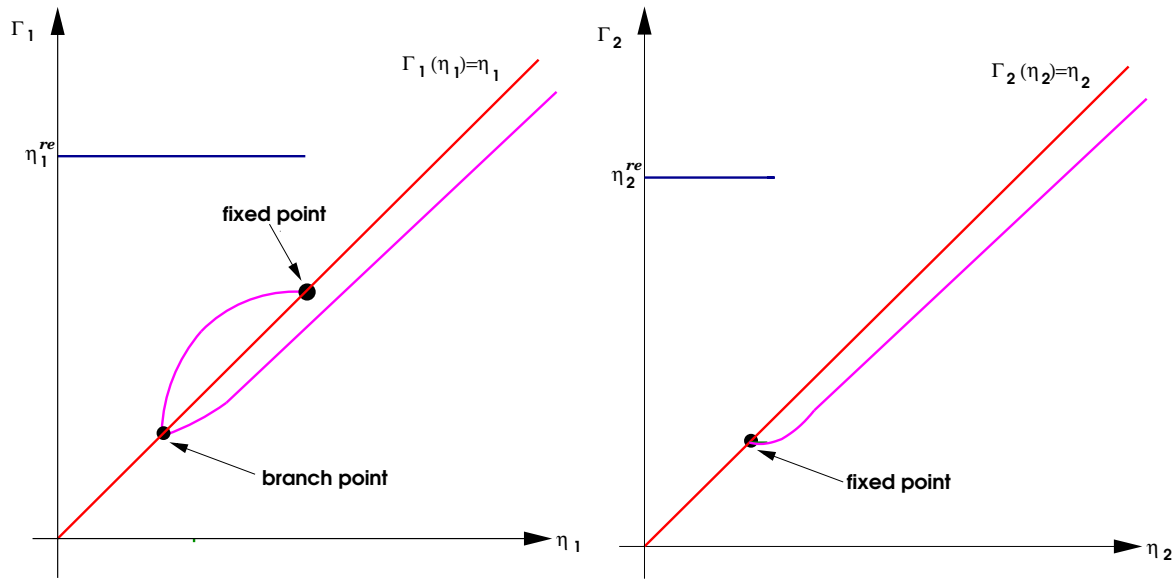

Figure 28: Transition from figure 26.

Finally, increasing g_{ton} even further can make the branch point and fixed point in figures 28 and 29 to come together and the map will qualitatively similar to figure 25. In this case, the two cells will still be spiking but this time the cells will go directly to the fixed point instead of crossing the identity at distinct times and then going to the fixed point. This case represents the transition from region **AS** to **SS**.

We claim that the forms of the map discussed above are the only possible forms that the map can assume and they well described the possible scenarios for the transition between different regimes.

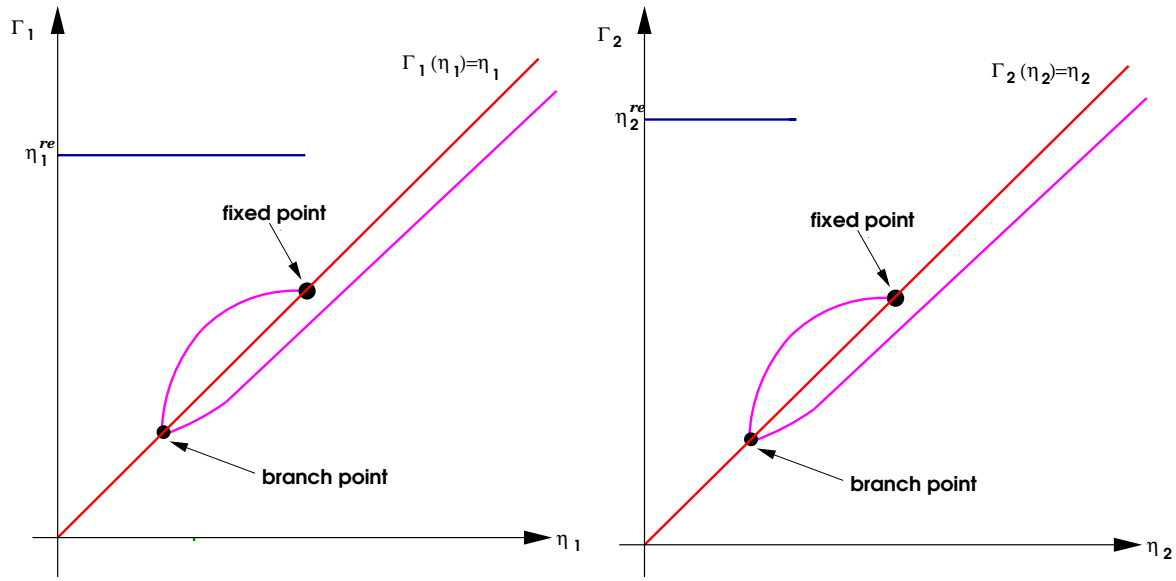

Figure 29: Transition from figure 27.

Below, we show one numerical example along with cartoon representation for the iterated map in each of the four regions described in [5] and how above description fits what has been observed before.

4.3.2 Region SB

In this region, trajectories of the full system (2.3.1)-(2.3.4) on the (h_1, h_2) plane will oscillate symmetrically around the identity line until the cells leave the oscillatory region O. Trajectories never cross the averaged nullcines inside O since they are outside O. Thus, it is expected that the iterated maps Γ_1 and Γ_2 do not have fixed points or branch points, that is, $\Gamma_1(\eta_1, \eta_2) \neq \eta_1$ and $\Gamma_2(\eta_1, \eta_2) \neq \eta_2$ for all pairs (η_1, η_2) in O.

Proposition 4.3.3. *Consider intervals (η_0^1, η_R^1) and (η_0^2, η_R^2) for $\eta_0^1 \geq \eta_L^1$ and $\eta_0^2 \geq \eta_L^2$ where η_R^i and η_L^i $i = 1, 2$ are the maximum and minimum values of η_i in the active phase. Then, if there exists η_1 and η_2 such that $\eta_2 = \eta_1 + O(\epsilon)$ with ϵ positive and small, then*

$$\Gamma_1 = \Gamma_2 + O(\epsilon) \tag{4.3.1}$$

Proof. Taylor expanding the exponential $e^{-\alpha_1(T_s)}$ up to $O(\epsilon^2)$ and some simple algebra on

$$\Gamma_1(\eta_1, \eta_2) = e^{-\alpha_1(T_s)}(\eta_1 - \Psi_1) + \Psi_1 \tag{4.3.2}$$

yields

$$\Gamma_1(\eta_1, \eta_2) \approx (1 - \alpha_1(T_s))\eta_1 + O(\epsilon^2) = \eta_1 - O(\epsilon). \tag{4.3.3}$$

where $\alpha_1(T_s)$, defined as in equation (4.1.5), is a $O(\epsilon)$ term. A similar argument produces

$$\Gamma_2(\eta_1, \eta_2) \approx (1 - \alpha_2(T_s))\eta_2 + O(\epsilon^2) = \eta_2 - O(\epsilon) \tag{4.3.4}$$

But, using the assumption $\eta_1 = \eta_2 + O(\epsilon)$, then equation (4.3.1) is obtained. □

If the above hold true one can also conclude that $\Gamma_1 < \eta_1$ and $\Gamma_2 < \eta_2$ for all η_1 and η_2, since $\alpha_1(T_s)$ and $\alpha_2(T_s)$ are both positive. In figure 30 (top), a cartoon shows how typical iterated maps in this region appear. For comparison, a numerical plot of the iterated maps Γ_1 and Γ_2 are shown in the same figure in the bottom panels. In the numerical examples, $g_{syn} = 0.107143$ and $g_{ton} = 0.02036$ were used to obtain the given iterated maps. As one can see, the numerical results and the predictions are a very good match.

4.3.3 Region AB

In this parameter region, the averaged nullclines are inside the oscillatory region. Trajectories of the full system (2.3.1)-(2.3.4) on the (h_1, h_2) space after some transient will follow the identity line and after some time will cross one of the averaged nullclines, but may not necessarily cross both. After an averaged nullcline is crossed then there will be a change in drifting direction for either h_1 or h_2. Unless trajectories hit a fixed point of the system, the averaged nullclines will be crossed at distinct times. After leaving O, trajectories follow the lower branch of the curve of steady states S, for increasing h_1 and h_2, until SN is reached. At this point the 2 cells jump back to the active phase. As a final note, it is known from [5] that the averaged nullclines cross each other on the identity line, but since the resulting fixed point is unstable it will be reached only for very special initial conditions. This case with be discussed later.

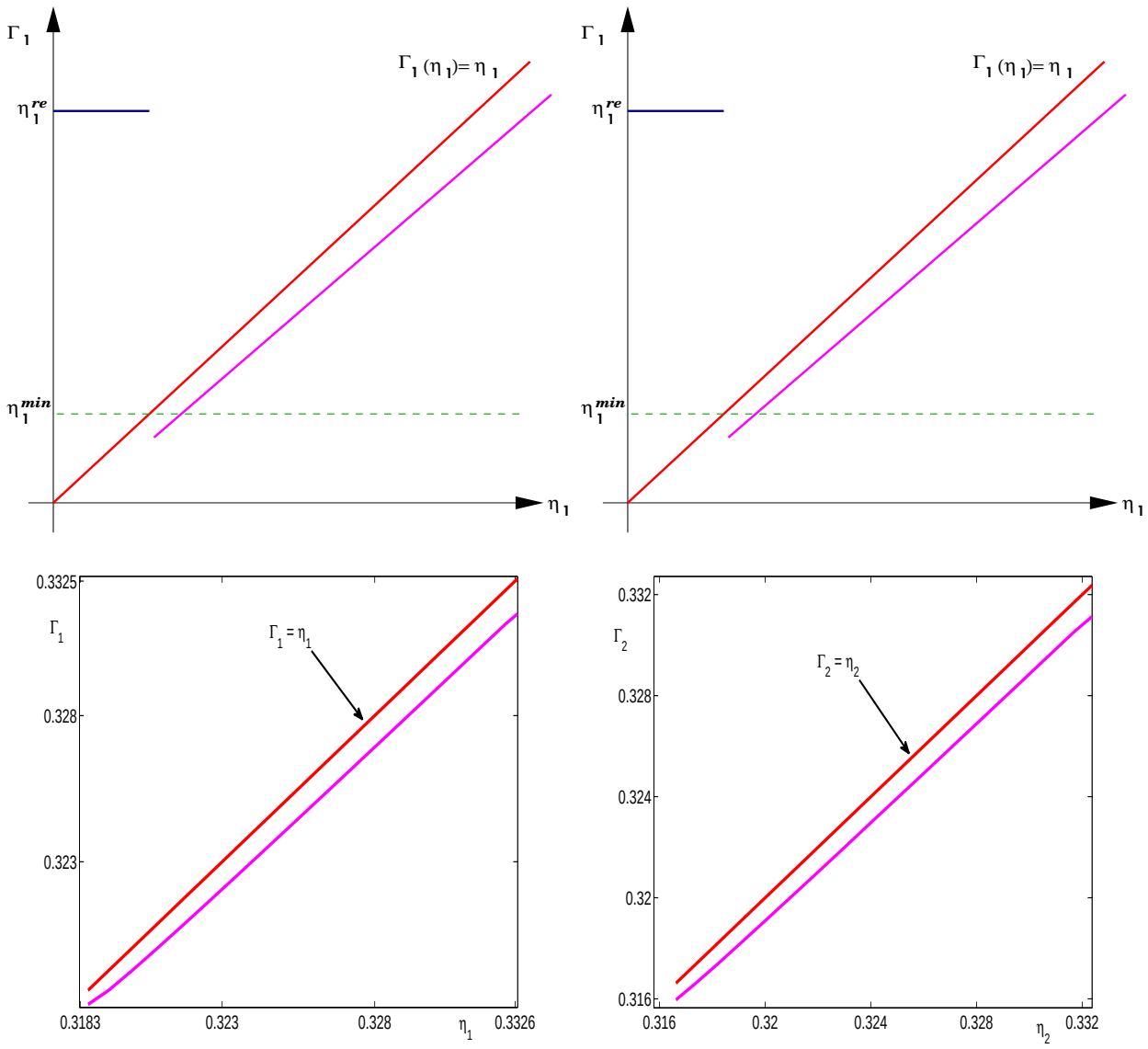

Figure 30: *top* - Cartoons describing possible representatives of a region where both iterated maps do not have true fixed points or branch points. *bottom* - Figures show numerically compute iterated maps for the $g_{syn} = 0.107143$ and $g_{ton} = 0.02036$ for all other parameters fixed. These values of g_{syn} and g_{ton} correspond to $g_{syn} = 3$ and $g_{ton} = 0.57$ in [5] (see figure 21).

So, in this region we expect that at least one of the iterated maps will have a branch point, due to the change in drift direction after the nullcline is crossed. Therefore, one or both iterated maps will deviate from linear near the branch point. Since trajectories initially remain approximately close to the identity line, then the iterated map is expected to have also a region where it behaves linearly.

In figure 31, cartoons show what we expect as some possible forms of the iterated maps in this region. Roles of Γ_1 and Γ_2 may be reversed, depending on initial conditions.

In figure 21 (shown in section 4.2), numerically generated iterated maps Γ_1 and Γ_2 are shown for $g_{syn} = 0.107143$ and $g_{ton} = 0.0275$. These results are as expected for iterated maps in this region.

4.3.4 Region AS

In region **AS**, trajectories of the full system (2.3.1)-(2.3.4) move toward two stable ($h_1 \neq h_2$) and one unstable fixed point ($h_1 = h_2$) on the (h_1, h_2) space inside the oscillatory region for the averaged nullclines. Starting with initial conditions close to the identity line, trajectories will cross the h_1 or h_2 nullclines and will go to the stable fixed points [5]. Depending if we start above or below the identity line, the solution of the full system will go to one or the other stable fixed point. Starting with initial conditions such that $h_2 > h_1$, trajectories of the full system will go to the fixed point above the identity line whereas initial conditions such that $h_1 < h_2$ will take trajectories to the fixed point below the identity line.

In terms of iterated maps, at least one of the iterated maps Γ_1 or Γ_2 will have a branch point, and both will have a stable fixed point. For the iterated map with both a branch point and true fixed point, one expects that the map would go through the branch point and move on until it gets stuck in a small neighborhood of the fixed point. If one of the iterated map has only a fixed point then, iterates of the map will close in the true fixed point and stay there. Figures 26 and 27 show possible shapes for the iterated maps.

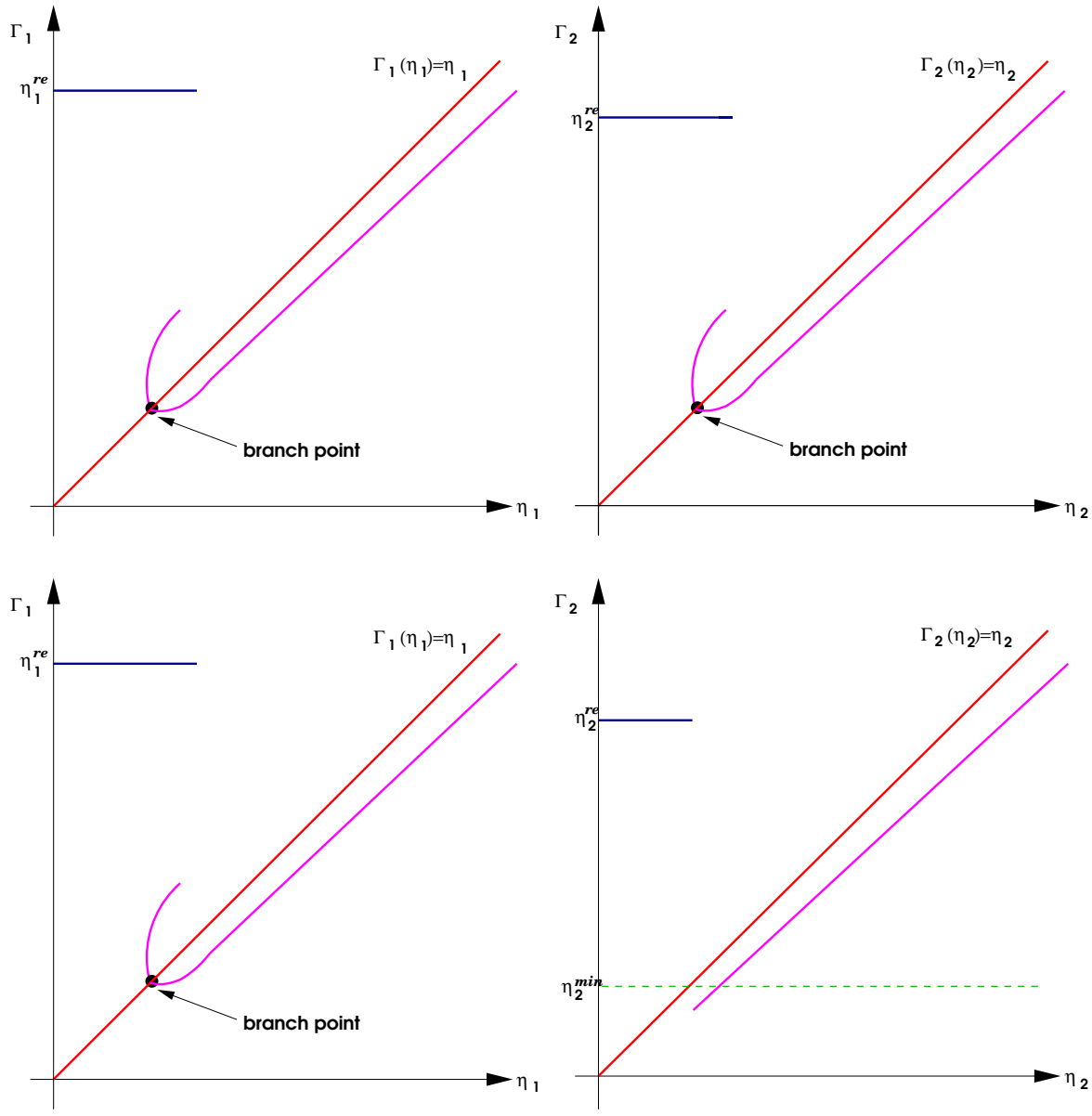

Figure 31: Each row represents a possible outcome for Γ_1 and Γ_2 with the presence of at least one of the maps with a branch point.

Figure 32 show numerical results for the iterated maps corresponding to $g_{syn} = 0.107143$ and $g_{ton} = 0.03107$. The top 2 pictures show Γ_1 versus η_1. The top left figure shows how close the iterated map is from the identity line and on each iterate we get closer and closer to the fixed point, according to the zooming on the right panel. The bottom 2 figures show Γ_2 versus η_2. This map was expected to have a fixed point and a branch point. It has a branch point and after 200 iterates of the map it seems to get closer and closer to the fixed point. A closer look into the branch point region reveals that the iterates seem to be very close to the identity line. We cannot reach the fixed point due to the fact that the averaged nullclines are very close to each other and the iterates of the map somehow go back and forth, crossing the 2 nullclines simultaneously (figure 32(bottom)). Although we do not have exactly the form we expected, qualitatively figure 32 is similar to what is expected. That is, the iterated map Γ_1 is tending to a fixed value of η_1 whereas Γ_2 has a branch point and it is tending to a fixed point.

This behavior is expected due to the fact that trajectories of the full system, stay lose to the fixed point but do not necessarily reach it.

4.3.5 Region SS

In this region, the averaged nullclines intersect exactly once inside the oscillatory region, on the $h_1 = h_2$ line, and the fixed point is stable. The 2 other fixed points collapsed into the previously unstable fixed point to give rise to a stable fixed point. Trajectories of the full system (2.3.1)-(2.3.4), after some transient has passed, will wiggle around the identity line and will converge to this stable fixed point. As for the iterated map, we expect them to have only true fixed points. No branch points are expected for the iterated maps in this region. Figure 33(top) shows cartoon for typical representatives of iterated maps in this region.

Figure 33(bottom), shows iterated maps obtained numerically for $g_{syn} = 0.107143$ and $g_{ton} = 0.0325$). It can be seen that both iterated maps go to their fixed points and stay there. A closer look in the region close to the tip of the map indicates that the iterates of both maps wiggle around the identity line never leaving this region (figures not shown).

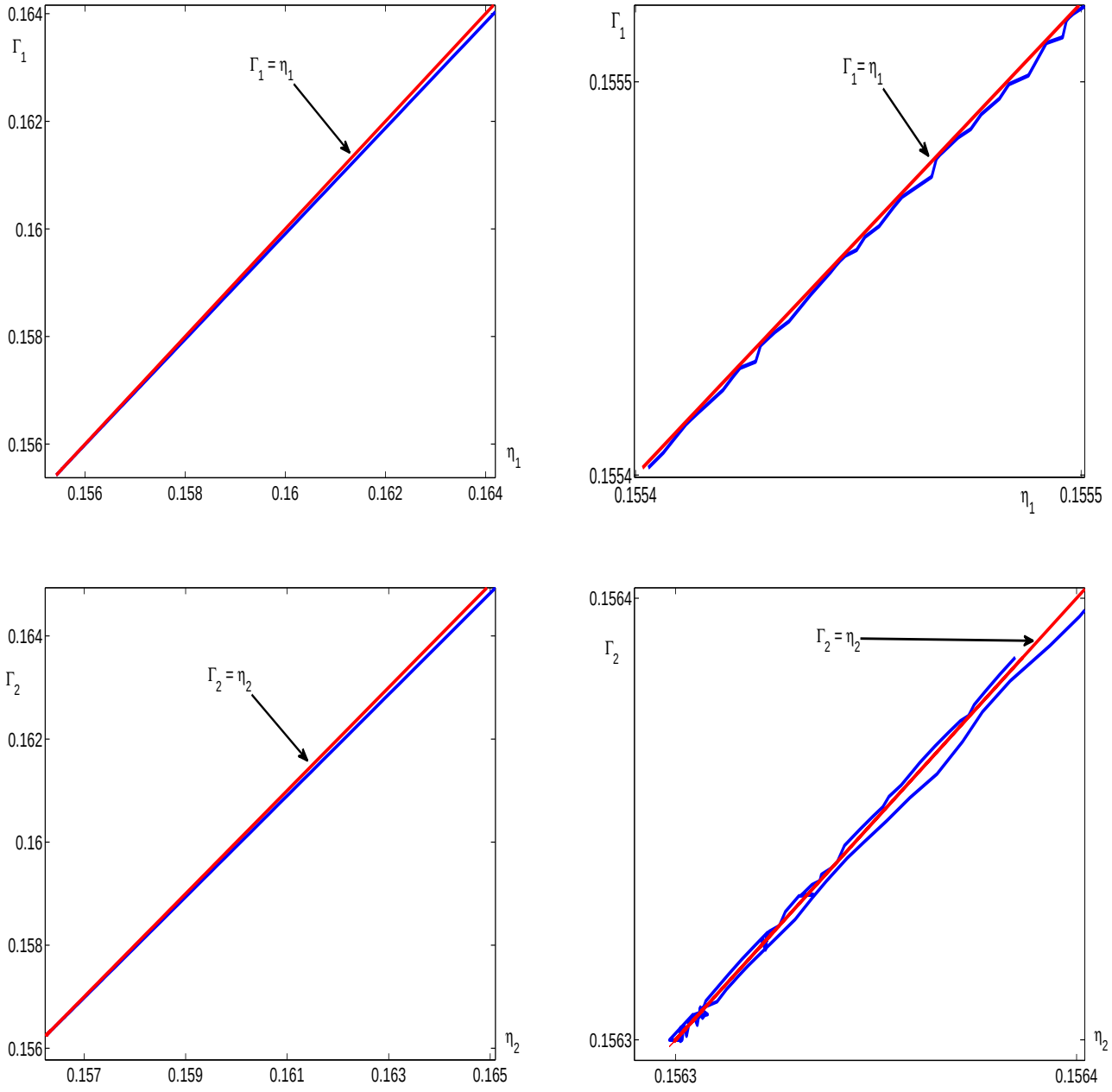

Figure 32: Numerical results for parameters in region **AS** for $g_{syn} = 0.107143$ and $g_{ton} = 0.03107$.

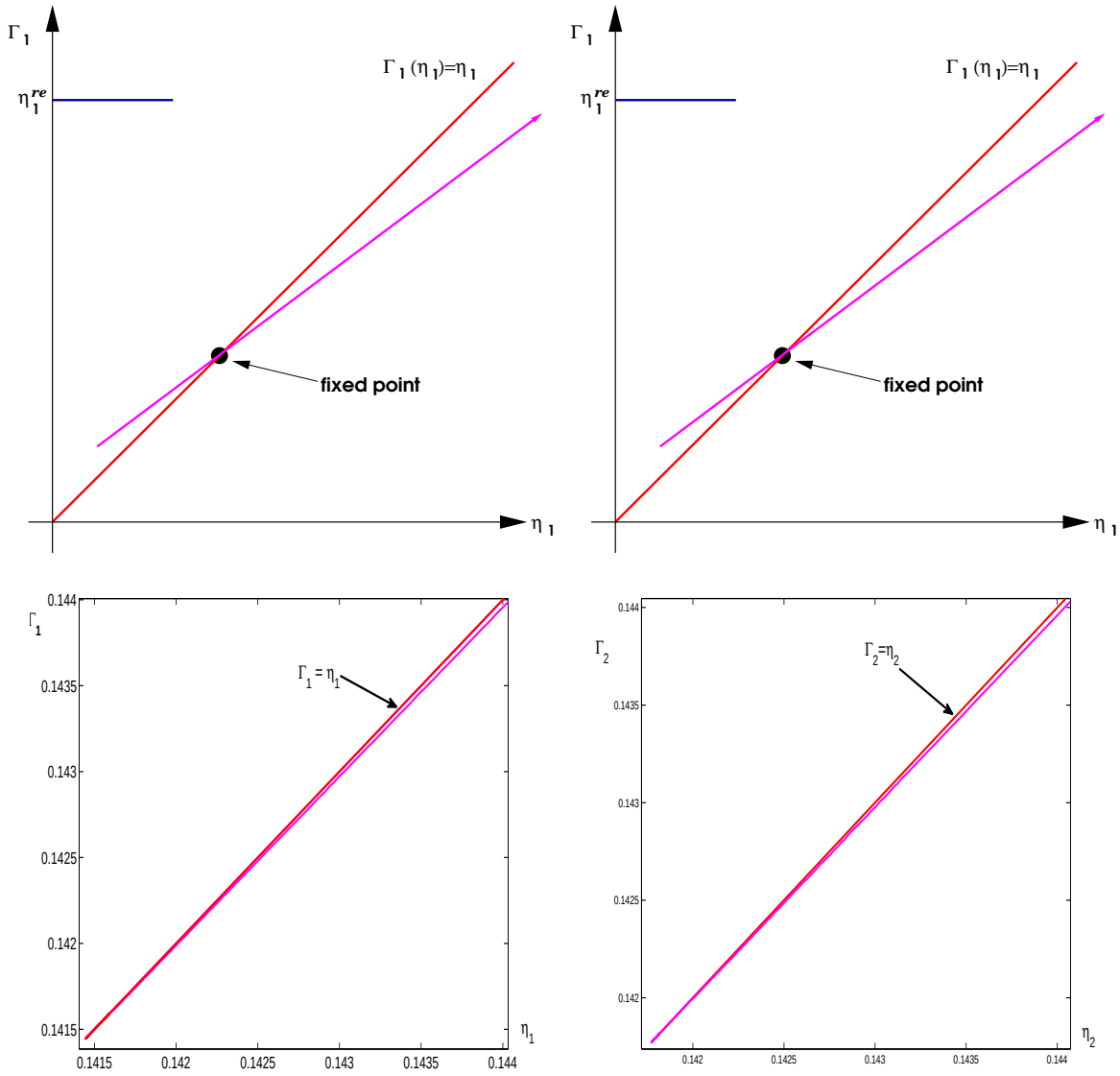

Figure 33: *top* - Typical iterated maps for region **SS**; *bottom*- Numerical example show how close the solutions of the numerically iterated maps and our predictions are.

This behavior could be expected due to that after a transient trajectories of the full system (2.3.1)-(2.3.4) wiggle around the fixed point never actually reaching it exactly.

An important question to be answered at this point is: what are the mechanisms for the transition between the different regions described above?

In the iterated maps, going from **AB** to **AS** implies the appearance of a true fixed point, with at least one of the iterated maps having a branch point.

Finally, the transition from **AS** to **SS**, for the original system takes place when the three fixed points of the averaged nullclines collapse into a single stable fixed point located on the identity line. In terms of the iterated map, the transition from **AS** to **SS** will occur when the branch point and the true fixed point collapse together to give rise to a single true fixed point for the iterated map $\mathbf{\Gamma}$.

As remark, it seems reasonable to assume that adding heterogeneity to the full system will likely change the structure of the iterated maps, and the resulting iterated map will likely be some combination of the 4 cases mentioned above. It is also likely that initial conditions will play an important role in determining the different regimes the network may enter.

4.4 SYNCHRONOUS SOLUTIONS

When full system (2.3.1)-(2.3.4) is simulated with the two cells at different initial conditions for a given set of parameters, the action potentials of the two cells are fired in anti-phase (AP), no matter whether the cells are spiking or bursting. Now, suppose the two cells start with exactly the same initial conditions,that is, at $T = 0$, $V_1 = V_2$, $n_1 = n_2$, $s_1 = s_2$ and $h_1 = h_2$. Then, for all $T > 0$, $V_1(T) = V_2(T)$, $n_1(T) = n_2(T)$, $s_1(T) = s_2(T)$ and $h_1(T) = h_2(T)$. This solution matches the solution for the self coupled single cell case. In this case, the 2 cells are said to be synchronized or that the given solution is synchronous or in-phase (IP). But, in terms of stability analysis, the stability of the fixed point for the one dimensional map P requires only to determine $\frac{dP}{d\eta}$. However, in order to determine the stability of the fixed point for the IP solution for the two cell network, it is necessary to compute the eigenvalues of the Jacobian matrix of the two dimensional map about the fixed

point.

In region **SS** there are two possible solutions: nonidentical initial conditions take trajectories of the full system to the stable fixed point p_0. Identical initial conditions take trajectories of the full system to the the fixed point of the self coupled single cell case, and the two cells are firing action potentials exactly at the same time.

An example of the difference between the IP and AP solutions, in region **SS** is shown in figure 34 (left panel), after some transient has been eliminated for $g_{syn} = 0.107143$ and $g_{ton} = 0.0325$. In this figure, the full system of equations were simulated to give rise to both solutions with slightly different initial conditions. Here, V_s represents the voltage for the IP solution and V_1^a and V_2^a represent the voltages for cells 1 and 2, respectively for the AP solution. Note how different these solutions are from each other. In figure 34 (right panel), it is shown how the corresponding dynamics of the h_i's are also different. This difference in the h_i's is due to coupling effects which tend to push the dynamics of the cell(s) to lower values of h in the 2 cell case [5].

As shown in figure 9 (chapter 2), the IP and AP solutions are close to each other for $g_{syn} = 0.107143$ and $g_{ton} = 0.0325$. With a perturbation of 10^{-5}, the AP solution barely changes whereas the IP solution may significantly differ from the unperturbed state (figure not shown).

For $g_{syn} = 0.107143$ and $g_{ton} = 0.0325$, with non-identical initial conditions, the (stable) fixed point of the system for the 2 cell case takes place for h_1 and h_2 approximately 0.1415. However, starting the 2 cells with identical initial conditions one finds that the (unstable) fixed point is $h_1 = h_2 \approx 0.1662$, which matches exactly the fixed point for the self coupled case [5]. For any initial condition, the system is spiking.

As a remark, not always the IP and AP solutions correspond to the same type of solution on a given region. For $g_{syn} = 0.2857$ and $g_{ton} = 0.02857$, the synchronous solution corresponds to bursting whereas the asynchronous solution corresponds to spiking, as expected (pictures and results not shown).

In table 4, it is shown the location of the fixed points for the one and two dimensional iterated maps for $g_{ton} = 0.0275, 0.03107, 0.0325$ and $g_{syn} = 0.107143$. For all these values of g_{ton}, the full system (2.3.1)-(2.3.4)is spiking.

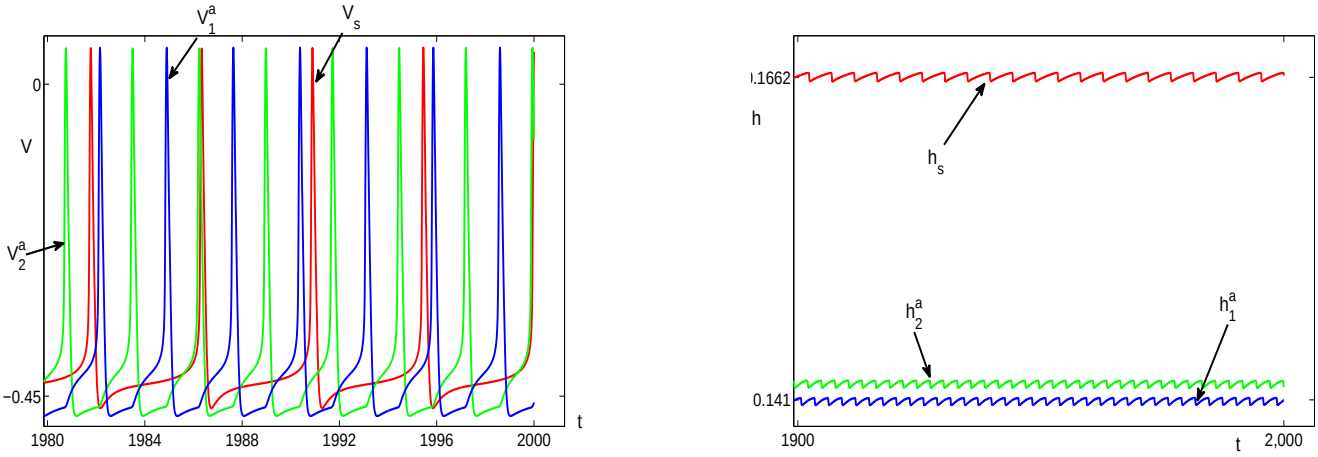

Figure 34: Comparison between solutions for the single self coupled case and two coupled cell case for $g_{syn} = 0.107143$ and $g_{ton} = 0.0325$. In the top left V_s, V_1^a and V_2^a correspond respectively to the solution for the self coupled single cell case and the voltages of the asynchronous solution. At the bottom h_s, h_1^a and h_2^a represent, respectively the gating variables for the self coupled single cell case and the gating variables for the asynchronous solution.

g_{ton}	h^*	$\mathbf{h}^* = (h_1^*, h_2^*)$
0.0325	0.16629	(0.16622, 0.16622)
0.03107	0.18328	(0.18325,018325)
0.0275	0.23042	(0.23042,0.23042)

Table 4: Fixed points for the one and two dimensional maps for $g_{syn} = 3$ and several values of g_{ton}. These values of g_{ton} are representative of the regions (from top to bottom): SS, AS and AB . The fixed points for the two dimensional map were obtained by starting with identical initial conditions for the two cells, that is, $V_1 = V_2$, $n_1 = n_2$, $s_1 = s_2$ and $h_1 = h_2$.

Due to some numerical error, the values of the fixed points do not match exactly with differences arising on the fifth decimal place.

4.5 STABILITY ANALYSIS OF THE FIXED POINTS OF THE $2D$ MAP

A fixed point $(\bar{\eta}_1, \bar{\eta}_2)$for the $2D$ iterated map exists if

$$\mathbf{P}(\bar{\eta}_1, \bar{\eta}_2) = \begin{bmatrix} \bar{\eta}_1 \\ \bar{\eta}_2 \end{bmatrix} \Longleftrightarrow \mathbf{F}(\bar{\eta}_1, \bar{\eta}_2) = \begin{bmatrix} \bar{\eta}_1 \\ \bar{\eta}_2 \end{bmatrix}. \tag{4.5.1}$$

Uniqueness of $(\bar{\eta}_1, \bar{\eta}_2)$ will depend on whether the iterated functions F_1 and F_2 are monotone. So far, numerical results do not seem to show that monotonicity of F_1 and F_2 is the case, as a general rule (figures not shown).

4.5.1 Some preliminaries

Let $(\bar{\eta}_1, \bar{\eta}_2)$ be a fixed point of the iterated map. Then, there are 2 cases to be analyzed: $\bar{\eta}_1 = \bar{\eta}_2$ and $\bar{\eta}_1 \neq \bar{\eta}_2$. The case $\bar{\eta}_1 = \bar{\eta}_2$ can be further divided in to 2 subcases: the 2 cells can be IP or AP.

In general, for a system of ordinary differential equations, a fixed point is stable if small perturbations in the neighborhood of the fixed point results in returning to the fixed point again. Otherwise, the fixed point is unstable. For a two dimensional map, a fixed point is *stable* if $|\lambda_1| < 1$ and $|\lambda_2| < 1$, *unstable* if $|\lambda_1| > 1$ or $|\lambda_2| > 1$ (see [27], p.16), where λ_1 and λ_2 are the eigenvalues of the linearized system about the fixed point. For the synchronous solutions, we conjecture that the eigenvalues will be such that $|\lambda_1| < 1$ and $|\lambda_2| > 1$, since the IP solution relates to the single self coupled case and the fixed point there is stable meaning that in at least one of the directions the fixed point should be attracting. For the asynchronous solution, stability of the fixed point will depend on the particular regime and the parameter set.

4.5.2 Jacobian matrix and eigenvalues

Suppose that for some fixed value of g_{syn}, the fixed point $(\bar{\eta_1}, \bar{\eta_2})$ exists. Let $\bar{}$ denote the evaluation of a given function at $(\bar{\eta_1}, \bar{\eta_2})$.

In order to determine stability of the fixed point, we linearize about $(\bar{\eta_1}, \bar{\eta_2})$ and compute the eigenvalues of the Jacobian matrix. The Jacobian matrix for P_1, P_2, denoted by $DP(\eta_1, \eta_2)$, is given by:

$$DP(\eta_1,\eta_2) = \begin{bmatrix} \frac{\partial F_1}{\partial \eta_1} & \frac{\partial F_1}{\partial \eta_2} \\ \frac{\partial F_2}{\partial \eta_1} & \frac{\partial F_2}{\partial \eta_2} \end{bmatrix} + \begin{bmatrix} e^{-\alpha_1(T_s)}\left(1-\frac{\partial F_1}{\partial \eta_1}\right) & e^{-\alpha_1(T_s)}\left(-\frac{\partial F_1}{\partial \eta_2}\right) \\ e^{-\alpha_2(T_s)}\left(-\frac{\partial F_2}{\partial \eta_1}\right) & e^{-\alpha_2(T_s)}\left(1-\frac{\partial F_2}{\partial \eta_2}\right) \end{bmatrix} + \begin{bmatrix} \frac{\partial e^{-\alpha_1(T_s)}}{\partial \eta_1}(\eta_1 - F_1) & \frac{\partial e^{-\alpha_1(T_s)}}{\partial \eta_2}(\eta_1 - F_1) \\ \frac{\partial e^{-\alpha_2(T_s)}}{\partial \eta_1}(\eta_2 - F_2) & \frac{\partial e^{-\alpha_2(T_s)}}{\partial \eta_2}(\eta_2 - F_2) \end{bmatrix}. \quad (4.5.2)$$

The eigenvalues of the linearized system are obtained by solving for λ, the following determinant

$$det(D\bar{P} - \lambda I) = 0 \quad (4.5.3)$$

where I is a 2×2 identity matrix.

4.5.2.1 Case 1 : $\bar{\eta_1} = \bar{\eta_2}$ At $(\bar{\eta_1}, \bar{\eta_2})$, assume that $\frac{\partial \bar{F_1}}{\partial \eta_1} = \frac{\partial \bar{F_2}}{\partial \eta_2}$ and $\frac{\partial \bar{F_1}}{\partial \eta_2} = \frac{\partial \bar{F_2}}{\partial \eta_1}$ and $\bar{\alpha}_1(T_s) = \bar{\alpha}_2(T_s)$(since at $(\bar{\eta_1}, \bar{\eta_2})$, $V_1 = V_2$). These assumptions only hold true for the fixed points of the iterated maps corresponding to synchronous solutions.

Let $a = \frac{\partial \bar{F_1}}{\partial \eta_1}$, $b = \frac{\partial \bar{F_1}}{\partial \eta_2}$, $c = (1-a)e^{-\bar{\alpha}_1(T_s)}$ and $d = -be^{-\bar{\alpha}_1(T_s)}$. Then, the Jacobian matrix in (4.5.2) can be written as

$$\overline{DP} = \begin{bmatrix} a+c & b+d \\ b+d & a+c \end{bmatrix}. \quad (4.5.4)$$

The eigenvalues for $\overline{DP}$ are given by:

$$\lambda_1 = (a+b)(1-e^{-\bar{\alpha}_1(T_s)}) + e^{-\bar{\alpha}_1(T_s)} \quad (4.5.5)$$

$$\lambda_2 = (a-b)(1-e^{-\bar{\alpha}_1(T_s)}) + e^{-\bar{\alpha}_1(T_s)} \quad (4.5.6)$$

with corresponding eigenvectors,

$$\mathbf{u} = \begin{bmatrix} 1 \\ 1 \end{bmatrix} \quad \text{and} \quad \mathbf{v} = \begin{bmatrix} 1 \\ -1 \end{bmatrix}$$

Notice that **u** and **v** are orthogonal to each other.

Considering the similarities of the solutions for the self coupled single cell case and the synchronous solution, it is easy to believe that the eigenvalues λ_1 and λ_2 must related to $\frac{dP}{d\eta}$ in some way. To compute the rate of change of P with respect to η, η is varied horizontally. In the 2 cell case, this is equivalent of moving along the diagonal, that is, whenever η_1 varies, η_2 varies by the same amount and in order to compute the stability of the fixed point we must take in to account changes in η_1 and η_2 when the other parameter is fixed.

4.5.2.2 Case 2 : $\bar{\eta}_1 \neq \bar{\eta}_2$ and $\bar{\eta}_1 = \bar{\eta}_2$ (asynchronous solution) In this case, no simplification to the Jacobian matrix can be made, except for the fact that at the fixed point $\bar{\eta}_i = \bar{F}_i \;\; i = 1, 2$. Let $a = \frac{\partial \bar{F}_1}{\partial \eta_1}$, $b = \frac{\partial \bar{F}_1}{\partial \eta_2}$, $c = \frac{\partial \bar{F}_2}{\partial \eta_1}$ and $d = \frac{\partial \bar{F}_2}{\partial \eta_2}$. Then,

$$\overline{DP} = \begin{bmatrix} a + e^{-\bar{\alpha}_1(T_s)}(1-a) & b\left(1 - e^{-\bar{\alpha}_1(T_s)}\right) \\ c\left(1 - e^{-\bar{\alpha}_2(T_s)}\right) & d + e^{-\bar{\alpha}_2(T_s)}(1-d) \end{bmatrix} \tag{4.5.7}$$

The eigenvalues in absolute value are:

$$\begin{aligned} |\lambda_1| &= |\gamma + a\psi_1 + d\psi_2 + \beta(ad + cd)| \\ |\lambda_2| &= |\gamma + a\psi_1 + d\psi_2 + \beta(ad - cd)| \end{aligned}$$

where $\gamma = e^{-\bar{\alpha}_1(T_s)} e^{-\bar{\alpha}_2(T_s)}$, $\psi_1 = e^{-\bar{\alpha}_2(T_s)}\beta_1$, $\psi_2 = e^{-\bar{\alpha}_1(T_s)}\beta_2$ and $\beta = \beta_1\beta_2$ with $\beta_1 = \left(1 - e^{-\bar{\alpha}_1(T_s)}\right)$ and $\beta_2 = \left(1 - e^{-\bar{\alpha}_2(T_s)}\right)$ are all positive (and smaller than 1). The magnitude of λ_1 and λ_2 is going to depend on the magnitude of the derivatives of the F_i's with respect to η_1 and η_2.

4.5.3 Numerical computation of eigenvalues

In the previous section, some analytical expressions for λ_1 and λ_2 were given along with some predictions and connections with the self coupled single cell case. Now, making use of numerical differentiation, the eigenvalues corresponding to the synchronous solution will be numerically computed. The numerical differentiation is needed due to the fact that we cannot computed closed forms for the quantities a and b, defined above.

In equation (4.5.8), the terms $a = \frac{\partial \bar{F}_1}{\partial \eta_1}$ and $b = \frac{\partial \bar{F}_1}{\partial \eta_2}$ will be compute using centered differences according to the following equations:

$$\begin{aligned} a = \frac{\partial F_1}{\partial \eta_1} &= \frac{1}{2}\frac{F_1(\eta_1+\xi,\eta_2+\xi)+F_1(\eta_1+\xi,\eta_2-\xi)-2(F_1(\eta_1-\xi,\eta_2+\xi)+F_1(\eta_1-\xi,\eta_2-\xi))}{2\xi} \\ &= \frac{1}{2}\frac{dP}{d\eta}+\frac{F_1(\eta_1+\xi,\eta_2-\xi)-F_1(\eta_1-\xi,\eta_2+\xi)}{4\xi} \end{aligned} \tag{4.5.8}$$

Similarly,

$$b = \frac{\partial F_1}{\partial \eta_2} = \frac{1}{2}\frac{dP}{d\eta}+\frac{F_1(\eta_1-\xi,\eta_2+\xi)-F_1(\eta_1+\xi,\eta_2-\xi)}{4\xi} \tag{4.5.9}$$

where ξ is a small and positive constant. In our computations we use $\xi = 10^{-5}$. Also, in the above equations, $\frac{dP}{d\eta}$ corresponds to the eigenvalue of the self coupled single cell case. These expressions for a and b were computed taking into account that η_1 and η_2 vary simultaneously.

Using these approximations for a and b plugged into equations (4.5.5) and (4.5.6), the eigenvalues for $g_{ton} = 0.0325$ and $g_{syn} = 0.107143$ corresponding to the fixed point $(\bar{\eta}_1, \bar{\eta}_2) = (0.16622, 0.16622)$ are given by $\lambda_1 = 0.99994$ and $\lambda_2 = -11.54$. For these values of the parameters $a = -2.215e+03$ and $b = 2.216e+03$. The eigenvalues computed here match what we expect for the eigenvalues for the synchronous solution, since the synchronous solution can be only achieved by means of identical initial conditions.

Other attempts to compute the eigenvalues for $g_{ton} = 0.0325$ and $g_{syn} = 0.107143$ to corroborate what we found above were made. We used forward, backward and centered differences in various ways but, none of the results matched the values for the eigenvalues shown here. There are possibly several sources of error in the computation of the eigenvalues. One of these sources refers to the fact that numerical differentiation in some cases is highly unstable [3].

5.0 SIMULATIONS FOR TWO HETEROGENEOUS CELLS

In the previous chapters we analyzed the effects of coupling on networks of one self coupled single cell and two identical coupled cells using first return maps. In this chapter, we will study the effect of having g_{NaP} different for the two cells, say g_{NaP_1} and g_{NaP_2}. In the two cell case with the two cells with the same parameters, [5] determined all possible regimes and transitions on the (g_{syn}, g_{ton}) parameter space. Here for fixed g_{syn} and $\delta = 2.8 - g_{NaP_1} = g_{NaP_2} - 2.8$ with $\delta > 0$, we will see how the dynamics of the cell changes with (g_{ton}, δ) and we will compare our results to [5]. In this set up, δ measures the level of heterogeneity present in the network.

In the first two sections, we will revisit some of the concepts we saw earlier in this thesis and determine the effect of changing g_{NaP} for the self coupled single cell case. In the rest of the chapter, we will explain the effects of δ on the dynamics of the network.

5.1 BACKGROUND

Suppose we are in the self coupled single cell case and consider figure 35.

Let's recall a few things from chapter 2. We determine if a cell is *quiescent*, *bursting* or *spiking* depending on where the intersection of the h nullcline and the curve of fixed points S is and the position of the curve of periodics. Let's fix a value of g_{syn} for which the cell may undergo all different regimes (quiescence, bursting or spiking) and let χ be the intersection of the h nullcline and S with lowest value of v.

Case 1: *Quiescence* - In this case, h nullcline intersects S below lower knee (L_k). That is, for a sufficiently small g_{ton} when h increases on the lower branch of S it converges to a

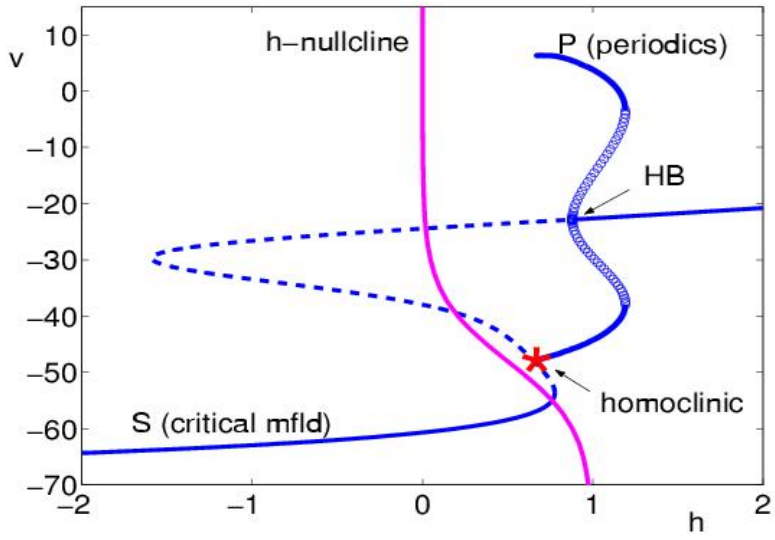

Figure 35: Bifurcation diagram for $g_{syn} = 0$ and $g_{ton} = 0.2$ [5]*(Copyright (c)2005 Society for Industrial and Applied Mathematics. Reprinted with permission. All rights reserved.)*

stable fixed point χ. In this case, we are in the *quiescent* region Q of the parameter space.

Case 2: *Bursting* - The h nullcline intersects S close to lower knee (L_k), but on the middle branch, with the curve of periodic still intersecting with the curve S. So, increasing g_{ton} makes the point χ migrate to the middle branch of S. χ loses stability there. From the neighborhood of the lower branch as h increases until it reaches L_k where it jumps to an *active* state. Now, the trajectory oscillates and the values of h drift to the left until the trajectory reaches an h value where it jumps down to the lower branch of S (hits the end of P). If this happens we say that our cell is *bursting*.

Case 3: *Spiking* - The h nullcline intersects S close to lower knee (L_k), still on the middle branch, but in this case the curve of periodics does not intersect S. That is, when g_{ton} is big enough the cell jumps to the active phase and stays there. The net drifting of the cell in h is very small. The cell is *tonically spiking*.

For all cases the position of the curve of fixed points S and P vary with g_{ton} (see [5]).

5.2 EFFECTS OF CHANGES IN G_{NAP} ON THE DYNAMICS

5.2.1 Self coupled single cell case

Recall from chapter 2 that changes in g_{ton} and g_{syn} affect the position of the curve of fixed points S and the curve of periodics P. Fixing all parameters and varying g_{syn} moves the curve P to lower values of h whereas the curve S remain practically unaltered; if g_{ton} is varied then both S and P move to lower values values of h [5]. These changes affect the equilibria of the system, since the intersection of the curve S and the h nullcline determine the steady states of the system, whereas changes in P affect the range of h values where the cell is active. In this section, all parameters of the system will be fixed except g_{NaP} in order to see how changes in this parameter change the dynamics of the cell. Figure 36 shows that both curves S and P move to lower values of h when g_{NaP} is increased. That is, the range of h values achieved on the trajectory moves to lower values of h.

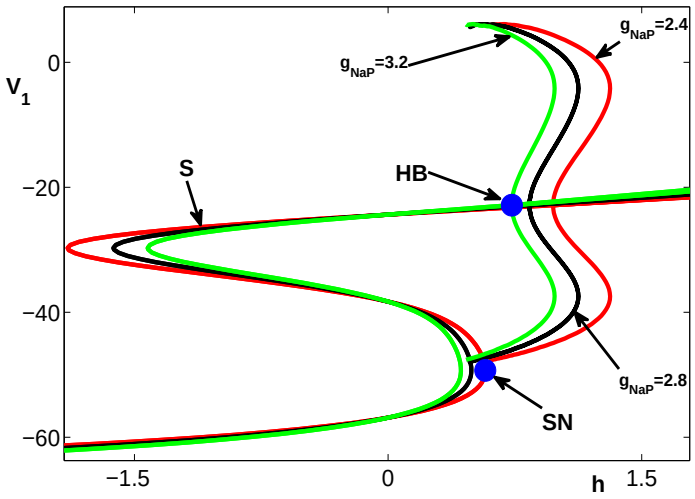

Figure 36: *top* - Bifurcation diagram corresponding to all parameter values fixed except g_{NaP}. The reference values for this plot were taken from [6]. Here $g_{syn} = 4$ and $g_{ton} = 0.4$. This figure also appears as figure 3 in chapter 2.

5.2.2 Coupled Cells

Define $\delta = 2.8 - g_{NaP_1} = g_{NaP_2} - 2.8$ be the level of heterogeneity of the network, where g_{NaP_1} and $g_{NaP_2} \geq 0$ refers to the values of g_{NaP} for cell 1 and cell 2, respectively and 2.8 is the reference value for g_{NaP} taken from [6]. The definition of δ implies that the maximal conductance of the persistent sodium will be varied symmetrically from the reference value 2.8 for the two cells at the same time.

Similar to what was done in chapter 3, all the analysis done here includes computing the averaged nullclines

$$N_i(h_1, h_2) = \frac{1}{T_s(h_1, h_2)} \int_0^{T_s(h_1,h_2)} g_i(v_i) d\xi \qquad i = 1, 2, \tag{5.2.1}$$

where $g_i(v_i) \equiv \epsilon \frac{(h_\infty(v_i) - h_i)}{\tau_h(v_i)}$ and $T_s(h_1, h_2)$ is the period of the fast subsystem periodic orbit being averaged for each fixed $(h_1,\ h_2)$ inside the oscillatory region O.

The goal here is, starting from the 4 regions found in [5], to determine how the dynamic range of bursting is affected by heterogeneity in g_{NaP}. Based on the configuration of the nullclines, on whether the averaged nullclines intersect inside O and on the stability of any resulting fixed points inside the O, we will determine changes in the dynamical behavior for different g_{NaP}.

In figure 37, the averaged h_1 and h_2 nullclines are shown for 3 different values of δ, namely, $\delta = 0, 0.001, 0.01$. Notice in this figure that an increase in δ implies that both averaged nullclines move to the right and down. The overall effect of increasing δ is to move the nullclines to larger values of h_1 and lower values of h_2. Some other tests were performed and similar results were obtained (not shown here).

Most of the analysis and studies done from now on include only the two cell case, unless some analogy with the one cell case is needed for comparison purposes.

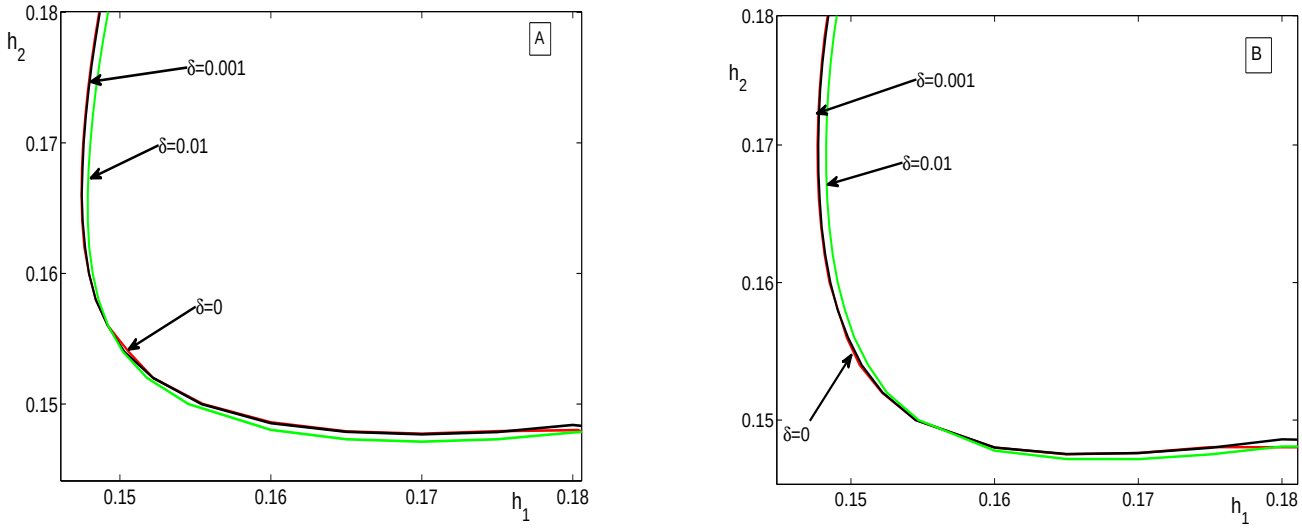

Figure 37: Changes in the averaged nullclines h_1 and h_2 when for three different levels of heterogeneity, namely, $\delta = 0(red)$, $\delta = 0.001(black)$ and $\delta = 0.01(green)$ and all other parameters fixed. (A) Changes in h_1 averaged nullcline; (B) changes in h_2 averaged nullcline.

5.3 CLASSIFYING DYNAMIC REGIMES

In order to possibly determine boundaries for the transition between different regimes similar to figure 7 in [5], we fixed g_{syn} and varied g_{ton} and δ. This procedure had the intent to check how changes in these 2 parameters would move the boundaries of the different regimes and if the appearance of a new regime was possible at all.

In the next three sections, we consider the effect of fixing g_{syn} and varying g_{ton} and δ.

5.3.1 Different regions of bursting and spiking for $g_{syn} = 3$

Before proceeding further, let us set up some notation and make some connections to the homogeneous case. In the homogeneous case, the averaged nullclines can intersect 1 or 3 times in O depending on the value of the parameters. Moreover, a pitchfork bifurcation of

periodics occurs as the parameter g_{ton} is increased, due to the symmetry of the fixed points on the (h_1, h_2) plane. In the heterogeneous case, it is possible to have 1, 2 or 3 intersections of the nullclines inside O, and each possibility will lead to a different behavior. The fixed points will be defined as follows: f_p^0 denotes a fixed point near the line $h_1 = h_2$; f_p^1 denotes a fixed point for $h_1 > h_2$ and f_p^2 denotes a fixed point for $h_2 > h_1$. When the three fixed points are present in O, they correspond, respectively, to p_0, q_B and q_A in the homogeneous case. Due to effects of heterogeneity the fixed point f_p^0 is not anymore at $h_1 = h_2$ as was p_0, but it should be close to the symmetry line for small δ.

In figure 38, a cartoon shows a generic result of symmetry breaking applied to a pitchfork bifurcation when different levels of heterogeneity are applied to this small network for $g_{syn} = 3$ and g_{ton} as a bifurcation parameter. Next, consider numerical results to assess the details of the transitions in the heterogeneous case.

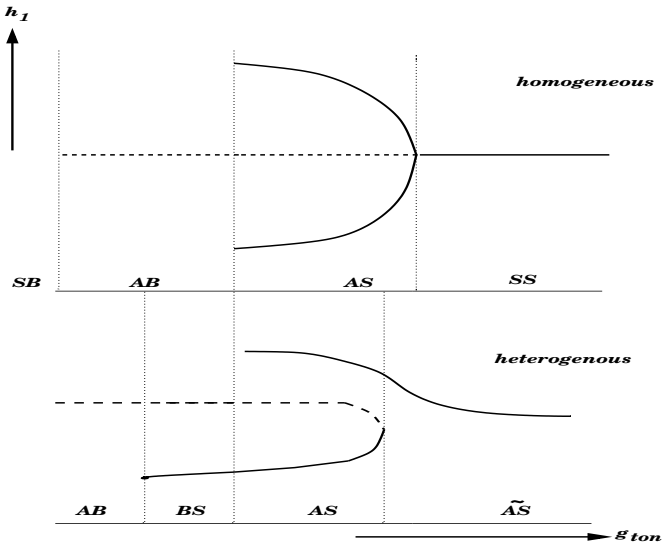

Figure 38: Cartoon representing the pitchfork bifurcation for the cells in the homogeneous case and another bifurcation diagram showing the break in symmetry when heterogeneity is introduced. In the picture, g_{ton} is the bifurcation parameter and $g_{syn} = 3$. Note that the choice of $\delta = 2.8 - g_{NaP_1} = g_{NaP_2} - 2.8$ influences the form of this bifurcation diagram. The regions **AB**, **BS**, **AS** and $\widetilde{\mathbf{AS}}$ are discussed in the text.

In figure 39, we show numerically how varying g_{ton} and δ with $g_{syn} = 3$ affected the dynamics of the 2 cells. In this picture, $\delta = 0$ represents the homogeneous case and $g_{ton} = 0.856$ and $g_{ton} = 0.898$ represent the values for the transition from **AB** to **AS** and **AS** to **SS**, respectively. For $\delta > 0$, the transitions between different regimes were determined as follows. Fixing $\delta = 0.01$, we systematically varied g_{ton} from lower to higher values and for various initial conditions. If 2 consecutive values of g_{ton} were giving completely different results on the (V_1, t), (V_2, t) and (h_1, h_2) planes, then the boundary for the transition from one regime to another was determined. We were not able to determine numerically the precise transition from **SB** and **AB** by direct numerical simulations in this way.

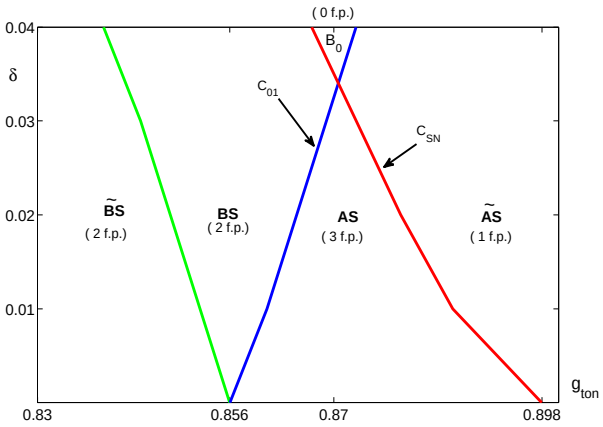

Figure 39: Different types of bursting and spiking for $g_{syn} = 3$. Values for $\delta = 0$ represent the values for which the transition for one regime to another takes place for a pair of homogeneous cells. Curve C_{SN} is a curve of saddle node points and C_{01} indicates that a fixed point enters the oscillatory region. In this figure $(i f.p.)$ indicates the presence of $1, 2 or 3$ fixed points on a given region.

In figure 40 we show a more complete description of the different regimes we expect to find for $g_{syn} = 3$. This cartoon is based on the numerical results presented on figure 39 and numerical simulations for various values of g_{ton} and δ using XPP/AUTO [14].

Now, let's describe what each of the regions presented on figures 39 and 40 represent for increasing g_{ton}. Since the notation is the same for both figures, I will describe all the elements in figure 40. In figure 40, **Q** represents the values of g_{ton} and δ, on the (g_{ton}, δ) plane

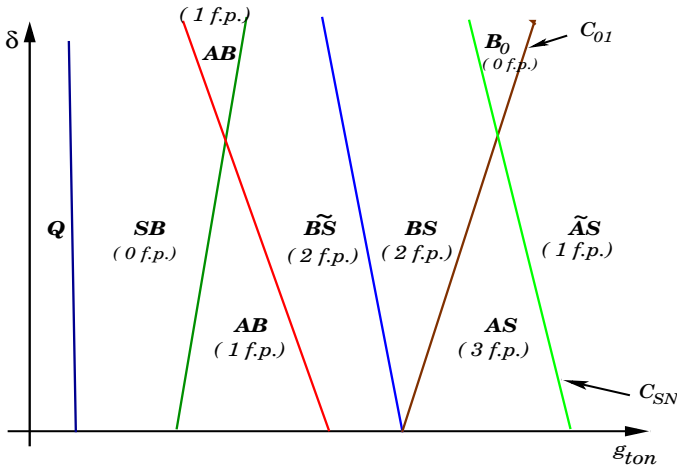

Figure 40: Cartoon showing all possible different types of bursting and spiking for $g_{syn} = 3$. This complements the numerical results obtained in figure 39.

so that the two cells are silent. We can see that for $\delta \neq 0$, the boundary of **Q** (dark blue curve) moves slightly to the left indicating that the transition from quiescence to bursting will occur for a lower value of g_{ton} as we increase δ, as observed numerically. The appearance of bursting activity for lower g_{ton} is likely to be due more excitation given to one of the cell with increasing δ, which can also be seen when we increase g_{NaP} in figure 36.

In region **SB** the cell is bursting. For all initial conditions trajectories of the full system approach reasonably close to the identity line and deviate from the identity line at the end of the active phase (figure not shown). In this region, we do not expect to find the average nullclines inside the oscillatory region. A typical bursting solution on the region **SB** is shown in figure 41.

In region **AB**, trajectories of the full system may approach one of two different solutions in the (h_1, h_2) plane. Initial conditions starting on or above the identity line go to a trajectory that stays above the identity line and initial conditions below the identity line yield trajectories of the full system that stay below the identity line for all time. In this region, based on perturbation of the homogeneous case, we expect the presence of the averaged nullclines inside the oscillatory region intersecting at a single (unstable) fixed point near the

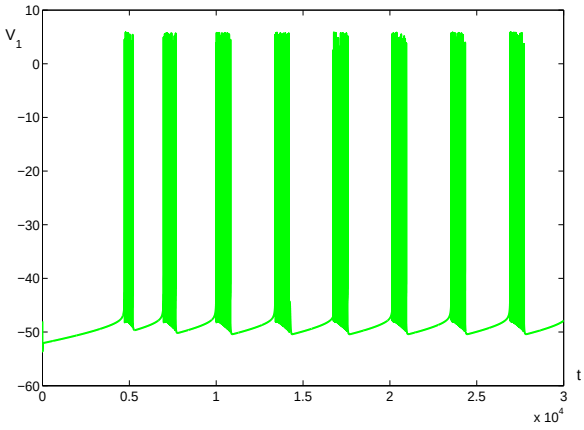

Figure 41: Typical bursting solution for $g_{syn} = 3$, $g_{ton} = 0.50$ and δ on region **SB**.

identity line. Transition from **SB** and **AB** is defined by the averaged nullclines entering the oscillatory region. The type of solution in this region is similar to the region **AB** described in [5].

In the following subsections is a description of the other regions.

5.3.1.1 Region $\tilde{\mathbf{BS}}$ As illustrated in figure 42(A), f_p^0 and f_p^1 are in O. For any IC, the system leaves the boundary of the computed oscillatory region through O. If IC are such that $h_2 < h_1$, then trajectories of the full system will exit the boundary Ω as shown in part (B) of figure 42. For IC with $h_1 < h_2$, trajectories of the full system cross Ω at some point above the line $h_1 = h_2$ (figure not shown). In figure 42(B), we show trajectories of the full system hang around f_p^1 inside O. For this initial conditions the cells are transitional from bursting to spiking. This type of solution we will call bursting with pause, and denote it by B_p to differentiate from the other types of bursting present in the system. According to our numerics, it seems that both f_p^0 and f_p^1 are unstable for these values of the parameters (figure 42(D)).

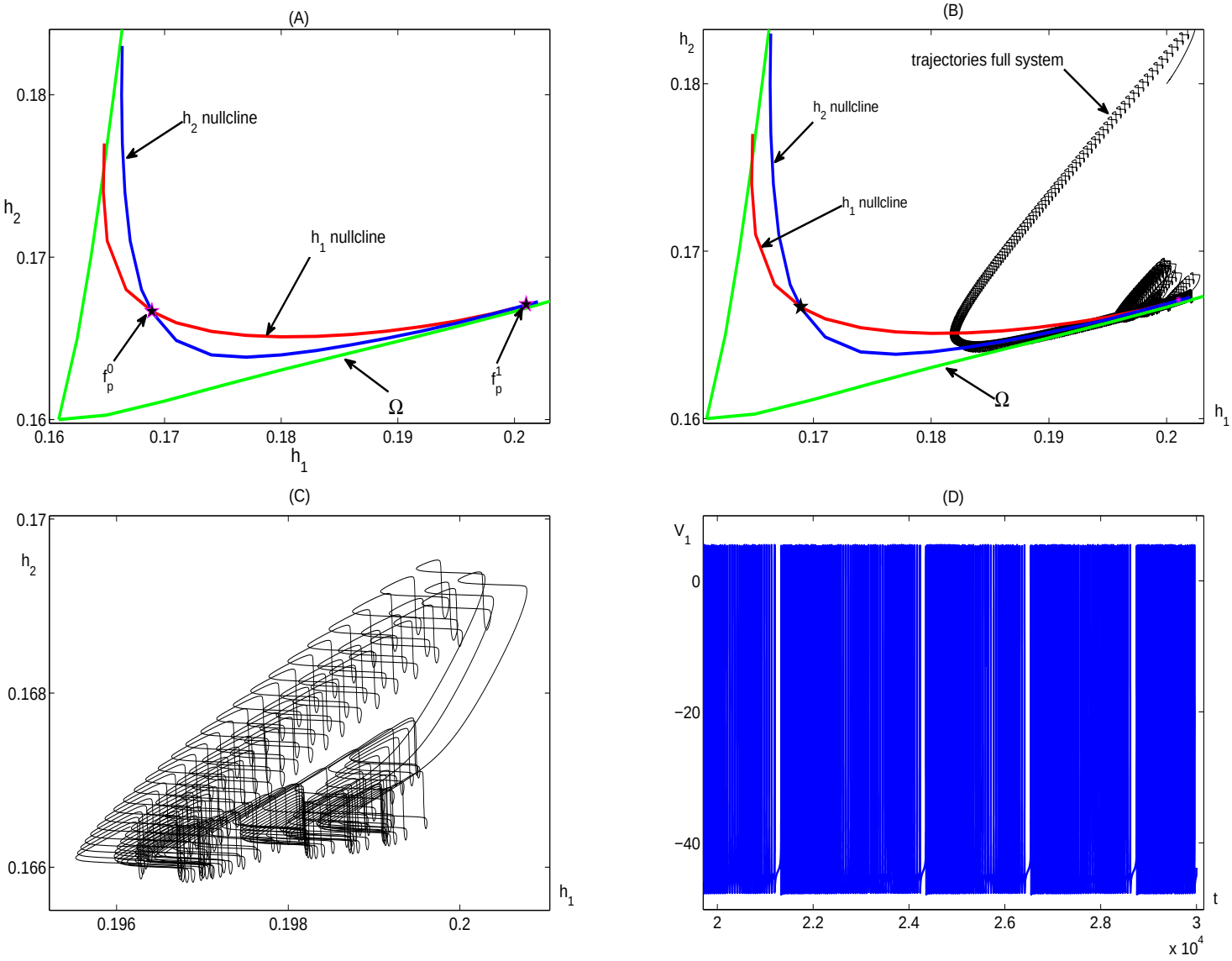

Figure 42: Example of (h_1, h_2) averaged dynamics from region $\tilde{\mathbf{BS}}$ with $g_{ton} = 0.84$, $g_{syn} = 3$ and $\delta = 0.01$. (A) Boundary of oscillatory region Ω with averaged nullclines h_1 and h_2 showing two fixed points in O. (B) Same as in (A), but with trajectories of the full system plotted together. (C) Trajectories of the full system after a sufficiently long transient has passed; (D) Plot of V_1 versus time showing a solution which we call a bursting with pause. This solution is transitional from bursting to spiking.

The transition from **AB** to $\tilde{\mathbf{BS}}$ happens with an unstable fixed point entering O for $h_1 > h_2$ through Ω. For δ big enough some numerical simulations of the full system show that a transition from **SB** to $\tilde{\mathbf{BS}}$ is also possible given that two unstable fixed points can enter the oscillatory region at the same time. This transition has to be further explored.

5.3.1.2 Region BS In this region, there are 2 fixed points inside O: f_p^0 and f_p^1. In this region, if one starts above $h_2 = h_1$, with $h_2 > h_1$, then trajectories of the full system (2.3.1)-(2.3.4) leave the oscillatory region above the identity line, fall through the silent phase and are reinjected to the active phase for some higher value of (h_1, h_2). Initial conditions below $h_2 = h_1$, with $h_2 < h_1$ take trajectories to f_p^1 and the system spikes. Now, f_p^0 is unstable and f_p^1 is stable, if we analyze the structure of the nullclines. In figure 43, a plot is shown for a representative of this region displaying the boundary of the oscillatory region Ω and the averaged nullclines along with the locations of the two fixed points. Also in the same figure, trajectories of the full system for different initial conditions. Note that, for initial conditions below the identity line, trajectories converge to f_p^1 and stay there forever and the system is spiking. For initial conditions above the identity line, trajectories leave O through Ω and after a transient has passed with see B_p type of bursting. Bursting solutions in **BS** are similar to the one shown in figure 45, except for some difference in burst duration which may decrease with increasing δ.

Note also in figure 43, the presence of a new region $\tilde{O}$. This region on the (h_1, h_2)parameter space correspond to pairs (h_1, h_2) for which the fast subsystem has B_p. A typical bursting solution for the fast subsystem is shown in figure 44.

5.3.1.3 Region $\mathbf{B}_0$ For $g_{syn} = 3$ and $\delta > 0.03$ there is another place where one can find bursting, for any initial condition. The region B_0 is between **BS** and $\tilde{\mathbf{AS}}$. Our conjecture is that the averaged nullclines do not intersect inside the oscillatory region. In this region, for any initial condition trajectories of the full system leave O through Ω above the identity line. In figure 45, plots of the voltages versus time show that indeed we have bursting with a period of recovery of about 100 ms. This is what we call bursting with pause, or B_p. We believe that the transition from **BS** and $\mathbf{B}_0$ occurs through a saddle node bifurcation.

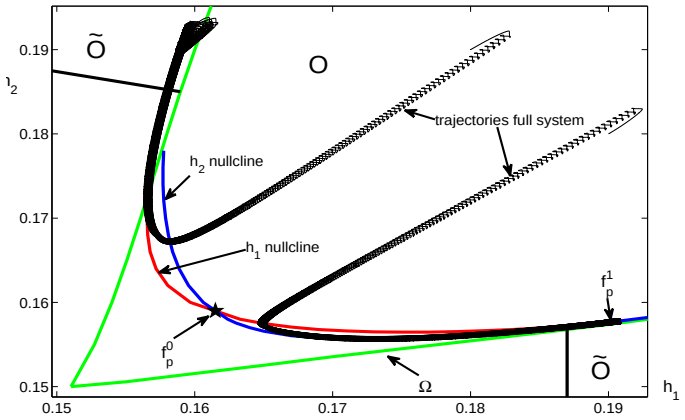

Figure 43: Solutions corresponding to region **BS** with $g_{ton} = 0.859$, $g_{syn} = 3$ and $\delta = 0.01$. Note the presence of the oscillatory region $\tilde{O}$ in which the fast subsystem is bursting with pause.

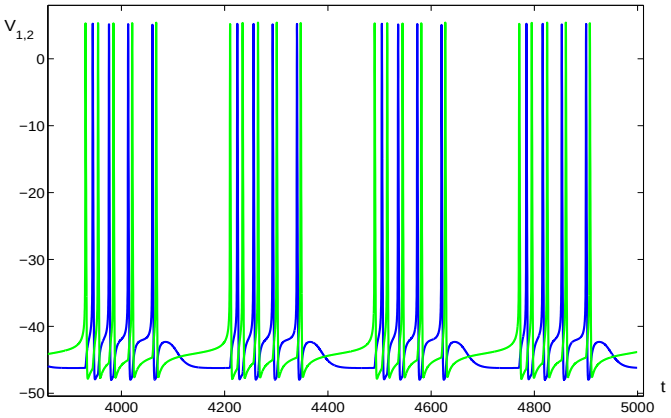

Figure 44: Typical bursting with pause solutions of the fast subsystem for $g_{syn} = 3$, $g_{ton} = 0.859$, $\delta = 0.01$, $h_1 = 0.149$ and $h_2 = 0.177$. Note that there are only four spikes per burst for both V_1 (blue) and V_2 (green).

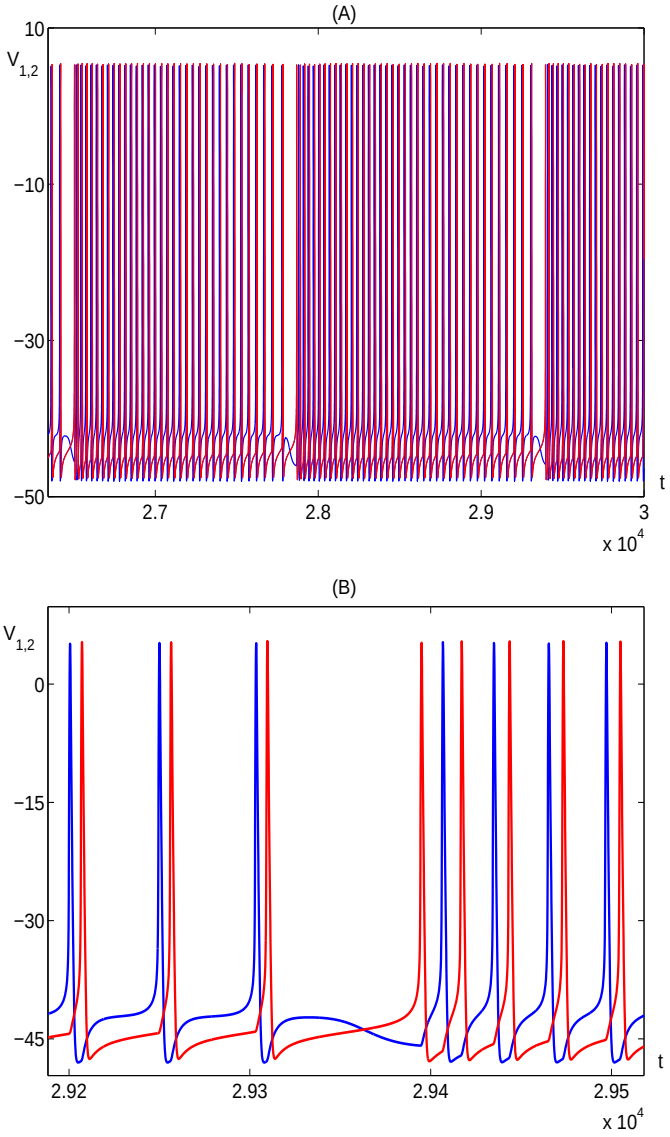

Figure 45: Plots showing solutions $g_{ton} = 0.87$ (top), $g_{syn} = 3$ and $\delta = 0.06$ on the region B_0. (A) V_1 and V_2 versus time showing the bursting solution. (B) Zoom of part (A) showing that there is a approximately 100ms of recovery period before the two cells start bursting again.

In this case, we go from two fixed points inside the oscillatory region in **BS** to no fixed points in region $\mathbf{B}_0$.

5.3.1.4 Regions AS and $\tilde{\mathbf{AS}}$ For region **S** the nullclines intersect each other in three distinct places. Two of the fixed points, f_p^0 and f_p^1 are inside O whereas f_p^2 is in $\tilde{O}$. No matter which initial condition is selected, the system exhibits tonic spiking. If you start with initial conditions above the $h_1 = h_2$ line, then the system goes to f_p^2. For initial conditions starting below the identity line the system goes to f_p^1. One representative of this region is shown in figure 46. Note that according to trajectories of the full system f_p^2 should be inside $\tilde{O}$ and not outside as it is shown in the picture. For initial conditions starting above the identity line we show trajectories of the full system with all transients until we get to the fixed point. In this region, f_p^1 and f_p^2 are stable where as f_p^0 is unstable.

For low values of δ, the transition from **BS** to **AS** will take place through C_{01} when a stable fixed point f_p^2 enters the region $\tilde{O}$. The transition from **AS** to $\mathbf{B}_0$ when at the cusp f_p^2 exits through $\tilde{O}$ and f_p^0 and f_p^1 are lost due to the saddle node (codimension 2 bifurcation).

Increasing g_{ton} further we see that f_p^0 and f_p^1 get closer and closer together and eventually h_2 and h_1 nullclines do not intersect anymore below the $h_2 = h_1$ line (inside O) and, thus, the only intersection left is f_p^2. For $\delta = 0.02$ and $g_{ton} = 0.88$ according to figure 47, f_p^2 is in $\tilde{O}$ and it is stable. Inside O the 2 nullclines are very close together for some values of h_1 and h_2. For all initial conditions, trajectories of the full system (2.3.1)-(2.3.4) converge to the fixed point. For some initial conditions the trajectories of the full system may hang around the two averaged nullclines for a while before it moves toward the fixed point. Notice that our fixed point is not exactly a match with the trajectories, but we are very close to it. This difference is due to error in the numerical computation of the averaged nullclines. This transition from 3 fixed points to only 1 fixed point, i.e., from **AS** to $\tilde{\mathbf{AS}}$, can only occur if the system passes through a saddle node point. Therefore, the curve C_{SN}, in figure 40, represents a curve of saddle node points for increasing δ.

Finally, the transition from $\mathbf{B}_0$ to $\tilde{\mathbf{AS}}$ occurs due to a fixed point entering $\tilde{O}$ through C_{01}. Note that the fixed point f_p^2 in $\tilde{\mathbf{AS}}$ can, in theory, move to region O. In table 5, we summarize all different regimes believed to be take place for $g_{syn} = 3$.

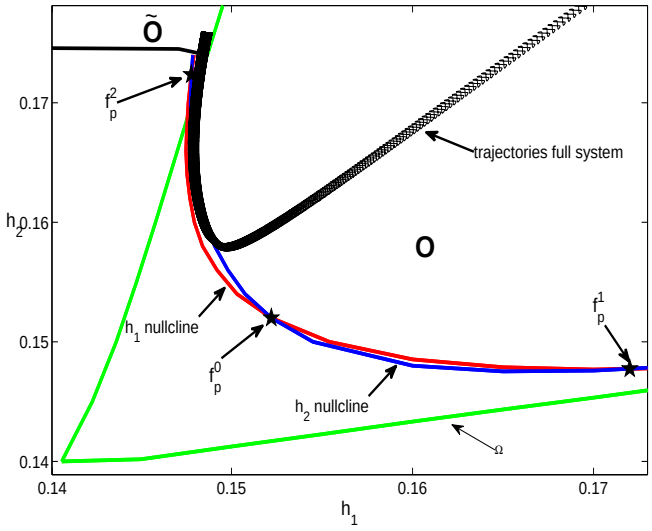

Figure 46: Representative of region **AS** for $g_{ton} = 0.88$, $g_{syn} = 3$ and $\delta = 0.01$, along with the trajectories of the full system for initial conditions with $h_2 > h_1$. These trajectories show that the fixed point f_p^2 was computed with some error and it should be inside $\tilde{O}$.

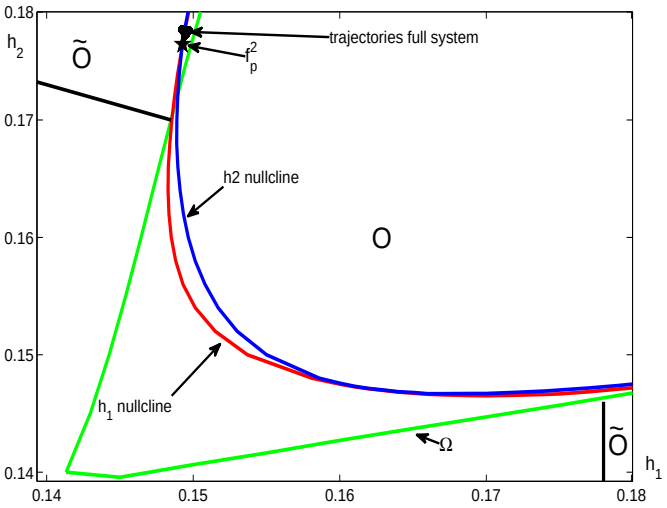

Figure 47: Representative of region $\tilde{\mathbf{AS}}$ for $g_{ton} = 0.88$, $g_{syn} = 3$ and $\delta = 0.02$

regime	picture	fixed point and stability	dyn. full system
SB	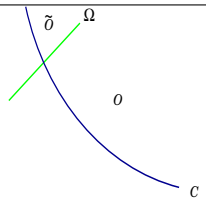	No fixed points in **O** or $\tilde{\mathbf{O}}$	bursting
AB	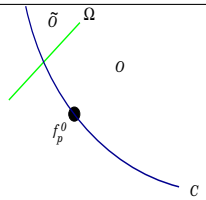	f_p^0 - unstable	bursting
B$\tilde{\text{S}}$	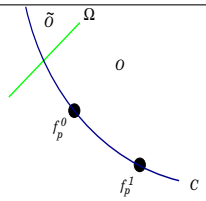	$\begin{cases} f_p^0 - unstable \\ f_p^1 - unstable \end{cases}$	$\begin{cases} bursting\ if\ h_2 > h_1 \\ bursting\ with\ pause\ if\ h_2 < h_1 \end{cases}$
BS	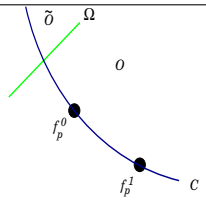	$\begin{cases} f_p^0 - unstable \\ f_p^1 - stable \end{cases}$	$\begin{cases} bursting\ with\ pause\ if\ h_2 > h_1 \\ spiking\ if\ h_2 < h_1 \end{cases}$
AS	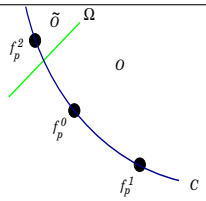	$\begin{cases} f_p^0 - unstable\ (in\ \mathbf{O}) \\ f_p^1 - stable\ (in\ \mathbf{O}) \\ f_p^2 - stable (in \tilde{\mathbf{O}}) \end{cases}$	spiking
A$\tilde{\text{S}}$	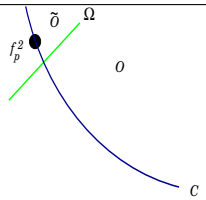	f_p^1 - stable	spiking
$\mathbf{B}_0$	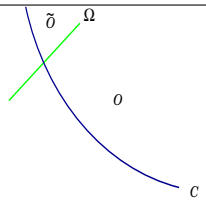	*no fixed points*	bursting with pause

Table 5: Summary of the different regions described in figure 40 and described in the text.

5.3.2 Different regions of bursting and spiking for $g_{syn} = 6$

For $g_{syn} = 6$, three regions were characterized: $\mathbf{B}_1$, $\mathbf{B}_2$ and $\mathbf{S}$. These regions are equivalent to regions **SB**, **AB** and **SS** found in [5]and are shown in figure 48. One important difference of the region found in the heterogeneous case and the homogeneous case was the fact that the fixed point of the averaged nullclines did not take place on the identity line as it was happening before. This is expected due to the fact that the averaged nullclines move when δ is increased.

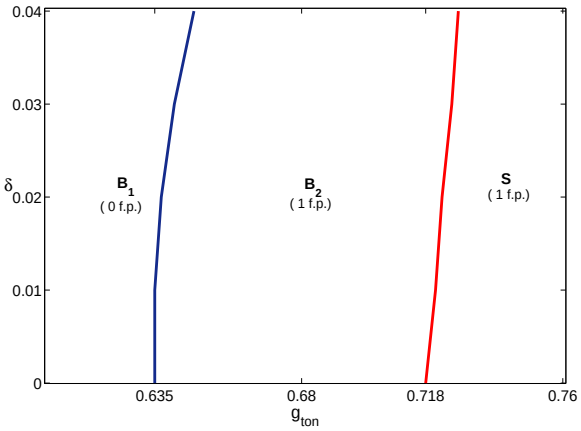

Figure 48: Different types of bursting and spiking for fixed values of $g_{syn} = 6$. Values for $\delta = 0$ represent the values for which the transition for one regime to another takes place for a pair of homogeneous cells. In this figure $(if.p.)$ indicates that there could be $i = 0, 1$ fixed point inside the oscillatory region.

5.3.2.1 Regions $\mathbf{B}_1$ and $\mathbf{B}_2$ According to our computations these two regions are similar to regions **SB** and **AB** found in [5]. That is, in $\mathbf{B}_1$ averaged nullclines do not enter O. For any initial condition, trajectories of the full system exit O through Ω, fall into the lower branch of the curve S and the values of h_1 and h_2 increase until they reach the SN where trajectories enter O again (figures not shown). For $\mathbf{B}_2$, the averaged nullclines enter $\mathbf{B}_2$ where they intersect at f_p^0, an unstable fixed point. Trajectories of the full system starting in O exit the oscillatory region through Ω. Figure 49(top), shows the boundary of the

oscillatory region together with the trajectories of the full system for region $\mathbf{B}_2$ to illustrate what happens in general with trajectories in this region.

Some numerical difficulties arose here in order to determine precisely the location of each nullcline, although further computation showed us that these nullclines are reasonably positioned (not shown here). By numerical difficulties it is meant that when determining the averaged nullclines convergence to zero for the averaged nullclines was not precisely obtained. What was observed instead was a sudden jump from positive to negative (or vice-versa) of both nullclines at the same time making it hard to determine when $\dot{h}_1 = 0$ and $\dot{h}_2 = 0$.

5.3.2.2 Region S For $g_{syn} = 6$, opposite to what happened with $g_{syn} = 3$ we have only one region of spiking. In this region as it happened for the other value of g_{syn} we have only one fixed point to which all IC converge to (see figure 49)(bottom).

5.3.3 Different regions of bursting and spiking for $g_{syn} = 9$

Boundaries for the transition between different regimes were determined also for $g_{syn} = 9$ and no significant difference was found from the transitions for the homogeneous case, at least for the level of heterogeneity applied to the system. The reason for such invariance can be the fact that the system coupling is quite strong when compared to the previous cases, not allowing changes in dynamical regimes. These results are not shown here. The transition from quiescence to bursting was barely affected by heterogeneity, again considering the level of heterogeneity that was applied to the system. Higher heterogeneity levels may or may not make a significant change in this boundary.

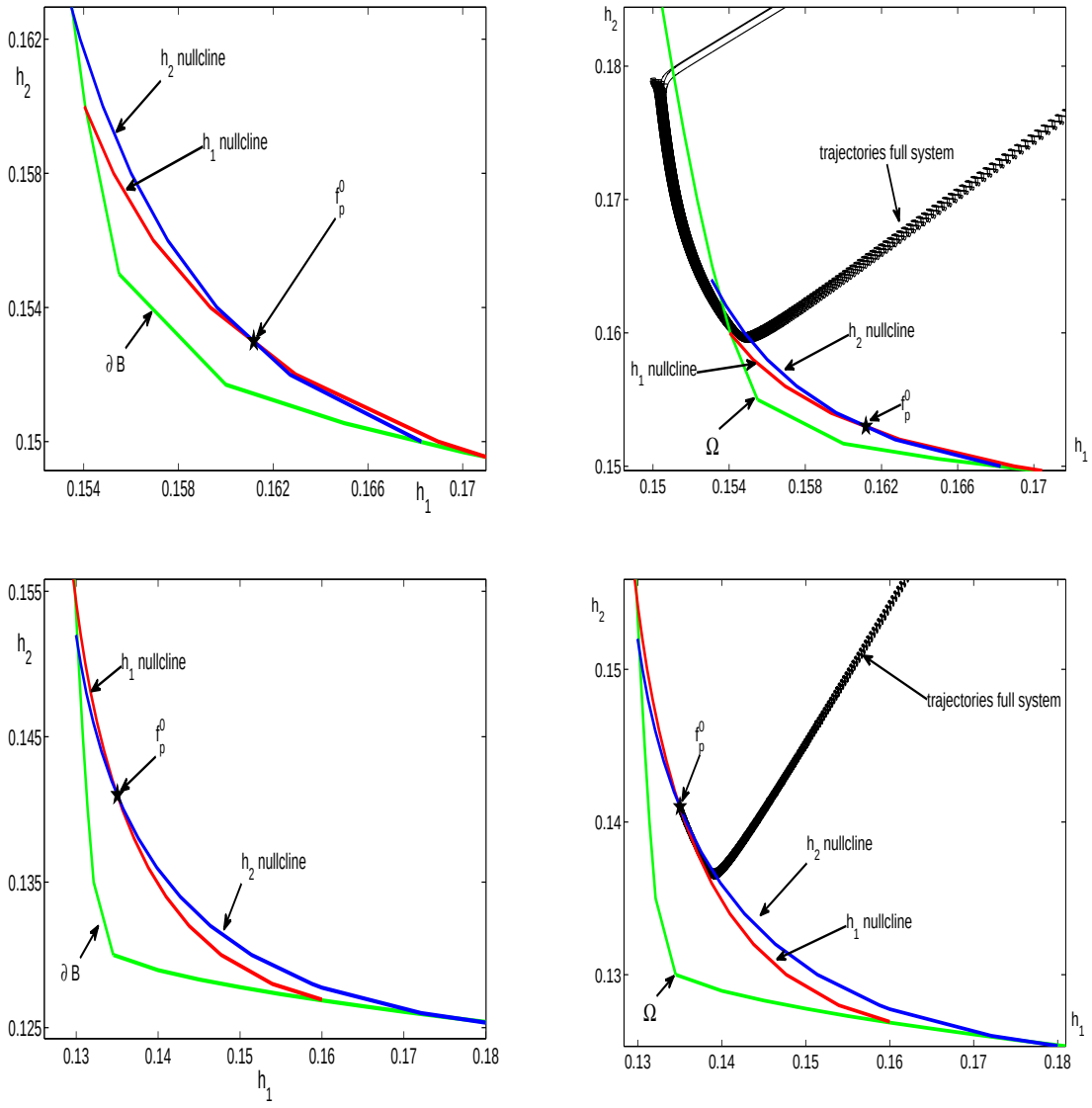

Figure 49: Representative of region $\mathbf{B}_2$ with $g_{ton} = 0.70$ (top); region $\mathbf{S}_2$ with $g_{ton} = 0.74$ (bottom). For these cases, $g_{syn} = 6$ and $\delta = 0.02$

5.4 HOMOGENEOUS × HETEROGENEOUS

Many differences arose when comparing the homogeneous ($g_{NaP_1} = g_{NaP_2}$) and heterogeneous ($g_{NaP_1} \neq g_{NaP_2}$). First, for the heterogeneous case we could not make the same analysis for general values of g_{ton} and g_{syn} as Best *et al* [5] did in the homogeneous case. We had to compute boundaries of spiking and bursting for particular values of g_{syn} and different values of δ when varying g_{ton}.

For the homogeneous case, we have that for any given value of g_{syn} the boundary between quiescence and bursting had a value of g_{ton} that was almost the same for all values of g_{syn}. More specifically, $g_{ton} \simeq 0.26$ (see [5]). For $\delta = 0.1$, the transition between quiescence and bursting takes place for some g_{ton} between 0.23 and 0.24. Therefore, the two cells in the heterogeneous case tend to become active for lower external inputs.

In theory, with increasing of heterogeneity we have chance to have bursting for a bigger interval of g_{ton}. That is, bursting should start with smaller external inputs applied to the system. This change in the boundary Q-**SB** was observed for $g_{syn} = 3$ and $g_{syn} = 6$.

For $g_{syn} = 3$, if we consider all the regions where the cell presents some type of bursting, the range of g_{ton} for which we have bursting is bigger than for the homogeneous case, although we have some dependency on initial conditions and one type of bursting is transitional. This shows that heterogeneity increases our chances of having a larger range of parameters where bursting is possible [7].

For $g_{syn} = 6$ we see an increasing of the bursting region independent of IC by 0.01 when we increased δ by 0.04, that is, for $\delta = 0.0$ the boundary of $\mathbf{B}_2 - \mathbf{S}$ occurs for $g_{ton} \simeq 0.718$ and for $\delta = 0.04$ this boundary was shifted to $g_{ton} \simeq 0.728$. Once again, we have improvement of bursting, but up to now we couldn't find a "island" of bursting after we started having the appearance of spiking. This is probably due to the fact that the synaptic input is too big to allow this kind of behavior.

Finally, for $g_{syn} = 9$ we don't have any improvement in the transition of bursting-spiking for δ varying from 0.0 to 0.04(results not shown here). In the homogeneous case this value of g_{syn} gives us just symmetric bursting and tonic spiking. This is similar to what was found in [5] for this level of synaptic input.

6.0 CONCLUSIONS

In this thesis, we used one and two dimensional maps and direct numerical simulations to determine how heterogeneity and coupling could be affecting the behavior of a small network of preBötC cells.

A one dimensional map was derived from an approach given by [37], using the slow dynamics and averaging over the fast subsystem. Analysis was used to establish certain features of the form of map, which in turn allowed us to determine the possible transition mechanisms for different levels of synaptic input and external drive. With the analytical results and numerical analysis, conditions for the onset of bursting for the self coupled single cell case were determined. The analytical conditions were numerically tested and proved to be accurate in determining such transition from spiking to bursting for small values of g_{syn}. For larger values of the synaptic input the transitions between bursting and spiking was numerically determined. For all these transitions information about the presence of homoclinic point was also used. The results obtained for the one dimensional map were an improvement on the transition from bursting to spiking and spiking to bursting determined in [5] for the singular limit case $\epsilon = 0$.

Using some of the ideas as for the one dimensional map, we derived for the network of two coupled identical cells a two dimensional iterated map. In the derivation of the map we used the two slow variables of the system and we averaged over the fast subsystem. The idea of the iterated map was introduced via a numerical example and together with the averaged nullclines a form of the iterated map was determined via a mix of analysis and numerics, and the form of the map was used to derive possible dynamical regimes for the two cell network. The iterated map obtained is a composition of one dimensional maps and its shape is determined depending whether or not the trajectories of the full system

intersect the averaged nullclines. For one set of parameters considered, $g_{syn} = 0.107143$ and $g_{ton} = 0.3107$, corresponding to the **AS** region, we could not determine the map as we predicted, in part due to the numerical error and for the fact that, as shown in [5], the two averaged nulllclines are really close to each other, making computations difficult to perform. Qualitative the form of the map was as predicted.

For the case when the network is spiking in synchrony, a linear analysis was performed and analytical expressions for the eigenvalues of the linearized system were found. However, once again numerical error prevented us from computing numerically the exact values for the eigenvalues. Therefore, we were not able to conclude anything about the stability of the fixed point of the iterated map. According to our analytical expressions we should have found that the fixed point corresponding to the synchronous state had to be unstable.

However, overall this analysis gave us a good understanding of the dynamics of this small network of preBötC cells in terms of the map. Although, we made a significant progress in understanding the dynamics of the network, some work still remains to be done. In this thesis, we only computed the map in the homogeneous case. Including heterogeneity, we expect to find interesting solutions which include what has been observed before for the homogeneous case plus possibly some other novel behaviors.

Using direct numerical simulations, when heterogeneity was added to our network for fixed values of the synaptic input, we determined in the (g_{ton}, δ) parameter space boundaries for transition between different regimes, for $g_{syn} = 3, 6, 9$. For these fixed values of g_{syn} we observed some very interesting behaviors. For $g_{syn} = 3$, a region where the 2 cells could either burst or spike, depending on the initial conditions was observed for a significant region in parameter space for low heterogeneity levels. Another region where cells were bursting was found after enough heterogeneity was applied to the network. The region where bursting and spiking coexist, may give us some insight in how applying certain levels of heterogeneity can improve significantly the range of bursting.

For the other 2 values of the synaptic input studied, the regions of activity did not change very much with heterogeneity. This could imply that an optimal level of heterogeneity, synaptic input and tonic current can maximize the region where bursting can be seen numerically for a large range of parameters. This certainly has to be studied in more detail.

For the heterogeneous system no analytical studies were performed. We strongly believe that an analysis of this heterogeneous system would give us some more insight on how heterogeneity is affecting the range of bursting for a network of cells. Another path that this study can take is the study of bigger networks of preBötC neurons. Although ambitious, this would provide us with even more understanding of the network mechanisms. Analytical work on synchrony and clustering in neuronal networks has already been done and related ideas could be implemented for this particular neural network, which has recently been discovered to have certain structured synaptic architecture [21].

We hope that this mathematical approach on studying a small network of preBöTC neurons combined with some experimental results is able to predict and help in finding mechanisms to prevent some aspect of diseases which are associated with the damaging of the neuronal cells responsible for respiratory rhythmogenesis, such as the preBötC cells.

BIBLIOGRAPHY

[1] M. E. Alexianu, B.-K. Ho, A. H. Mohamed, V. La Bella, R. G. Smith, and S. H. Appel. The role of calcium-binding proteins in selective motoneuron vulnerability in amyotrophy lateral sclerosis. *Ann. Neuro.*, 36:846–858, 1994.

[2] R. Altendorfer, D. Koditschek, and P. Holmes. Stability analyisis of legged locomotion by symmetry-factored return maps. *Int. J. Robotics Research*, 23:979–999, 2003.

[3] K.E. Atkinson. *An introduction to Numerical Analysis*. John Wiley & Sons, Inc., second edition, 1988.

[4] E.E. Benarroch, A.M. Schmeichel, P.A. Low, and J.E. Parisi. Depletion of ventromedullary nk-1 receptor-immunoreactive neurons in multiple system atrophy. *Brain*, 126:2183–2190, 2003.

[5] J. Best, A. Borisyuk, J. Rubin, D. Terman, and M. Welschselberger. The dynamic range of bursting in a model respiratory pacemaker network. *SIAM J. Appl. Dyn. Syst.*, 4:1107–1139, 2005.

[6] R. Butera, J. Rinzel, and J. Smith. Models of respiratory rhythm generation in the pre-bötzinger complex. i. bursting pacemaker neurons. *J. Neurophysiol.*, 82:382–397, 1999.

[7] R. Butera, J. Rinzel, and J. Smith. Models of respiratory rhythm generation in the pre-bötzinger complex. ii. population of coupled pacemaker. *J. Neurophysiol.*, 82:398–415, 1999.

[8] P. Channell Jr., G. Cymbalyuk, and A. Shilnikov. Applications of the poincaré mapping technique to analysis of neuronal dynamics. *Neurocomputing*, 70:2107–2111, 2007.

[9] T.R. Chay and J. Rinzel. Bursting, beating, and chaos in an excitable membrane model. *J. Biophys. Soc.*, 47:357–366, 1985.

[10] P. Darbon, C. Yvon, J.-C. Legrand, and J. Streit. i_{NaP} underlies intrinsic spiking and rhythm generation in networks of cultured rat spinal cord neurons. *Eur. J. Neurosci.*, 20:976988, 2004.

[11] C. A. Del Negro, C. Morgado-Valle, J. A. Hayes, D. D. Mackay, R. W. Pace, E. A. Crowder, and J. L. Feldman. Sodium and calcium current-mediated pacemaker neurons and respiratory rhythm generation. *J. Neurosci.*, 25:446–453, 2005.

[12] C.A. Del Negro, S.M. Johnson, R.J. Butera, and J.C. Smith. Models of respiratory rhythm generation in the pre-bötzinger complex. iii. experimental tests of model predictions. *J. Neurophysiol.*, 86:59–74, 2001.

[13] W.L. Ditto, S.N. Rauseo, and M.L. Spano. Experimental control of chaos. *Phys. Rev. Letters*, 65:3211–3214, 1990.

[14] B. Ermentrout. *Simulating, Analyzing, and Animating Dynamical Systems: A Guide to XPPAUT for Researchers and Students.* Software Environ. Tools 14, SIAM, Philadelphia, 2002.

[15] G.B. Ermentrout and N. Kopell. Fine structure of neural spiking and synchronization in the presence of conduction delays. *Proc. Natl. Acad. Sci. USA*, 95(3):1259–64, 1998.

[16] J.L. Feldman, C.A. Connelly, H.H. Ellenberger, and J.C. Smith. The cardiorespiratory system within the brainstem. *Eur. J. Neurosic.*, 3 (Supplem.):171, 1990.

[17] J.L. Feldman and C.A. Del Negro. Looking for inspiration: new perspectives on respiratory rhythm. *Nature*, 7:232–242, 2006.

[18] A.A. Gomes, E. Manica, and M.C. Varriale. Applications of chaos control techniques to a three-species food chain,. *Chaos, Solitons and Fractals*, 35:432–441, 2008.

[19] P.A. Gray, W.A. Janczewski, N. Mellen, D.R. McCrimmon, and J.L. Feldman. Normal breathing requires prebötzinger complex neurokinin-1 receptor-expressing neurons. *Nature Neurosci.*, 4:927–930, 2001.

[20] S. Grillner. Biological pattern generation: Review the cellular and computational logic of networks in motion. *Neuron*, 52:751–766, 2006.

[21] N. Hartelt, E. Skorova, T. Manzke, M. Suhr, L. Mironova, S. Kügler, and S.L. Mironova. Imaging of respiratory network topology in living brainstem slices. *Mol. Cell. Neurosci.*, 37:425431, 2008.

[22] A. L. Hodgkin and A. F. Huxley. A quantitative description of membrane current and its application to conduction and excitation in nerve. *J.Physiol.(London)*, 4:500–544, 1952.

[23] X. Huang, W. C. Troy, Q. Yang, H. Ma, C. R. Laing, S. J. Schiff, and J.-Y. Wu. Spiral waves in disinhibited mammalian neocortex. *J. Neurosci.*, 24:9897–9902, 2004.

[24] W.A. Janczewski and J.L. Feldman. Distinct rhythm generators for the inspiration and expiration in the juvenile rat. *J. Physiol.(Lond.)*, 570:407–420, 2006.

[25] W.A. Janczewski, H. Onimaru, I. Homma, and J.L Feldman. Opioid-resistant respiratory pathway from the pre-inspiratory neurones to abdominal muscles. *J. Physiol.(Lond.)*, 545:1017–1026, 2002.

[26] D.E Morrison J.C. Smith, H.H. Ellenberger, M.R. Otto, and J.L. Feldman. Brainstem projections to the major respiratory neuron populations in the medulla of the cat. *J. Comp. Neurol.*, 281:69–96, 1989.

[27] J.Guckenheimer and P. Holmes. *Nonlinear Oscillations, dynamical systems, and bifurcations of vector fields*. Springer-Verlag, New York, 1983.

[28] S. M. Johnson, N. Koshiya, and J. C. Smith. Isolation of the kernel for respiratory rhythm generation in a novel preparation: The pre-bötzinger complex island. *J. Neurophysiol.*, 85:1772–1776, 2001.

[29] S.M. Johnson, J.C. Smith, G.D Funk, and J.L Feldman. Pacemaker behavior of respiratory neurons in medullary slices from neonatal rats. *J. Neurophysiol.*, 73:2598–2608, 1994.

[30] J. Kevorkian and J.D. Cole. *Perturbation methods in applied mathematics*. Springer-Verlag, New York, 1981.

[31] H. Koizumi and J. C. Smith. Persistent na^+ and k^+-dominated leak currents contribute to respiratory rhythm generation in the pre-bötzinger complex *in vitro*. *J. Neurosci.*, 28:1773–1785, 2008.

[32] Y.A. Kuznetsov. *Elements of applied bifurcation theory*, volume 112 of *Applied Math. Sciences*. Springer-Verlag, Berlin, 1995.

[33] T. LoFaro and N. Kopell. Timing regulation in a network reduced from voltage-gated equations to a one-dimensional map. *J. Math. Biol.*, 38:479–533, 1999.

[34] J.E. Marsden and M.J. Hoffman. *Elementary classical analysis*. W.H Freeman and Company, New York, second edition, 2001.

[35] The MathWorks, Inc. *MATLAB The Language of Technical Computing*, version 7.6.0.324(r2008a) edition, Feb. 2008.

[36] L.C. McKay, W.A. Janczewski, and J.L. Feldman. Sleep-disordered breathing following targeted ablation of prebötzinger complex. *Nature Neurosci.*, 8:1142–1144, 2005.

[37] G.S. Medvedev. Reduction of a model of an excitable cell to a one-dimensional map. *Physica D*, 202:37–59, 2005.

[38] G.S. Medvedev. Transition to bursting via deterministic chaos. *Phys. Rev. Lett.*, 97:048102, 2006.

[39] G.S. Medvedev and Y. Yoo. Chaos at the border of criticality. *CHAOS*, 18:033105, 2008.

[40] N.M. Mellen, W.A. Janczewski, C.M. Bocchiaro, and J.L Feldman. Opioid-induced quantal slowing reveals dual networks for respiratory rhythm generation. *Neuron*, 37:821–826, 2003.

[41] A. Milik, P. Szmolyan, H. Löffelmann, and E. Gröller. Geometry of mixed-mode oscillations in the 3-d autocatalator. *Int. J. Bif. Chaos*, 8:505 – 519, 1998.

[42] R.E. O'Malley. *Singular perturbation methods in ordinary differential equations*. Springer-Verlag, New York, 1991.

[43] L. Perko. *Differential equations and dynamical systems*. Springer-Verlag, New York, third edition edition, 2001.

[44] L. K. Purvis, J. C. Smith, H. Koizumi, and R. J. Butera. Intrinsic bursters increase the robustness of rhythm generation in an excitatory network. *J. Neurophysiol.*, 97:15151526, 2007.

[45] J.C. Rekling and J.L Feldman. Prebötzinger complex and pacemaker neurons: hypothesized site and kernel for respiratory rhythm generation. *Annu. Rev. Physiol.*, 60:385–405, 1998.

[46] J. Rinzel. Bursting oscillations in an excitable membrane model. In B.D. Sleeman and R.J. Jarvis, editors, *Ordinary and Partial Differential Equations*, pages 304–316. Springer-Verlag, Berlin, 1985.

[47] J. Rinzel and W.C. Troy. Bursting phenomena in a simplified oregonator flow system d activity an model. *J. Chem. Phys.*, 76:1775–1789, 1982.

[48] J. Rinzel and W.C. Troy. A one-variable map analysis of bursting in the belousov-zhabotinskii reaction. *Lecture Notes in Biomathematics*, 51:1–23, 1982.

[49] J. Rubin and D. Terman. Synchronized activity and loss of synchrony among heterogeneous conditional oscillators. *SIAM J. Appl. Dyn. Syst.*, 1:146–174, 2002.

[50] N.F. Rulkov. Modeling of spiking-bursting neural behavior using two-dimensional map. *Physical Review E*, 65, 2002.

[51] N.F. Rulkov. Oscillations in large-scale cortical networks: map-based model. *J. Comput. Neurosci.*, 17:203–223, 2004.

[52] I.A. Rybak, J.F.R. Paton, and J.S. Schwaber. Modeling neural mechanisms for genesis of respiratory rhythm and pattern. i. models of respiratory neurons. *J. Neurophysiol.*, 77:1994–2006, 1997.

[53] I.A. Rybak, J.F.R. Paton, and J.S. Schwaber. Modeling neural mechanisms for genesis of respiratory rhythm and pattern. ii. network models of the central respiratory pattern generator. *J. Neurophysiol.*, 77:2007–2026, 1997.

[54] I.A. Rybak, N.A. Shevtsova, K. Ptak, and D.R. McCrimmon. Intrinsic bursting activity in the prebötzinger complex: Role of persistent sodium and potassium currents. *Biol. Cybern.*, 90:59–74, 2004.

[55] I.A. Rybak, N.A. Shevtsova, W.M. St-John, J.F.R. Paton, and O. Pierrefiche. Endogenous rhythm generation in the prebötzinger complex and ionic currents: modeling and *in vitro* studies. *Eur. J. Neurosci.*, 18:239–257, 2003.

[56] J.C. Smith, H.H. Ellenberger, K. Ballayi, D.W. Richter, and J.L. Feldman. Pre-bötzinger complex: A brainstem region that may generate respiratory rhythm in mammals. *Science*, 254:726–729, 1991.

[57] X. Wang. Period-doublings to chaos in a simple neural network. *IEEE*, pages 333–339, 1991.

[58] D. E. Weese-Mayer, L. Zhou, E. M. Berry-Kravis, B. S. Maher, J. M. Silvestri, and M. L. Marazita. Association of the serotonin transporter gene with sudden infant death syndrome: a haplotype analysis. *Am. J. Med. Genet. A*, 122:238–245, 2003.

[59] S. Wiggins. *Global bifurcations and chaos.* Springer-Verlag, New York, 1988.